INSTITUTO NACIONAL DE MATEMÁTICA PURA E APLICADA

Content-Based Projections for Panoramic Images and Videos

Leonardo Koller Sacht

Advisor: Paulo Cezar Carvalho

Co-advisor: Luiz Velho

Rio de Janeiro, April 5, 2010.

Master thesis committee:

Paulo Cezar Pinto Carvalho (advisor) - IMPA

Luiz Carlos Pacheco Rodrigues Velho (co-advisor) - IMPA

Marcelo Gattass - PUC-Rio

Luiz Henrique de Figueiredo (substitute) - IMPA

Acknowledgements

First of all, I would like to thank my mother for always supporting me, encouraging me and pushing me forward.

I would like to thank Professor Paulo Cezar Carvalho for guiding my studies during the last years and for giving valuable suggestions and contributions to this work.

I am grateful to Professor Luiz Velho for receiving me very well in the Visgraf Laboratory, for introducing me to the theme of this thesis, for giving great ideas for the development of this work and for providing key discussions about the theme.

I would also like to thank Professor Marcelo Gattass for helping me on the Computer Vision aspects of this work.

A more general acknowledgement to all Professors from IMPA and UFSC that contributed to my academic growth.

I want to thank all my colleagues from the Visgraf Lab that somehow helped me in this thesis: Thiago Pereira, Adriana Schulz, Djalma Lucio, Gabriel Duarte, Marcelo Cicconet, Francisco Ganacim and Leandro Cruz. Also, I want to thank all friends at IMPA for making the years of my masters studies not only constructive but also very pleasant.

I would like to thank all the people that work at IMPA and contribute to keeping it a place of excellence to study Mathematics.

I am very grateful to the Brazilian Government for giving me conditions to focus on my studies and CNPq for the financial support.

Resumo

Câmeras comuns geralmente capturam um campo de visão bastante limitado, por volta de noventa graus. A razão para este fato é que quando o campo de visão se torna maior, a projeção que estas câmeras usam começa a introduzir distorções não-naturais e não-triviais. Esta dissertação estuda estas distorções com a finalidade de obter imagens panorâmicas, isto é, imagens de grandes campos de visão.

Após modelar o campo de visão como uma esfera unitária, o problema passa a ser achar uma projeção de um subconjunto da esfera unitária em um plano de imagem, com propriedades desejáveis. Nós fazemos uma discussão aprofundada de Carroll et. al ([1]), no qual preservação de linhas retas e formas de objetos são colocados como as propiedades desejáveis principais e uma solução de otimização é proposta. A seguir, nós mostramos imagens panorâmicas obtidas por este método e concluímos que ele funciona bem numa variedade de cenas.

Esta dissertação também faz um estudo inovador sobre vídeos panorâmicos, isto é, vídeos nos quais cada quadro é construído a partir de um grande campo de visão. Nós introduzimos um modelo matemático para o problema, discutimos propriedades de coerência temporal desejáveis, formulamos equações que representam estas propriedades, propomos uma solução de otimização para um caso particular e apontamos direções futuras.

Palavras-chave: Esfera visível, imagens panorâmicas, vídeos panorâmicos.

Abstract

Common cameras usually capture a very narrow field of view (FOV), around ninety degrees. The reason for this fact is that when the field of view becomes wider, the projection that these cameras use starts introducing unnatural and nontrivial distortions. This thesis studies these distortions in order to obtain panoramic images, i.e., images of wide fields of view.

After modeling the FOV as a unit sphere, the problem becomes finding a projection from a subset of the unit sphere to the image plane, with desirable properties. We provide an in-depth discussion of Carroll et. al ([1]), where preservation of straight lines and object shapes are stated as the main desirable properties and an optimization solution is proposed. Next, we show panoramic images obtained by this method and conclude that it works well in a variety of scenes.

This thesis also provides a novel study about panoramic videos, i.e., videos where each frame is constructed from a wide FOV. We introduce a mathematical model for this problem, discuss desirable temporal coherence properties, formulate equations that represent this properties, propose an optimization solution for a particular case and point future directions.

Keywords: Viewing sphere, panoramic images, panoramic videos.

Contents

Introduction **1**

Motivation and Overview of the Problem 1

Goals 3

Original Contributions 3

Structure of the thesis: a time line 4

1 Panoramic images **6**

1.1 The Viewing Sphere 6

1.2 Problem Statement 10

1.3 Standard Projections 10

1.3.1 Perspective Projection 10

1.3.2 Stereographic Projection 13

1.3.3 Mercator Projection 14

1.4 Modified Standard Projections 15

1.4.1 Perspereographic Projections 16

1.4.2 Perspective Projection Centered on Other Points 18

1.4.3 Recti-Perspective Projection 19

1.5 Previous Approaches 20

1.5.1 Correction of Geometric Perceptual Distortions in Pictures 21

1.5.2 Artistic Multiprojection Rendering 23

1.5.3 Squaring the Circle in Panoramas 25

1.5.4 Other Approaches 27

2 Optimizing Content-Preserving Projections for Wide-Angle Images **28**

2.1 Desirable Properties 29

2.2 User Interface 31

2.3 Discretization of the Viewing Sphere 35

2.4 Conformality 36

2.4.1 Differential Geometry and the Cauchy-Riemann Equations 36

2.4.2 Examples 40

2.4.3 Energy Term 42

2.5 Straight Lines 44

2.5.1 Energy terms . . . 48
2.5.2 Inverting Bilinear Interpolation . . . 52
2.6 Smoothness . . . 56
2.6.1 Energy Term . . . 57
2.7 Spatially-Varying Weighting . . . 58
2.8 Minimization . . . 62
2.8.1 Total Energy . . . 63
2.8.2 Eigenvalue/Eigenvector Method . . . 63
2.8.3 Linear System Method . . . 65
2.8.4 Results in each iteration . . . 68

3 Results **73**
3.1 Result 1 . . . 74
3.2 Result 2 . . . 78
3.3 Result 3 . . . 82
3.4 Result 4 . . . 86
3.5 Result 5 . . . 90
3.6 Failure cases . . . 92
3.7 Result Discussion . . . 94

4 Panoramic Videos **97**
4.1 Overview . . . 97
4.2 The three cases . . . 98
4.3 Desirable Properties . . . 98
4.4 The Temporal Viewing Sphere and Problem Statement . . . 100
4.5 Transition Functions . . . 102
4.6 Case 1 - Stationary VP, Stationary FOV and Moving Objects . . . 104
4.6.1 Temporal Coherence Equations . . . 104
4.6.2 Discretization of the temporal viewing sphere . . . 106
4.6.3 Total energy, minimization and results . . . 107
4.6.4 Implementation Details . . . 113
4.6.5 Other Solutions . . . 115
4.7 Case 2 - Stationary VP, Moving FOV and Stationary Objects . . . 115
4.7.1 Temporal Coherence Equations . . . 115
4.7.2 A solution . . . 116
4.8 Concluding Remarks . . . 116

A Application Software **118**
A.1 Application and user's manual . . . 118
A.2 Implementation Details . . . 122
A.2.1 Window 1 . . . 123

A.2.2 Window 2 . . . 124
A.2.3 Matlab processing . . . 125

B Feature Detection in Equirectangular Images **128**
B.1 Automatic Face Detection in Equirectangular Images . . . 128
B.1.1 Robust Real-time Face Detection . . . 129
B.1.2 Method and Implementation . . . 133
B.1.3 Results . . . 135
B.1.4 Weight Field . . . 136
B.2 Semiautomatic Line Detection in Equirectangular Images . . . 137
B.2.1 The Hough Transform . . . 137
B.2.2 Bilateral Filter . . . 140
B.2.3 Eigenvalue Processing . . . 141
B.2.4 The Method . . . 143
B.2.5 Results . . . 148
B.2.6 Concluding remarks . . . 149

Conclusion **151**
Review . . . 151
Discussion . . . 152
Future Work . . . 153

Bibliography **155**

Introduction

Motivation and Overview of the Problem

This thesis studies the problem of obtaining perceptually acceptable panoramic images, which are images that represents wide fields of view.

One of the motivations for this problem is that common cameras capture just a limited field of view (FOV), usually near 90 degree longitude and 90 degree longitude, while our eyes see about 150 degree longitude and 120 degree latitude. When we see a photograph, it is as if we were seeing the world through a limited window. This limitation in common photographs happens because they are produced under a projection that approximates the perspective projection, which stretches objects too much for wide FOVs.

The panoramic images can be used to extrapolate our perception, since they can capture FOVs beyond the human eye. Also, a panoramic image allows us to better represent an entire scene. There may be important parts in a scene that could not be seen under a limited FOV.

The study of this topic became possible only recently with the development of stitching software and equipment ([2], [3] and [4]). With these techniques, it is possible to create an image of the entire *viewing sphere* centered at the viewpoint, an image that contains the visual information that is seen from this viewpoint in all possible directions. In figure 1 one can see an example of such image, which we call *equirectangular image*.

Once we have an image that represents the viewing sphere, what is left to be done is to find a projection from the sphere to the plane that results in a perceptually good result. Some previous works as [5], [6], [7], [4] and [8] considered this problem. The main difficulty that arises is to satisfy two important perceptual properties: preservation of shapes, i.e., objects in the scene should not appear too stretched in the final panoramic image, and preservation of straight lines, i.e., straight lines the scene should be mapped to straight lines in the final panoramic image.

The paper studied in depth in this thesis, named *Optimizing content-preserving projections for wide-angle images* ([1]), addresses these two properties by formulating energies that measure how a projection distorts shapes and bends lines. The user marks in an interface the lines she wants to be preserved and the method detect regions where the projection should preserve more shapes, as face regions for example. Based on this in-

Figure 1: Example of equirectangular image.

formation, the method formulates the energies and the minimizer of a weighted sum of these energies is the panoramic image that most satisfy these properties. An extra term for modeling the smoothness of the projection is necessary to avoid mappings that vary too much to satisfy the constrains. An example of panoramic image produced by this method is shown in figure 2.

Figure 2: Example of result produced by the method discussed in detail in this thesis.

This thesis is also concerned about the problem of obtaining perceptually acceptable panoramic videos. This theme has the motivations we already mentioned for panoramic images, but also it has more interesting practical applications. The development of ideas in this field could lead to new ways of filming, which could be applicable for cinema and sport broadcasting, for example.

Recently, capture devices that film a wide field of view were invented. An example of it can be found in [9]. These cameras return a video where each frame is an equirectangular image for the respective time. Again, what is left to be done is to project this set of viewing spheres (which we call *temporal viewing sphere*) to a set of images.

Very little work has been done on this subject. The strategy adopted in this thesis is to adapt the theory studied for images and include new desirable properties that model *temporal coherence*, in order to produce a perceptually good panoramic video.

Goals

This thesis has the following goals:

• **Study and understand the panoramic image problem:** In our work, we do a review of the methods proposed up to the moment, which is necessary to understand the difficulties and challenges of the problem.

• **Analyze in detail a reference on this topic:** After doing the review, we elected [1] as the main reference of this thesis because it satisfies most of the properties we state as desirable. All the details, even the ones that were omitted in the reference, are explained in this thesis.

• **Propose extensions to this reference:** Beyond detailing [1], we propose two extensions for it: feature detection on equirectangular images and panoramic videos.

• **Focus on mathematical aspects of the problem:** All the mathematical techniques related to the problem are discussed in details in this thesis. Perceptual aspects are also discussed and implementation aspects are left as appendix.

Original Contributions

We believe that the two most important contributions of our work are:

• **Statement, modeling and solutions for the panoramic video problem:** As far as we know, this thesis is the first work where the problem of obtaining a video where each frame represents a wide FOV is considered. We consider desirable properties for this problem, that depend on temporal coherence of the objects and of the entire scene, we model the problem as the one of finding a projection and we propose an optimization solution for a particular case. These contributions are all found in chapter 4.

• **An in-depth conclusive analysis of [1]:** As we already mentioned, [1] omits details of their method. This thesis makes a complete mathematical analysis of their work, and also a conclusive analysis based on the results produced by their method. This analysis is in chapters 2 and 3.

Our work has other contributions of less impact, but also important in the context of this thesis:

• **Line detection on equirectangular images:** We propose a method to semiautomatically detect straight lines of the world in equirectangular images. This detection was pointed as future work in [1] and helps the user in the task of marking lines. This contribution can be found in appendix B.

• **Application software:** We propose in this work an application software that has some features that the interface proposed in [1] does not have, such as specification of FOV, vertices and number of iteration. This application is explained in appendix A.

• **Perspereographic Projections:** We developed a set of projections that interpolates conformality and preservation of straight lines in a very intuitive way. It has the same purpose of the projection presented in [5], but is obtained in a much easier way. These projections are in section 1.4.1.

Structure of the thesis: a time line

The thesis is structured according to figure 3.

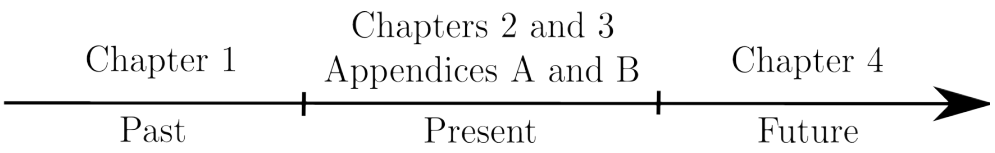

Figure 3: Structure of the thesis.

Chapter 1 starts with the statement of the panoramic image problem and then reviews many possibilities proposed to solve this problem until last year (2009). That is why we associate it to *past time*. The first solutions considered are the *standard projections*, which were developed centuries ago with other purposes but are applicable to the problem. Some modifications of them are also considered. Then we analyze previous approaches proposed in the last 15 years: [5], [6], [7], [4] and [8].

Motivated by chapter 1, we start chapter 2 by making a list of desirable properties a method to produce panoramic images should have and explain why [1] satisfies most

of them. Since [1] is very recent (it was published in SIGGRAPH 2009) we associate it to *present time*. Each section of this reference is discussed and theoretical details are rigorously posed.

In chapter 3, we show the results produced by the method. Good results are shown, each one illustrating some interesting feature of the method. Also, some failure cases are discussed.

In order to complement the discussion about [1], we provide two appendices. In appendix A, we show the application software we did to implement the method and give implementation details. Appendix B shows the methods we developed to detect faces and straight lines in equirectangular images. The Computer Vision and Image Processing techniques we used are explained.

We finish the thesis by discussing what we consider to be the *future* of this theme: panoramic videos. Chapter 4 is an initial step on this direction. We separate the problem in 3 cases, discuss and model undesirable distortions in panoramic videos and state the problem as finding a projection from the temporal viewing sphere to the 3-dimensional euclidian space. An optimization solution is proposed for case 1 and other possible solutions are discussed. Some initial results are provided.

Chapter 1

Panoramic images

A *panoramic image* or *wide-angle image* or *panorama* is an image constructed from a wide field of view. The *field of view* (FOV) is the angular extent of the observable world that is seen at any given moment.

In this chapter we model the field of view as a subset of a unit sphere centered at the viewpoint. From this, we derive standard projections from this sphere to an image plane and also show some modifications of them.

Motivated by the distortions that these mappings cause, we show some previous approaches that proposed methods to alleviate such problems.

This chapter can be seen as a detailed introduction to the panoramic image problem and its main goals are:

• Present and explain the necessary formalism (section 1.1);

• Clearly state the panoramic image problem (section 1.2);

• Discuss known projections and previous approaches in order to understand what properties are desirable in wide-angle images (sections 1.3, 1.4 and 1.5).

1.1 The Viewing Sphere

In this work, any scene observed from a fixed viewpoint at a given moment will be modeled as the unit sphere centered at the viewpoint ($\mathbb{S}^2 = \{(x, y, z) \in \mathbb{R}^3 | x^2 + y^2 + z^2 = 1\}$) on which each point has an associated color, the color that is seen when one looks toward this point. Here we assume that the viewpoint is the origin of $\mathbb{R}^3$ for convenience.

This sphere we will call the *viewing sphere*. Notice that the viewing sphere represents the whole 360 degree longitude by 180 degree latitude field of view. Figure 1.1 shows an example of viewing sphere.

Figure 1.1: A viewing sphere (looked from outside) that represents the visible information of some scene.

A very known and useful representation of $\mathbb{S}^2$ is the one by longitude and latitude coordinates[1]:

$$\begin{array}{rccl} \mathbf{r}: & [-\pi,\pi]\times\left[-\frac{\pi}{2},\frac{\pi}{2}\right] & \rightarrow & \mathbb{S}^2 \\ & (\lambda,\phi) & \mapsto & (\cos(\lambda)\cos(\phi),\sin(\lambda)\cos(\phi),\sin(\phi)) \end{array}$$

This representation is illustrated in figure 1.2.

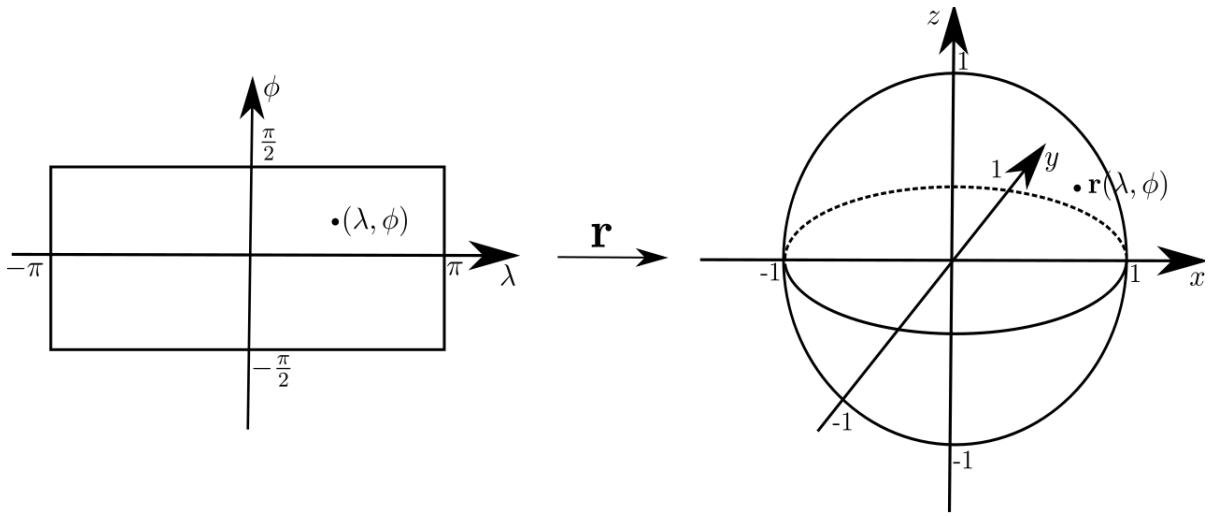

Figure 1.2: Longitude/latitude representation $\mathbf{r}$.

$\mathbf{r}$ gives us a way of representing all the information of a scene from a single viewpoint as the longitude/latitude rectangle $[-\pi,\pi]\times\left[-\frac{\pi}{2},\frac{\pi}{2}\right]$, which we will call the *equirectangular domain*.

[1] Also known as yaw and pitch values or pan and tilt values.

Recent development of stitching techniques made it possible to take many pictures of a scene and stitch them all together into an equirectangular domain that represents such scene. More specifically, from a set of photographs (common photographs or images obtained with fisheye lenses, for example) taken from the same viewpoint, it became possible to create an image in which every pixel represents a point and its associated color on the equirectangular domain.

The stitching process itself is a very detailed task and will not to be discussed in this work. However, it is important to notice that without the development of such techniques, it would not be possible to deal with projections from the viewing sphere to an image plane, which is one of the main tasks of this thesis. For additional information about stitching, we suggest references [2] and [3].

Such images of the equirectangular domain are called *equirectangular images* and will be the input information for all the algorithms that we will develop. Examples of equirectangular images are shown in figures 1.3, 1.4 and 1.5.

Figure 1.3: "San Marco Plaza", by Flickr user Veneboer, taken from [10].

Figure 1.4: "Reboot 8.0: Ianus demos Cabinet to Thomas' kid", by Flickr user Aldo, taken from [10].

Figure 1.5: "Cloud Gate", by Flickr user Wcm777, taken from [10].

The bottom left corner of the images (with coordinates $(x, y) = (m-1, 0)$) represents the point $\left(-\pi, -\frac{\pi}{2}\right)$, the top right corner ($(x, y) = (0, n-1)$) of the image represents the point $\left(\pi, \frac{\pi}{2}\right)$ and the center of the image ($(x, y) = (\frac{m-1}{2}, \frac{n-1}{2})$) represents the point $(0, 0)$ on the equirectangular domain, as illustrated in figure 1.6.

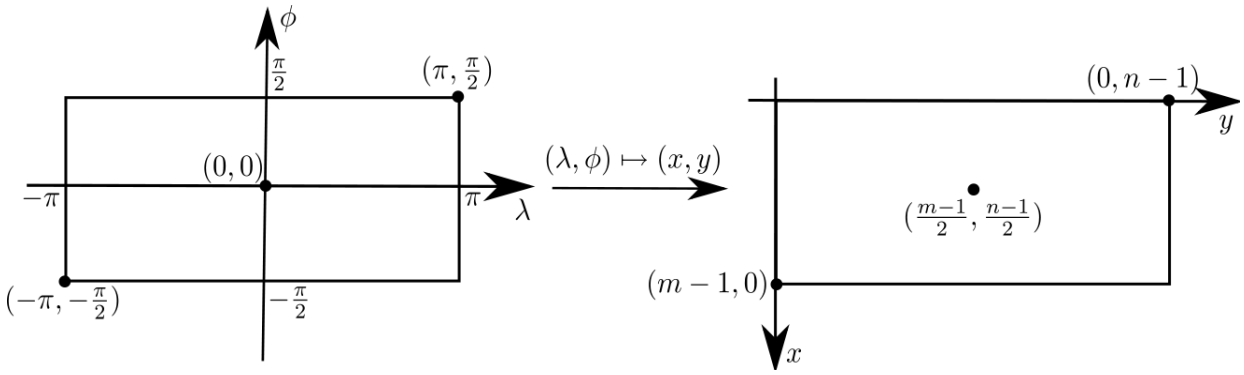

Figure 1.6: Correspondence between the equirectangular domain and the equirectangular image.

The correspondence between $[-\pi, \pi] \times \left[-\frac{\pi}{2}, \frac{\pi}{2}\right]$ and the equirectangular image is very simple:

$$(\lambda, \phi) \mapsto (x, y) = \left((m-1) - \left(\frac{\phi + \frac{\pi}{2}}{\pi}\right)(m-1), \left(\frac{\lambda + \pi}{2\pi}\right)(n-1)\right),$$

where m and n are the height and width of the equirectangular image and the image is assumed to have coordinates in $[0, m-1] \times [0, n-1]$. To keep the proportions of the equirectangular domain we impose $n - 1 = 2(m-1)$.

The inverse correspondence between the equirectangular image and $[-\pi, \pi] \times \left[-\frac{\pi}{2}, \frac{\pi}{2}\right]$ is immediate:

$$(x, y) \mapsto (\lambda, \phi) = \left(\frac{2\pi y}{n-1} - \pi, \frac{\pi}{2} - \frac{\pi x}{m-1}\right).$$

The equirectangular image shows the strong distortions that are caused by the mapping $\mathbf{r}$. For example, regions near $\phi = -\frac{\pi}{2}$ and $\phi = \frac{\pi}{2}$, which correspond to regions

near the south and north poles on the sphere, are too stretched. That happens because the sphere has a much smaller area near the poles, for some variation of ϕ, than near the equator ($\phi = 0$) for this same variation of ϕ. But these very different areas are represented by the same number of pixels on the equirectangular image.

To finish this discussion about equirectangular images, it is important to emphasize how popular this format of image became during the last years. Today it is possible to find thousands of them on photo sharing sites. To illustrate this point, the reader may, for example, access Flickr group on [10].

One can find there a great variety of equirectangular images: indoor or outdoor scenes, with or without people, realistic or with artistic effects, from places all around the world, in many different resolutions.

1.2 Problem Statement

With the formalism created in the last section we can formulate the panoramic image problem as the one of finding a mapping

$$\begin{array}{rccc} \mathbf{u}: & S \subseteq \mathbb{S}^2 & \rightarrow & \mathbb{R}^2 \\ & (\lambda, \phi) & \mapsto & (u, v) \end{array},$$

with desirable properties. Here S is a field of view which may not be the entire 360 by 180 degree entire field of view.

The set $\mathbf{u}(S)$ can be interpreted as a continuous image: each $\mathbf{u}(\lambda, \phi) \in \mathbf{u}(S)$ receives the color that the viewing sphere has at (λ, ϕ).

Thus we have two ways of thinking of a panoramic image: as a mapping $\mathbf{u}$ or as a continuous image $\mathbf{u}(S)$. This duality allows us to turn perceptual properties of the continuous image into algebraic expressions, that depend on the function $\mathbf{u}$.

1.3 Standard Projections

There are many known functions that project the viewing sphere (or a part of it) onto a plane. Many of them were developed for cartography purposes, since Earth's shape can be approximated by a sphere. There are different classifications for these projections (equal-area, conformal, cylindrical, etc.). For details about these classifications and many examples of projections, we recommend [11].

In this section we study the best known projections (Perspective, Stereographic and Mercator) and discuss their properties.

1.3.1 Perspective Projection

The result of a perspective projection is very well known because most of the photographs (taken with simple cameras) are captured by lenses that approximate linear

perspective, since this projection has many desirable properties that we are going to discuss further.

The construction of this projection is quite simple: the viewing sphere is projected onto a tangent plane (we are going to use the plane $x = 1$) through lines emanating form the center of the sphere, as shown in figure 1.7.

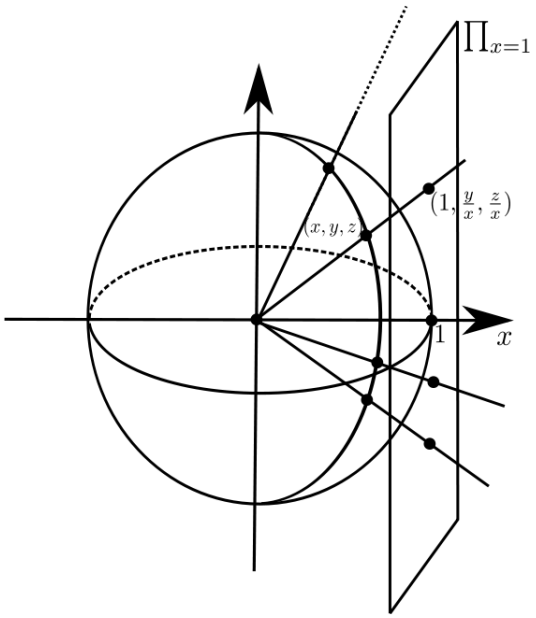

Figure 1.7: Perspective projection.

Thus $(x, y, z) \in \mathbb{S}^2$ is mapped to $\left(1, \frac{y}{x}, \frac{z}{x}\right) \simeq \left(\frac{y}{x}, \frac{z}{x}\right) \in \prod_{x=1}$, which consists in a simple division by the x coordinate. Observe that the mapping stretches to infinity when $x \to 0$ and is not defined when $x = 0$. So we define the perspective only for points with $x > 0$.

Since we want a mapping from the equirectangular domain to a plane, we have to convert the formula above to latitude/longitude coordinates: given $(x, y, z) \in \mathbb{S}^2$, $x > 0$, there is a $(\lambda, \theta) \in \left(-\frac{\pi}{2}, \frac{\pi}{2}\right) \times \left(-\frac{\pi}{2}, \frac{\pi}{2}\right)$ such that $(x, y, z) = (\cos(\lambda)\cos(\phi), \sin(\lambda)\cos(\phi), \sin(\phi))$ and the perspective projection is

$$(\cos(\lambda)\cos(\phi), \sin(\lambda)\cos(\phi), \sin(\phi)) \mapsto \left(1, \frac{\sin(\lambda)\cos(\phi)}{\cos(\lambda)\cos(\phi)}, \frac{\sin(\lambda)}{\cos(\lambda)\cos(\phi)}\right) = \left(1, \tan(\lambda), \frac{\tan(\phi)}{\cos(\lambda)}\right).$$

Hence, the final formula for the perspective projection is:

$$\begin{aligned} P: \left(-\frac{\pi}{2}, \frac{\pi}{2}\right) \times \left(-\frac{\pi}{2}, \frac{\pi}{2}\right) &\to \mathbb{R}^2 \\ (\lambda, \phi) &\mapsto (u, v) = \left(\tan(\lambda), \frac{\tan(\phi)}{\cos(\lambda)}\right) \end{aligned}$$

Figures 1.8 and 1.9 show some results of this projection with different fields of view.

Figure 1.8: Left: 90 degree long./90 degree lat.; Right: 120/120.

Figure 1.9: Left: 90 degree long./90 degree lat.; Right: 130/120.

The main advantages and disadvantages of the perspective projection are:

Advantages: • Straight lines in the scene appear straight on the final result;

• When the camera is held parallel to the ground the orientation constancy of the vertical lines is maintained, i.e., they appear vertical in the resulting image.

Disadvantages: • As the field of view increases, the shape of the objects near the periphery of the image starts to change considerably. This fact is noticeable even for FOVs which are not too wide, such as 120 degrees (see the right images in figures 1.8 and 1.9). The cause of this effect is that the perspective projection is not *conformal*, concept that we are going to formalize further. Informally, a mapping is conformal if it locally

preserves shapes of objects. The nonconformality of the perspective projection is the reason why simple photographs have a small field of view, usually less than 90 degrees.

1.3.2 Stereographic Projection

The geometric construction of the stereographic projection is the following: the viewing sphere is projected on the $x = 1$ plane (just as the perspective projection) through lines emanating from the pole opposite to the point of tangency, $(-1, 0, 0)$ in this case. So it is essentially the perspective projection but with lines coming from $(-1, 0, 0)$ instead of coming from $(0, 0, 0)$, as shown in figure 1.10.

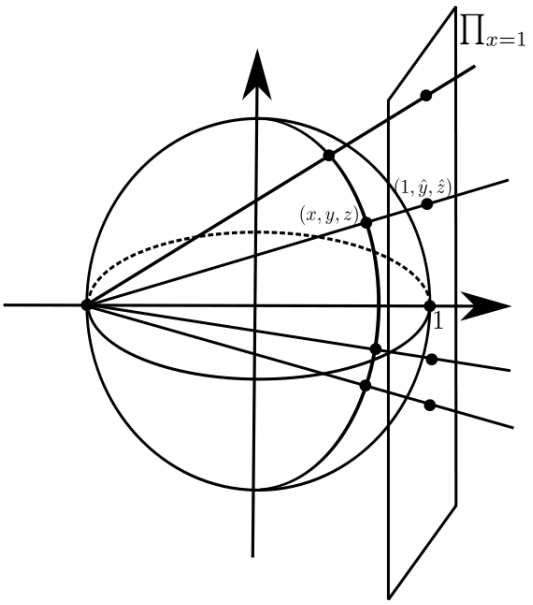

Figure 1.10: Stereographic projection.

If $(1, \hat{y}, \hat{z})$ is the projection of $(x, y, z) \in \mathbb{S}^2$, by similarity of triangles we obtain the following relations:

$$\frac{\hat{y}}{2} = \frac{y}{x+1}, \ \frac{\hat{z}}{2} = \frac{z}{x+1}.$$

Thus $(x, y, z) \in \mathbb{S}^2$ is mapped to $\left(1, \frac{2y}{x+1}, \frac{2z}{x+1}\right) \simeq \left(\frac{2y}{x+1}, \frac{2z}{x+1}\right) \in \prod_{x=1}$. Observe that the mapping is not defined at $(-1, 0, 0)$, the opposite pole to the tangent plane.

In longitude/latitude coordinates, we have:

$$(\cos(\lambda)\cos(\phi), \sin(\lambda)\cos(\phi), \sin(\phi)) \mapsto \left(1, \frac{2\sin(\lambda)\cos(\phi)}{\cos(\lambda)\cos(\phi)+1}, \frac{2\sin(\lambda)}{\cos(\lambda)\cos(\phi)+1}\right).$$

So the final formula for the stereographic projection is:

$$\begin{aligned} S: \ [-\pi, \pi) \times \left[-\frac{\pi}{2}, \frac{\pi}{2}\right] \setminus \{(-\pi, 0)\} &\to \mathbb{R}^2 \\ (\lambda, \phi) &\mapsto (u, v) = \left(\frac{2\sin(\lambda)\cos(\phi)}{\cos(\lambda)\cos(\phi)+1}, \frac{2\sin(\phi)}{\cos(\lambda)\cos(\phi)+1}\right) \end{aligned}$$

We show some results of this projection for different scenes in figure 1.11.

Figure 1.11: Left: 180 degree long./180 degree lat.; Right: 180/180.

The main advantages and disadvantages of the stereographic projection are:
Advantages: • Lines that pass through the center of the image are preserved;
• It is conformal, i.e., it preserves the shape of objects locally. Although the objects near the periphery of wide fields of view are stretched, this stretching is the same in all directions, which maintains the conformality of such mapping.
Disadvantages: • Most of the lines in the scene are bent on the final result.

1.3.3 Mercator Projection

This projection was presented by the flemish cartographer and geographer Gerardus Mercator, in 1569, with only cartography purposes in mind.

It is a cylindrical projection, which means that the u coordinate varies linearly with the longitude λ, and it is conformal. We are going to obtain its formula when we introduce the *Cauchy-Riemann equations* on the next chapter, in order to formalize what is a conformal mapping.

For the moment, it is just a cylindrical projection that preserve the shape of the objects. Its formula is the following:

$$\begin{array}{rccl} M: & [-\pi,\pi)\times\left(-\frac{\pi}{2},\frac{\pi}{2}\right) & \to & \mathbb{R}^2 \\ & (\lambda,\phi) & \mapsto & (u,v)=(\lambda,\log(\sec(\phi)+\tan(\phi))) \end{array}$$

Observe that the mapping tends to infinity when $\phi \to \pm\frac{\pi}{2}$.

Figures 1.12 and 2.8 show some results of this projection.

Figure 1.12: 360 degree longitude/150 degree latitude.

Figure 1.13: 360 degree longitude/150 degree latitude.

The main advantages and disadvantages of the Mercator projection are:
Advantages: • As in all cylindrical projections, meridians ($\{(\lambda, \phi) \in \mathbb{S}^2 : \lambda = \text{constant}\}$) are mapped to vertical lines.
• It is conformal.
• It handles wide longitude fields of view, even 360 degree ones.
Disadvantages: • Just as the stereographic projection, most of the straight lines in the scene are bent on the final result.

1.4 Modified Standard Projections

In the last section, we showed the three most known projections from the viewing sphere to an image plane. In this section, we show how simple modifications of these projections can generate better results.

1.4.1 Perspereographic Projections

As we mentioned before, perspective and stereographic projections have a lot in common. Actually, they are constructed in a very similar way, the only difference is that the point from where the rays emanate in the first is $(0,0,0)$ and in the second is $(-1,0,0)$.

We generalize the geometrical construction of these both projections as follows: for each $K \in [0,1]$ we define the *perspereographic projection for* K as being the one obtained by projecting points from the sphere on the $x = 1$ plane through rays emanating from $(-K,0,0)$. Figure 1.14 illustrates this projection.

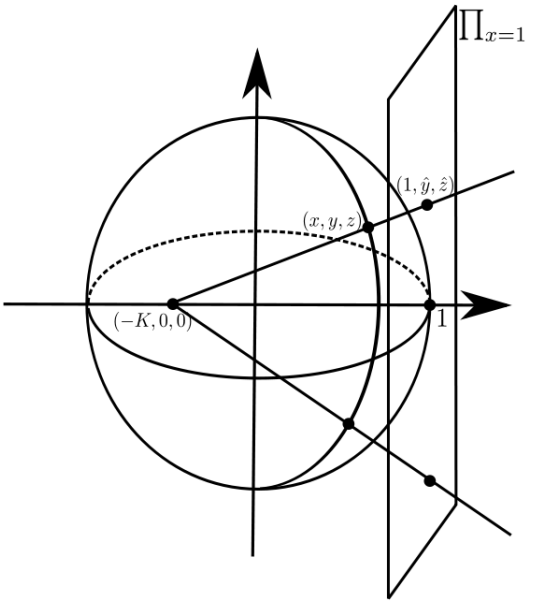

Figure 1.14: Perspereographic projection for K.

If $(1,\hat{y},\hat{z})$ is the projection of $(x,y,z) \in \mathbb{S}^2$, by similarity of triangles we obtain:

$$\frac{\hat{y}}{1+K} = \frac{y}{x+K},\ \frac{\hat{z}}{1+K} = \frac{z}{x+K} \Rightarrow \hat{y} = \frac{(1+K)y}{x+K}, \hat{z} = \frac{(1+K)z}{x+K}.$$

Obviously this projection is not defined for $(x,y,z) \in \mathbb{S}^2$ such that $x = -K$. To simplify, we are going to consider just the points s.t. $x > 0$.

In longitude/latitude coordinates:

$$(\cos(\lambda)\cos(\phi), \sin(\lambda)\cos(\phi), \sin(\phi)) \mapsto \left(1, \frac{(1+K)\sin(\lambda)\cos(\phi)}{\cos(\lambda)\cos(\phi)+K}, \frac{(1+K)\sin(\lambda)}{\cos(\lambda)\cos(\phi)+K}\right).$$

And the final formula is:

$$\begin{aligned} PS_K : \left(-\frac{\pi}{2},\frac{\pi}{2}\right) \times \left(-\frac{\pi}{2},\frac{\pi}{2}\right) &\to \mathbb{R}^2 \\ (\lambda,\phi) &\mapsto (u,v) = \left(\frac{(1+K)\sin(\lambda)\cos(\phi)}{\cos(\lambda)\cos(\phi)+K}, \frac{(1+K)\sin(\phi)}{\cos(\lambda)\cos(\phi)+K}\right) \end{aligned}$$

Notice that when $K = 0$ we have the perspective projection and for $K = 1$ we have the stereographic projection.

Some results are shown in figures 1.15 and 1.16.

Figure 1.15: Both with 150 degree long./150 degree lat. Left: $K = 0$; Right: $K = \frac{1}{3}$.

Figure 1.16: Both with 150 degree long./150 degree lat. Left: $K = \frac{2}{3}$; Right: $K = 1$.

The **advantages** of these new projections are the following:

• They give us an intuitive way to control the conformality and the preservation of straight lines in the scene. The greater the K the better the shapes of objects are preserved, and the extreme case, $K = 1$, leads to the stereographic projection, which is conformal. On the other hand, when lower values for K are used, straight lines become less bent and objects more stretched. The extreme case, $K = 0$, leads to perspective projection. Therefore the parameter K can be adjusted according to the scene and FOV that is being projected.

• The value K could depend on the points on the sphere. Thus we would have K as a function of (λ, ϕ), $K(\lambda, \phi)$. This idea allows the possibility of having a projection locally

adapted to the image content. Possibly $K(\lambda, \phi)$ should have some degree of smoothness and such analysis and results for this approach are going to be left as future work.

1.4.2 Perspective Projection Centered on Other Points

The perspective projection shown on section 1.3.1 preserves well only the shape of objects that are near the point with $(\lambda, \phi) = (0, 0)$, the center of such projection.

As we'll see in further sections, one may want to use perspective projection but preserve shapes of other objects that are not near $(\lambda, \phi) = (0, 0)$. That leads to constructing perspective projections centered on $(\lambda_0, \phi_0) \neq (0, 0)$. The geometrical construction is analogous to the one presented on section 1.3.1.

Let $(x_0, y_0, z_0) = (\cos(\lambda_0)\cos(\phi_0), \sin(\lambda_0)\cos(\phi_0), \sin(\lambda_0))$,
$(x, y, z) = (\cos(\lambda)\cos(\phi), \sin(\lambda)\cos(\phi), \sin(\lambda)) \in \mathbb{S}^2$. The tangent plane to $\mathbb{S}^2$ passing through (x_0, y_0, z_0) has the following equation:

$$\prod : x_0(x - x_0) + y_0(y - y_0) + z_0(z - z_0) = 0 \ \left(\prod : x_0 x + y_0 y + z_0 z = 1\right)$$

since $(x_0, y_0, z_0) \perp \prod$. We illustrate the projection in figure 1.17.

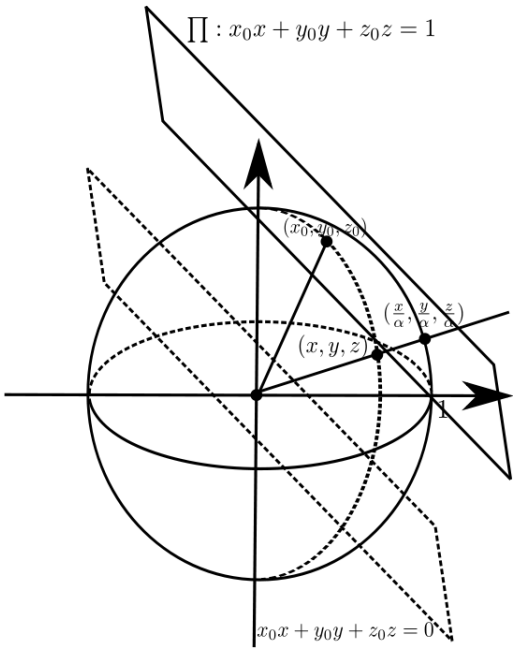

Figure 1.17: Perspective projection centered on (λ_0, ϕ_0).

We want to project (x, y, z) radially in $\prod$, i.e., we want to find α s.t. $\left(\frac{x}{\alpha}, \frac{y}{\alpha}, \frac{z}{\alpha}\right) \in \prod$, which is equivalent to

$$x_0\left(\frac{x}{\alpha} - x_0\right) + y_0\left(\frac{y}{\alpha} - y_0\right) + z_0\left(\frac{z}{\alpha} - z_0\right) = 0.$$

Solving the above equation leads to

$$\alpha = (x_0 x + y_0 y + z_0 z) = (\cos(\phi_0)\cos(\phi)\cos(\lambda_0 - \lambda) + \sin(\phi_0)\sin(\phi)).$$

So the projection $(x, y, z) \mapsto \left(\frac{x}{\alpha}, \frac{y}{\alpha}, \frac{z}{\alpha}\right)$ has the following form in (λ, ϕ) coordinates:

$$(\lambda, \phi) \mapsto \left(\frac{\cos(\lambda)\cos(\phi)}{\cos(\phi_0)\cos(\phi)\cos(\lambda_0 - \lambda) + \sin(\phi_0)\sin(\phi)}, \right.$$

$$\left. \frac{\sin(\lambda)\cos(\phi)}{\cos(\phi_0)\cos(\phi)\cos(\lambda_0 - \lambda) + \sin(\phi_0)\sin(\phi)}, \frac{\sin(\lambda)}{\cos(\phi_0)\cos(\phi)\cos(\lambda_0 - \lambda) + \sin(\phi_0)\sin(\phi)} \right).$$

Observe that the projection is not well defined for $(x, y, z) \in \mathbb{S}^2$ s.t. $x_0x + y_0y + z_0z = 0$, the plane that is parallel to $\prod$ and passes through zero. This also happened for the simple perspective projection: the points s.t. $x = 0$ could not be projected in $\prod_{x=1}$.

The final projection is in $\mathbb{R}^3$ and we would like it to have a 2D coordinate system. This is achieved by performing two rotations on $\prod$ in order to transform it in $\prod_{x=1}$, for example. We will not expose the details of this process here.

We show in figure 1.18 a result where the center object (the tower) appears less stretched than in the standard perspective projection (right image in figure 1.8).

Figure 1.18: Perspective centered on $(\lambda, \phi) = (-\frac{\pi}{3}, \frac{\pi}{9})$.

1.4.3 Recti-Perspective Projection

This projection, also known as *Pannini projection*, is a modification of the perspective projection that is designed to handle wider FOVs and preserve radial and vertical lines. The other lines appear bent on the final result.

Let u and v be the coordinates of the standard perspective projection and u' and v' the coordinates of recti-perspective projection. The modification

$$u' = \alpha \tan\left(\frac{\lambda}{\alpha}\right),$$

where *alpha* is a chosen parameter, allows this projection to handle wider FOVs and preserves vertical lines (λ constant $\Rightarrow$ u' constant).

In order to preserve radial lines, the v coordinate of the perspective projection must be scaled by a constant multiple of the factor used to scale the u axis, i.e.,

$$v' = \gamma v, \ \gamma = \beta \left(\frac{u'}{u} \right),$$

where β is a chosen parameter. The above expressions lead to

$$v' = \frac{\left(\beta \alpha \tan\left(\frac{\lambda}{\alpha}\right) \tan(\phi) \right)}{\sin(\lambda)}, \text{ if } \lambda \neq 0,$$

and

$$v' = \beta \tan(\phi), \text{ if } \lambda = 0.$$

We show in figure 1.19 a good result obtained setting $\alpha = 2$ and $\beta = \frac{3}{4}$:

Figure 1.19: 180 degree longitude/130 degree latitude.

1.5 Previous Approaches

As pointed in last sections, it is not an easy task to obtain an image from a wide field of view. We showed some of the most known projections from the sphere to an image plane and realized that all of them have their advantages and disadvantages.

This section is devoted to discuss previous approaches created during the last years to deal with the problem of distortions in panoramic images. We do not intend to get into too many details of each approach, but we intend to show their key ideas in order to motivate the next chapter. Thus, this section is intended to be a review and a motivation.

We chose to discuss three papers that we understand to have the key ideas on the development of this theme: [5], [6] and [7]. At the end of the section, we mention some other important related work.

1.5.1 Correction of Geometric Perceptual Distortions in Pictures

This work by Zorin and Barr ([5]) is surely one of the most referenced in this area. It is probably the first work to apply perceptual principles to the analysis and construction of planar images of the 3D world. Their theory is even more applicable for panoramic images, where deviations of perception are more present.

The authors mention that the most important features that an image should have to be representative are the *structural features* such as dimension (whether the image of an object is an area, a curve or a point) and presence or absence of holes and self-intersections. They make the following statement:

> *The retinal projections of an image of an object should not contain any structural features that are not present in any retinal projection of the object itself.*

Since most of the visual informations that we have are in the images formed on the retina, this statement asks that when we look at an image the objects should not contain any structural feature that we would not see if we looked directly at them.

They selected three *structural requirements* to develop their theory:

• The image of a surface should not be a point;

• The image of a part of a straight line either should not have self intersections (loops) or else should be a point;

• The image of a plane should not have twists on it, i.e., either each point of the plane is projected to a different point in the image, or the whole plane is projected to a curve.

Figure 1.20 illustrates the last two requirements:

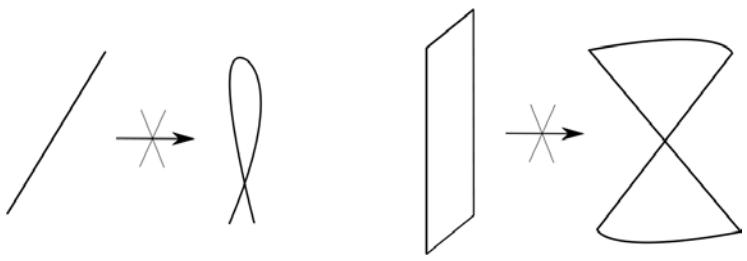

Figure 1.20: Mappings forbidden by the last two requirements.

They also state *desirable conditions*. These are not as essential as the structural ones because they can be changed with some intervals of tolerance. The desirable conditions are the following:

• **Zero-curvature condition:** Images of all possible straight lines should be straight;

• **Direct view condition:** All possible objects in the image should look as if they were viewed directly - as if they appeared in the middle of a photograph.

The authors obtain two functionals, K and D, that measure how much a mapping T_{sphere} from the viewing sphere to a plane does not respect both conditions. So ideally we should find a map such that:

$$K(T_{sphere}) = D(T_{sphere}) = 0;$$

After a theoretical development, it is shown that there is no T_{sphere} satisfying these conditions and also the structural requirements. Then they suggest to minimize the functional

$$F(T_{sphere}) = \mu K(T_{sphere}) + (1-\mu)D(T_{sphere}),$$

where μ is the desired tradeoff between both desirable conditions.

An approximate minimizer for this functional is a perspective projection of the viewing sphere followed by a one-to-one smooth transformation of the image plane given by:

$$\rho = \lambda \frac{r}{R} + (1-\lambda)\frac{R(\sqrt{r^2+1}-1)}{r(\sqrt{R^2+1}-1)};\ \psi = \phi,$$

where (r, ϕ) is the polar coordinate system of the perspective image, (ρ, ψ) is the polar coordinate system of the transformed image, λ is a parameter that depends on μ and R depends on the FOV that is being projected.

Some results for different values of λ are shown in figures 1.21 and 1.22.

Figure 1.21: Both: 150 degree longitude/150 degree latitude. Left: $\lambda = 0$ (very similar to stereographic projection); Right: $\lambda = 1$ (perspective projection).

Figure 1.22: Both: 150 degree longitude/150 degree latitude. Left: $\lambda = \frac{1}{2}$; Right: Perspereographic projection for $K = \frac{1}{2}$. Both have the same purpose of controlling the conformality and straight lines in the scene. Which one is better? The choices $\lambda = \frac{1}{2}$ and $K = \frac{1}{2}$ are arbitrary.

The key ideas that we can take from this work are: a panoramic image should respect the structural requirements; no panoramic image (mapping from the viewing sphere to a plane) that satisfies the structural requirements can satisfy completely both desirable properties at the same time; an optimization framework is an option for the task of minimizing all the important distortions.

1.5.2 Artistic Multiprojection Rendering

As we have already mentioned, perspective projection causes too much distortion for wide-angle fields of view. A simple and effective alternative to such problem is to render the most distorted objects in a different way.

This alternative was already known and used by painters hundreds of years ago, for example, in Raphael's *School of Athens* (Figure 1.23). The humans in the foreground would appear too distorted if rendered with the same perspective projection of the background. So Raphael altered the projections of the humans to give each one a more central perspective projection. This choice did not take off (actually improved) the realism of the painting.

This work by Agrawala, Zorin and Munzner ([6]) suggests using the same method for computer-generated images and animations: a scene is rendered using a set of different cameras. One of this cameras is elected to be the *master camera*, which is going to be used to render the background, and the other ones are the *local cameras*, which are going to be used to render the objects in the scene.

The visibility is not a well defined problem in this context. They use the visibility

Figure 1.23: Raphael's *School of Athens*.

ordering of the master camera to solve this problem: a point will be rendered if it is visible for the master camera.

The key idea that we have to take from this paper is that a special treatment can be given to the objects in order to reduce their distortion in panoramic images. But the multiprojection rendering has also other applications:

• **Artistic Expression:** The usage of different viewpoints was used by painters also to express feelings, ideas and mood.

• **Best Views:** A good viewpoint for an object may not be the best viewpoint for other objects. By choosing the best viewpoint for each object in the scene it's possible to improve the representation of the scene.

The author of this thesis, in a final course project, adapted the techniques described in this article for real world scenes in the following way: a set of equirectangular images (views) is given to the user so he can choose a different perspective (camera) for each view, by setting the FOV and the center point of each perspective. A screenshot of the first window of the user interface is shown in figure 1.24.

In the next windows, the user specifies which of the perspectives is the best view for each object and the program tries to solve the visibility problem for the master camera. An output of the program is the right image in figure 1.25, where I rendered myself with a local camera (perspective projection centered on me), to correct my distortions on the left image.

The reader may check the home page with more results and details of this project: [12].

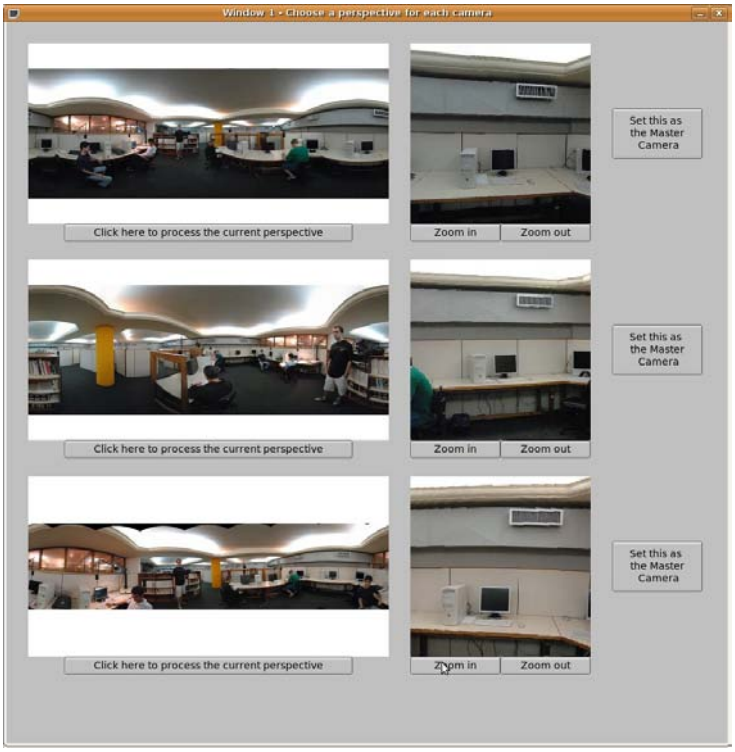

Figure 1.24: First window of the interface of the S3D project.

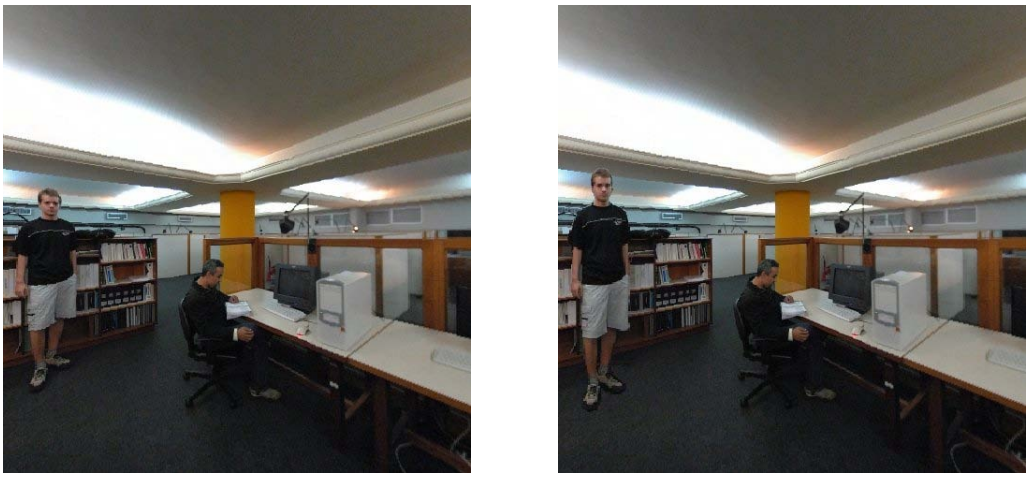

Figure 1.25: Both: 90 degree longitude/90 degree latitude. Left: Standard perspective projection; Right: Me (black t-shirt) corrected with a different perspective.

1.5.3 Squaring the Circle in Panoramas

The key idea of this article by Zelnik-Manor, Peters and Perona ([7]) is the one of constructing a projection that depends more on the structure of the entire scene, not only where the objects are, like the previous approach we just presented.

They start by discussing global projections (the ones we have already discussed under the name of standard projections), and suggest a multi-plane projection that is constructed in the following way: multiple tangent planes are positioned around the sphere and each region of the viewing sphere is projected via perspective projection onto its corresponding tangent plane. This construction is illustrated in figure 1.26.

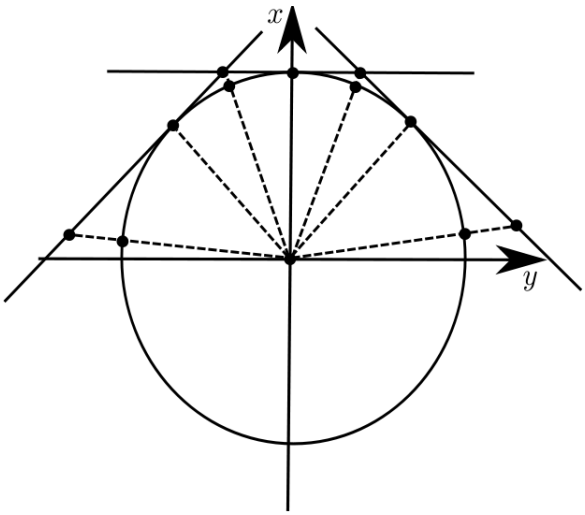

Figure 1.26: Top view of the multiplane projection.

To unfold this projection on a plane without distortions, one could think of the intersections of the planes being fitted with hinges that allow flattening.

The advantages of this new projection are that it preserves the straight lines that are mapped entirely in one single plane and it uses perspective projections only for limited fields of view, which avoids distortions caused by the global perspective projection.

This process causes discontinuities of orientation along the seams (intersections between tangent planes). This problem can be well hidden for scenes that naturally have such discontinuities, like man-made environments. Then the tangent planes must be chosen in a way that fits the geometry of the scene, usually so that vertical edges of a room project onto the seams and each projection plane corresponds to a single wall. A result of the multi-plane projection is shown in figure 1.27.

Figure 1.27: 180 degree longitude/90 degree longitude. Source image: "Posters", by Flickr user Simon S., taken from [10].

Under this projection the objects on the scene still may appear distorted on the final result for two reasons: if an object falls on a seam, it will have a discontinuity of orientation on it, which is very unnatural; or even for reduced FOVs, the perspective projection still

can distort objects..

The solution adopted for these two kinds of distortion is very similar to the one used on [6]: the background is rendered using the multi-plane projection and the objects are rendered each one using a local perspective projection centered on it.

The author of this thesis implemented most of the techniques contained in this article in his Image Processing course final project. The reader can see the details in [13].

1.5.4 Other Approaches

In this section we expose very briefly three other approaches ([14], [4] and [8]) that also deal with the problem of constructing panoramic images:

1) Photographing Long Scenes with Multi-Viewpoint Panoramas ([14])**:** This work addresses the problem of making a single image of a long planar scene (the buildings of one side of a street, for example) having as input a set of photographs taken from different viewpoints. Although this problem is different from the one we are concerned about in this thesis (here the input comes from a single viewpoint), it faces similar difficulties, such as preserving shapes of objects and making the final result a comprehensive representation for the scene.

2) Capturing and Viewing Gigapixel Images ([4])**:** This article presents a viewer that interpolates between cylindrical and perspective projection as the FOV is increased or decreased. The ability for zooming in and out panoramas is more useful when the input has high resolution. We think that the perspereographic projection presented in section 1.4.1 is a simpler solution for this task and could also produce good results.

3) Locally Adapted Projections to Reduce Panorama Distortions ([8])**:** This work starts with a cylindrical projection of a scene and allows the user to mark regions where he or she wants the projection to be near-planar. Then the method computes a deformation of the projection cylinder that fits such constraints and smoothly varies between different regions and unfold the deformed cylinder on a plane. Although their results are very good in many cases and produced quickly via optimization, their method has limitations: if some marked region occupies a wide-angle FOV (up to 120 degrees) the final result starts suffering with the same limitations as perspective projection (stretching of objects); a good solution depends on the precision of the user in marking regions; even inside the marked regions lines may appear slightly bent; and if two marked regions are too close, orientation discontinuities may appear between these regions, similarly to the method presented in section 1.5.3.

Chapter 2

Optimizing Content-Preserving Projections for Wide-Angle Images

In this chapter we show and discuss in more depth the ideas presented in Carroll et al. ([1]), which we believe to be the state-of-the-art reference for the panoramic image problem. Many details that are going to be exposed here do not appear in the original reference, which makes this chapter a good complement for it. We show in figure 2.1 a result produced by this method.

Figure 2.1: A result produced by the method described in this chapter. FOV: 285 degree longitude/170 degree latitude. Observe how most of the lines in the scene are straight and the shape of the objects is well preserved.

Motivated by chapter 1, we start this chapter by making a list of desirable properties in panoramic images and how this approach satisfies most of them.

Then we detail each section of the article in a mathematical way: all the necessary definitions and theorems are going to be stated. The pre-requisites for understanding the

theory are going to be mentioned progressively. For the moment, we assume the reader is familiar with multi-variable calculus and linear algebra.

The only parts of the article that are not explored in this chapter are the results and implementation. The first topic is left to Chapter 3, where a discussion about it is provided. We leave to Appendix A the details about how we implemented the method we are going to describe here.

To summarize, the main goals of this chapter are:

• To list the main desirable properties in wide-angle images (section 2.1);

• To make an as complete as possible mathematical explanation for the techniques in [1] (all the other sections of this chapter).

2.1 Desirable Properties

This section is devoted to argument why we consider [1] the best method for dealing with panoramic images and why a study in depth about it is worthy.

We believe a method to produce wide-angle images should have the following characteristics:

• **Depend on the scene content:** As we saw in sections 1.3 and 1.4, global projections produce distortions. One of the reasons for this fact is that they do not give a special treatment for different regions of the panorama. Some previous approaches (sections 1.5.2 and 1.5.3) tried to do something like this, but they did it in a coarse way. This approach constructs a wide-angle image adapted to the location of lines (sections 2.2, 2.5 and 2.7), faces (sections 2.7 and B.1) and importance of regions on the scene (section 2.7).

• **Handle wide fields of view:** Some standard projections and previous approaches are only defined for fields of view up to 180 degree and some of them produce bad results even for narrower FOVs. This approach does not have this problem and can handle arbitrary FOVs, as can be seen in chapter 3.

• **Satisfy the structural requirements:** In section 1.5.1 we stated requirements that a wide-angle image should have in order to match our perception of the world, since they are based on the retinal projections. We do not devote any special discussion to them here but we will always be careful to weather the method satisfy them or not.

• **Have a simple user interface:** Although not emphasized in the last chapter, some previous approaches (sections 1.5.2, 1.5.3 and 1.5.4(3)) needed a precise and/or tedious interaction with the user in order to yield a good result. The interface proposed in this approach requires the user only to click the endpoints of a lines in the real world and set

their orientation. Details are presented in sections 2.2 and A.1.

• **Mathematically formalize distortions and use an optimization framework:** Many previous approaches used just intuitive and classical ideas for minimizing distortions as, for example, centering projections on objects. A more precise solution would be to mathematically formalize these distortions and try to minimize them all, in the way we saw in section 1.5.1. All this chapter is devoted to develop such optimization solution.

• **Preserve straight lines:** It is very unnatural and noticeable if a line that is supposed to be straight in the final result appears bent. That happens because we perceive all straight lines in the real world as straight. This approach handles this task by allowing the user to mark curves on the equirectangular image that should map to straight lines on the final result (section 2.2), by obtaining an energy that measures how much a marked curve is not straight in the final result (section 2.5) and then minimizing this energy with other energies (section 2.8).

• **Have orientation consistency:** Another undesirable effect related to lines is when a line that is supposed to have some orientation (like the corner between walls or a tower are supposed to be vertical) appear with another orientation in the result. This approach avoids this problem by allowing the user to specify the orientation of lines (section 2.2) and by obtaining an energy that measures how much a line deviates from the assigned direction (section 2.5.1).

• **Preserve shape of objects:** Object distortion is another very unpleasant effect that may appear in wide-angle images. Previous approaches (sections 1.5.2 and 1.5.3) tried to fix this problem by locally correcting the projection of objects. This approach formalizes the concept of preservation of object shapes through the mathematical concept of *conformality*. Section 2.4 is devoted to explain such concept and obtain an energy that measures how conformal a panoramic image is. This energy is minimized together with other energies in section 2.8.

• **Vary scale and orientation smoothly**: Discontinuities of scale and orientation may be unpleasant. For example, when the approach in section 1.5.3 is applied to scenes that do not have some natural discontinuity the result is not good (the unnatural discontinuities can be noticed on the ceiling of the scene in figure 1.27, for example). In section 2.6 we describe an energy that measures how smooth a panoramic image is. This energy is also minimized with other ones.

• **Avoid restrictions to some particular structure of scene:** The method should

produce good results in a variety of scenes and it should not be restricted to some special kinds of scene. All previous approaches suffered from this problem in different degrees. As we will see in chapter 3, this new approach succeeds in this task. That happens because all the important distortions are considered and well modeled. Also, this method depends on parameters, and it is not desirable when one has to find a set of parameters that work well for different scenes. As we will see in in chapter 3, this approach works well with a fixed set of parameters.

• **Produce results fast:** This is the only property listed here that is not satisfied by this approach. It is the price we have to pay in order to obtain a really precise result. In chapter 3 we show that each result took about one or two minutes to be computed. Although one can see it as a problem, we think that it is an incentive to study the numerical details and implementation of the method and develop tools and theory in order to reduce computation time.

2.2 User Interface

The interface that will be shown here allows the user to identify linear structures in the equirectangular image and mark them. Then the method will focus on making only this specified linear structures to be straight in the final result, which is a more intelligent solution than trying to make straight all possible lines, as the perspective projection.

A central question here is: given two points $P_1^{(w)}, P_2^{(w)} \in \mathbb{R}^3$ what is the projection of the line segment $(r^{(w)})$ connecting them on the viewing sphere? See the illustration in figure 2.2.

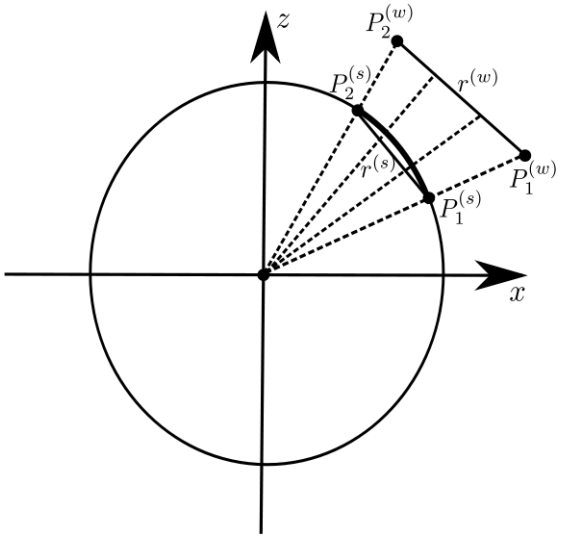

Figure 2.2: Projection of lines from the scene to the viewing sphere. Points $P_1^{(w)}$ and $P_2^{(w)}$ are projected to $P_1^{(s)}$ and $P_2^{(s)}$ on the sphere. We denote by $r^{(s)}$ the line segment connecting $P_1^{(s)}$ to $P_2^{(s)}$.

The *key observation* is that $r^{(w)}$ and $r^{(s)}$ project to the same points on the viewing sphere (the arc connecting $P_1^{(s)}$ and $P_2^{(s)}$ on the sphere). So we can work just with the points $P_1^{(s)}$ and $P_2^{(s)} \in \mathbb{S}^2$, which will be corresponding points to the ones marked by the user on the equirectangular image.

A very simple parametrization for $r^{(s)}$ is:

$$\begin{aligned} r^{(s)}: \ [0,1] &\to \mathbb{R}^3 \\ t &\mapsto (1-t)P_1^{(s)} + tP_2^{(s)} \end{aligned}.$$

The projection of $r^{(s)}$ on $\mathbb{S}^2$ (say $\gamma^{(s)}$) also has a simple parametrization:

$$\begin{aligned} \gamma^{(s)}: \ [0,1] &\to \mathbb{S}^2 \\ t &\mapsto \frac{(1-t)P_1^{(s)} + tP_2^{(s)}}{\| \ (1-t)P_1^{(s)} + tP_2^{(s)} \ \|} \end{aligned}.$$

We have to bring these calculations to the equirectangular domain: The user marks two points

$$(\lambda_1, \phi_1) \text{ and } (\lambda_2, \phi_2) \in [-\pi, \pi] \times \left[-\frac{\pi}{2}, \frac{\pi}{2}\right],$$

which have the following corresponding points on $\mathbb{S}^2$:

$$\begin{aligned} P_1^{(s)} &= (\cos(\lambda_1)\cos(\phi_1), \sin(\lambda_1)\cos(\phi_1), \sin(\phi_1)) \text{ and} \\ P_2^{(s)} &= (\cos(\lambda_2)\cos(\phi_2), \sin(\lambda_2)\cos(\phi_2), \sin(\phi_2)). \end{aligned}$$

Let $\gamma^{(s)}$ as above. For each $\gamma^{(s)}(t) = (x(t), y(t), z(t)) \in \mathbb{S}^2$, $t \in [0,1]$, we have to find the corresponding $(\lambda(t), \phi(t)) \in [-\pi, \pi] \times \left[-\frac{\pi}{2}, \frac{\pi}{2}\right]$.

Let $t_0 \in [0,1]$ and $\gamma^{(s)}(t_0) = (x, y, z)$ and (λ, ϕ) the corresponding longitude and latitude on the equirectangular domain. Then we have the following relation

$$(x, y, z) = (\cos(\lambda)\cos(\phi), \sin(\lambda)\cos(\phi), \sin(\phi)).$$

Obviously

$$\phi = \arcsin(z).$$

To obtain λ we first consider $x > 0$: in this case we must have $-\frac{\pi}{2} < \lambda < \frac{\pi}{2}$ and the relation

$$\frac{y}{x} = \frac{\sin(\lambda)\cos(\phi)}{\cos(\lambda)\cos(\phi)} = \tan(\lambda)$$

implies $\lambda = \arctan\left(\frac{y}{x}\right)$.

Now consider $x < 0$, $y < 0$: for such points on the sphere we must have $-\pi < \lambda < -\frac{\pi}{2}$ and $\lambda = \arctan\left(\frac{y}{x}\right) - \pi$ satisfies such inequality and the relations between x, y and λ. Analogously, for $x < 0$ and $y \geqslant 0$ the solution is $\lambda = \arctan\left(\frac{y}{x}\right) + \pi$.

For points s.t. $x = 0$, $y < 0$ the correspondent longitude is $\lambda = -\frac{\pi}{2}$ and for $x = 0$, $y > 0$ we have $\lambda = \frac{\pi}{2}$. To summarize:

$$\lambda = \arctan 2(y, x),$$

where

$$\arctan 2(y,x) = \begin{cases} \arctan\left(\frac{y}{x}\right) & , \quad x > 0 \\ \arctan\left(\frac{y}{x}\right) - \pi & , \quad x < 0, y < 0 \\ \arctan\left(\frac{y}{x}\right) + \pi & , \quad x < 0, y \geqslant 0 \\ -\frac{\pi}{2} & , \quad x = 0, y > 0 \\ \frac{\pi}{2} & , \quad x = 0, y < 0 \end{cases}$$

Beyond allowing the user to specify lines[1] in the equirectangular domain, the interface also allows her to set the orientation of the lines by typing 'v' (for vertical lines), 'h' (for horizontal lines) or 'g' (for lines with no specified orientation). As we mentioned in section 2.1, it is important that the final result has *orientation consistency*. If it were not possible to set line orientations, the final panoramic image would be like figure 2.3.

Figure 2.3: A result produced by the method if the user had only marked lines with no specified orientation. It seems that the tower is falling, for example. In order to avoid such problem, we give the user the possibility to specify the orientation of lines that she wants to be vertical or horizontal on the final result.

To summarize, our interface works in the following way:

- Input: Equirectangular image;
- For each line the user identifies
  - The user clicks the two endpoints (λ_1, ϕ_1), (λ_2, ϕ_2) on the equirectangular image;
  - The program computes $P_1^{(s)}$, $P_2^{(s)}$, $\gamma^{(s)}$, $(\gamma(t), \phi(t))$, $t \in [0,1]$, and draws in black the curve $(\lambda(t), \phi(t))$ on the equirectangular image;

[1] Here *line* stands for both $r^{(s)}$ and $\gamma^{(s)}$.

    - The user types ‘v’, ‘h’ or ‘g’ for the orientation and the color of the curve changes.
- Output: Marked equirectangular image and a list of points[2].

We show in figure 2.4 an image produced by the process just explained:

Figure 2.4: Equirectangular image with lines marked by the user. Red lines stands for vertical lines, blue for horizontal ones and green for general orientation ones.

For such marked lines, the method produces the result shown in figure 2.5.

Figure 2.5: Observe that line orientation is correct now. For example, the tower appears vertical on the result, because the user specified such behavior.

[2]The details of this list are left to section A.2.

The implementation details can be found in section A.2.

In our opinion, this interface satisfies the requirement of being simple and intuitive. The tasks of clicking endpoints and setting orientations are simple and the procedure to mark all the lines takes about one minute long.

We try to automate this procedure in section B.2 with the help of Computer Vision techniques. It turns out that the obtained results are a good initial guess for lines, which may help the user, avoiding her to have to mark all the lines.

One final remark is that the interface showed here is simpler than the one implemented in [1]. Our input is an equirectangular image that represents the entire viewing sphere. In [1] the input may have arbitrary FOVs and other formats, not only equirectangular. Despite simpler, our interface serves our purposes well.

2.3 Discretization of the Viewing Sphere

For the rest of this chapter we assume $S = \mathbb{S}^2$, i.e., the field of view that will be projected is the entire viewing sphere. All the development is analogous if restricted to some narrower FOV, since such FOV corresponds to a rectangle on the equirectangular domain.

In section 1.2 we stated the panoramic image problem as the one of finding

$$\begin{array}{rccc} \mathbf{u}: & \mathbb{S}^2 & \to & \mathbb{R}^2 \\ & (\lambda, \phi) & \mapsto & (u(\lambda,\phi), v(\lambda,\phi)) \end{array},$$

where (λ, ϕ) are in the equirectangular domain and (u, v) are cartesian coordinates that represent position on the image plane.

Instead of finding a function defined in all equirectangular domain, we discretize it in a uniform manner and look for the values of $\mathbf{u}$ at the vertices.

More precisely, the vertices of the discretization[3] of the domain are

$$\Lambda_{ij} = (\lambda_{ij}, \phi_{ij}),\ j = 0, \ldots, n,\ i = 0, \ldots, m,$$

where

$$\lambda_{ij} = -\pi + j\frac{2\pi}{n},\ \phi_{ij} = -\frac{\pi}{2} + i\frac{\pi}{m},\ j = 0, \ldots, n,\ i = 0, \ldots m,$$

and the corresponding values of $\mathbf{u}$ at Λ_{ij} are

$$\mathbf{u}_{ij} = \mathbf{u}(\lambda_{ij}, \phi_{ij}) = (u_{ij}, v_{ij}),\ j = 0, \ldots, n,\ i = 0, \ldots m.$$

Figure 2.6 illustrates what was just explained.

The image of each rectangle by the function $\mathbf{r}$ on the sphere is called *quad*.

In the next sections, we are going to formulate energy terms that depend on the values u_{ij} and v_{ij} and measure how much a panoramic image contains undesirable distortions.

[3]This discretization does not have to be the pixel discretization of the equirectangular image.

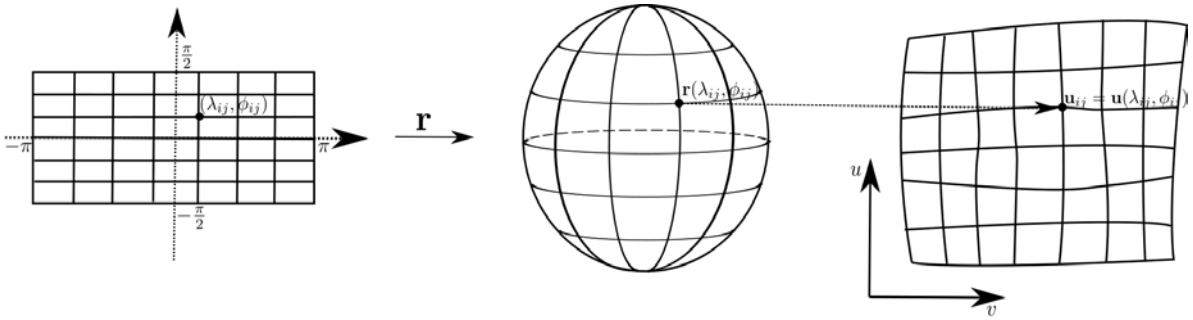

Figure 2.6: The discretization of the equirectangular domain induces a discretization of the viewing sphere. The vertices of this discretization of the sphere (or, equivalently, the vertices of the discretization of the equirectangular domain) are mapped to the image plane by the function **u**.

2.4 Conformality

This section is devoted to mathematically model the concept of preservation of shapes stated as a desirable property for wide-angle images in section 2.1.

The reader is assumed to have some notions of differential geometry of surfaces. Such notions can be found in [15], sections 2.1 to 2.5.

Here a point (λ, ϕ) is an interior point in the equirectangular domain, i.e., $\lambda \neq \pm\pi$ and $\phi \neq \pm\frac{\pi}{2}$. This assumption allows us to consider differential properties of the mapping **u** and turns **r** into an actual parametrization. Although now this parametrization does not cover the entire sphere (it excludes one meridian and the poles), we identify $\mathbf{r}((-\pi, \pi) \times (-\frac{\pi}{2}, \frac{\pi}{2}))$ as $\mathbb{S}^2$, for convenience.

2.4.1 Differential Geometry and the Cauchy-Riemann Equations

Definition 2.1 *A dipheomorfism $\varphi : S \to \overline{S}$ is a **conformal mapping** if for all $p \in S$ and for all $v_1, v_2 \in T_pS$ holds*

$$\langle d\varphi_p(v_1), d\varphi_p(v_2)\rangle = \Theta^2(p)\langle v_1, v_2\rangle,$$

where Θ^2 is a differentiable function on S that never vanishes.

The above definition says that $d\varphi_p$ preserves inner products (except for the Θ^2 factor). The following statement proves that conformal mappings preserve angles:

Statement 2.1 *Conformal mappings preserve angles.*

Proof: Let $\varphi : S \to \overline{S}$ be a conformal mapping. Let $\alpha : I \to S$ and $\beta : I \to S$ two curves in S that intersect in, say, $t = 0$. The angle θ between them at $t = 0$ is given by

$$\cos(\theta) = \frac{\langle \alpha'(0), \beta'(0)\rangle}{\| \alpha'(0) \| \| \beta'(0) \|}, \ 0 < \theta < \pi.$$

φ transform such curves in curves $\varphi \circ \alpha : I \to \overline{S}$, $\varphi \circ \beta : I \to \overline{S}$ that intersect at $t = 0$, forming an angle given by:

$$\cos(\overline{\theta}) = \frac{\langle d\varphi_{\alpha(0)}(\alpha'(0)), d\varphi_{\beta(0)}(\beta'(0))\rangle}{\parallel d\varphi_{\alpha(0)}(\alpha'(0)) \parallel \parallel d\varphi_{\beta(0)}(\beta'(0)) \parallel} = \frac{\Theta^2\langle \alpha'(0), \beta'(0)\rangle}{\Theta^2 \parallel \alpha'(0) \parallel \parallel \beta'(0) \parallel} = \cos(\theta).$$

■

The definition of conformal mappings turns up to be appropriate for modeling preservation of shapes: according to definition 2.1, locally, the objects can only be rotated and/or scaled in an equal manner along all directions. As we saw in statement 2.1, this also implies in the preservation of angles.

We bring the formal discussion into the panoramic image context by taking in the definition of conformality $S = \mathbb{S}^2$, $\overline{S} = \mathbb{R}^2$ and $\varphi = \mathbf{u}$.

Let $p \in (-\pi, \pi) \times \left(-\frac{\pi}{2}, \frac{\pi}{2}\right)$. The basis of $T_p\mathbb{S}^2$ associated to $\mathbf{r}$ (the longitude/latitude parametrization) is $\left\{\frac{\partial \mathbf{r}}{\partial \lambda}(p), \frac{\partial \mathbf{r}}{\partial \phi}(p)\right\}$, where

$$\frac{\partial \mathbf{r}}{\partial \lambda}(p) = \begin{pmatrix} -\sin(\lambda)\cos(\phi) \\ \cos(\lambda)\cos(\phi) \\ 0 \end{pmatrix} \text{ and } \frac{\partial \mathbf{r}}{\partial \phi}(p) \begin{pmatrix} -\cos(\lambda)\sin(\phi) \\ -\sin(\lambda)\sin(\phi) \\ \cos(\phi) \end{pmatrix}.$$

Assuming $\mathbf{u}$ to be a dipheomorfism $d\mathbf{u}_p : T_p\mathbb{S}^2 \to T_{\mathbf{u}(p)}\mathbb{R}^2 = \mathbb{R}^2$ has the following form[4]:

$$d\mathbf{u}_p(w) = \begin{pmatrix} \frac{\partial u}{\partial \lambda}(p) & \frac{\partial u}{\partial \phi}(p) \\ \frac{\partial v}{\partial \lambda}(p) & \frac{\partial v}{\partial \phi}(p) \end{pmatrix} w_{\left\{\frac{\partial \mathbf{r}}{\partial \lambda}(p), \frac{\partial \mathbf{r}}{\partial \phi}(p)\right\}},$$

where $w_{\left\{\frac{\partial \mathbf{r}}{\partial \lambda}(p), \frac{\partial \mathbf{r}}{\partial \phi}(p)\right\}}$ is a vector in $T_p\mathbb{S}^2$ written in the basis $\left\{\frac{\partial \mathbf{r}}{\partial \lambda}(p), \frac{\partial \mathbf{r}}{\partial \phi}(p)\right\}$.

It's clear that $\frac{\partial \mathbf{r}}{\partial \lambda}(p)$ and $\frac{\partial \mathbf{r}}{\partial \phi}(p)$ are orthogonal, but they are not unitary, since $\left\|\frac{\partial \mathbf{r}}{\partial \lambda}(p)\right\| = |\cos(\phi)| = \cos(\phi)$.

Thus we define the following orthonormal basis for $T_p\mathbb{S}^2$:

$$\widehat{\frac{\partial \mathbf{r}}{\partial \phi}(p)} = \frac{\partial \mathbf{r}}{\partial \phi}(p) = \begin{pmatrix} 0 \\ 1 \end{pmatrix}_{\left\{\frac{\partial \mathbf{r}}{\partial \lambda}(p), \frac{\partial \mathbf{r}}{\partial \phi}(p)\right\}}$$

and

$$\widehat{\frac{\partial \mathbf{r}}{\partial \lambda}(p)} = \frac{1}{\cos(\phi)}\frac{\partial \mathbf{r}}{\partial \lambda}(p) = \begin{pmatrix} \frac{1}{cos(\phi)} \\ 0 \end{pmatrix}_{\left\{\frac{\partial \mathbf{r}}{\partial \lambda}(p), \frac{\partial \mathbf{r}}{\partial \phi}(p)\right\}}.$$

Lemma 2.1 *$\boldsymbol{u} : \mathbb{S}^2 \to \mathbb{R}^2$ is conformal if and only if $d\boldsymbol{u}_p\left(\widehat{\frac{\partial \boldsymbol{r}}{\partial \phi}(p)}\right) = R_{\pm 90} \cdot d\boldsymbol{u}_p\left(\widehat{\frac{\partial \boldsymbol{r}}{\partial \lambda}(p)}\right)$, $\forall p \in (-\pi, \pi) \times \left(-\frac{\pi}{2}, \frac{\pi}{2}\right)$, where $R_{90} = \begin{pmatrix} 0 & -1 \\ 1 & 0 \end{pmatrix}$, $R_{-90} = \begin{pmatrix} 0 & 1 \\ -1 & 0 \end{pmatrix} = -R_{90}$ are 90 degree rotations.*

[4]Details in [15], pages 84 and 85.

Proof: ($\Leftarrow$) We want to prove that $\mathbf{u}$ is conformal. Let $p \in (-\pi,\pi)\times\left(-\frac{\pi}{2},\frac{\pi}{2}\right)$ and $v_1, v_2 \in T_p\mathbb{S}^2$. Suppose $v_1 = \alpha_1\widehat{\frac{\partial \mathbf{r}}{\partial\phi}(p)} + \beta_1\widehat{\frac{\partial \mathbf{r}}{\partial\lambda}(p)}$ and $v_2 = \alpha_2\widehat{\frac{\partial \mathbf{r}}{\partial\phi}(p)} + \beta_2\widehat{\frac{\partial \mathbf{r}}{\partial\lambda}(p)}$. It's clear that

$$\langle v_1, v_2\rangle = \alpha_1\alpha_2 + \beta_1\beta_2,$$

since $\widehat{\frac{\partial \mathbf{r}}{\partial\phi}(p)}$ and $\widehat{\frac{\partial \mathbf{r}}{\partial\lambda}(p)}$ are orthonormal. Now consider

$$\begin{aligned}\langle d\mathbf{u}_p(v_1), d\mathbf{u}_p(v_2)\rangle &= \langle \alpha_1 d\mathbf{u}_p\left(\widehat{\tfrac{\partial \mathbf{r}}{\partial\phi}(p)}\right) + \beta_1 d\mathbf{u}_p\left(\widehat{\tfrac{\partial \mathbf{r}}{\partial\lambda}(p)}\right), \alpha_2 d\mathbf{u}_p\left(\widehat{\tfrac{\partial \mathbf{r}}{\partial\phi}(p)}\right) + \beta_2 d\mathbf{u}_p\left(\widehat{\tfrac{\partial \mathbf{r}}{\partial\lambda}(p)}\right)\rangle \\ &= \alpha_1\alpha_2\left\|d\mathbf{u}_p\left(\widehat{\tfrac{\partial \mathbf{r}}{\partial\phi}(p)}\right)\right\|^2 + \alpha_1\beta_2\langle d\mathbf{u}_p\left(\widehat{\tfrac{\partial \mathbf{r}}{\partial\phi}(p)}\right), d\mathbf{u}_p\left(\widehat{\tfrac{\partial \mathbf{r}}{\partial\lambda}(p)}\right)\rangle + \\ &\quad +\beta_1\alpha_2\langle d\mathbf{u}_p\left(\widehat{\tfrac{\partial \mathbf{r}}{\partial\lambda}(p)}\right), d\mathbf{u}_p\left(\widehat{\tfrac{\partial \mathbf{r}}{\partial\phi}(p)}\right)\rangle + \beta_1\beta_2\left\|d\mathbf{u}_p\left(\widehat{\tfrac{\partial \mathbf{r}}{\partial\lambda}(p)}\right)\right\|^2\end{aligned}.$$

Applying the hypothesis, we have

$$\langle d\mathbf{u}_p\left(\widehat{\tfrac{\partial \mathbf{r}}{\partial\phi}(p)}\right), d\mathbf{u}_p\left(\widehat{\tfrac{\partial \mathbf{r}}{\partial\lambda}(p)}\right)\rangle = \langle d\mathbf{u}_p\left(\widehat{\tfrac{\partial \mathbf{r}}{\partial\lambda}(p)}\right), d\mathbf{u}_p\left(\widehat{\tfrac{\partial \mathbf{r}}{\partial\phi}(p)}\right)\rangle = 0$$

and

$$\left\|d\mathbf{u}_p\left(\widehat{\tfrac{\partial \mathbf{r}}{\partial\phi}(p)}\right)\right\| = \left\|d\mathbf{u}_p\left(\widehat{\tfrac{\partial \mathbf{r}}{\partial\lambda}(p)}\right)\right\|$$

and we obtain

$$\langle d\mathbf{u}_p(v_1), d\mathbf{u}_p(v_2)\rangle = \left\|d\mathbf{u}_p\left(\widehat{\tfrac{\partial \mathbf{r}}{\partial\phi}(p)}\right)\right\|^2(\alpha_1\alpha_2+\beta_1\beta_2) = \left\|d\mathbf{u}_p\left(\widehat{\tfrac{\partial \mathbf{r}}{\partial\phi}(p)}\right)\right\|^2\langle v_1, v_2\rangle.$$

Taking $\Theta(p) = \left\|d\mathbf{u}_p\left(\widehat{\frac{\partial \mathbf{r}}{\partial\phi}(p)}\right)\right\|$ in the definition of conformality, we conclude that $\mathbf{u}$ is conformal.

($\Rightarrow$) Now suppose that $\mathbf{u}$ is conformal, i.e.,

$$\langle d\mathbf{u}_p(v_1), d\mathbf{u}_p(v_2)\rangle = \Theta(p)^2\langle v_1, v_2\rangle,\ \forall v_1, v_2 \in T_p\mathbb{S}^2.$$

• Taking $v_1 = \widehat{\frac{\partial \mathbf{r}}{\partial\phi}(p)}$ and $v_2 = \widehat{\frac{\partial \mathbf{r}}{\partial\lambda}(p)}$ leads to $\langle d\mathbf{u}_p\left(\widehat{\frac{\partial \mathbf{r}}{\partial\phi}(p)}\right), d\mathbf{u}_p\left(\widehat{\frac{\partial \mathbf{r}}{\partial\lambda}(p)}\right)\rangle = 0$, i.e., $d\mathbf{u}_p\left(\widehat{\frac{\partial \mathbf{r}}{\partial\phi}(p)}\right)$ and $d\mathbf{u}_p\left(\widehat{\frac{\partial \mathbf{r}}{\partial\lambda}(p)}\right)$ are orthogonal.

• Taking $v_1 = v_2 = \widehat{\frac{\partial \mathbf{r}}{\partial\phi}(p)}$ we obtain $\left\|d\mathbf{u}_p\left(\widehat{\frac{\partial \mathbf{r}}{\partial\phi}(p)}\right)\right\| = |\Theta(p)|$. Taking $v_1 = v_2 = \widehat{\frac{\partial \mathbf{r}}{\partial\lambda}(p)}$ leads to $\left\|d\mathbf{u}_p\left(\widehat{\frac{\partial \mathbf{r}}{\partial\lambda}(p)}\right)\right\| = |\Theta(p)|$. Thus $\left\|d\mathbf{u}_p\left(\widehat{\frac{\partial \mathbf{r}}{\partial\phi}(p)}\right)\right\| = \left\|d\mathbf{u}_p\left(\widehat{\frac{\partial \mathbf{r}}{\partial\lambda}(p)}\right)\right\|$.

The two above considerations, $d\mathbf{u}_p\left(\widehat{\frac{\partial \mathbf{r}}{\partial\phi}(p)}\right)$ and $d\mathbf{u}_p\left(\widehat{\frac{\partial \mathbf{r}}{\partial\lambda}(p)}\right)$ are orthogonal and have the same length in $\mathbb{R}^2$, allows only two possibilities: $d\mathbf{u}_p\left(\widehat{\frac{\partial \mathbf{r}}{\partial\phi}(p)}\right) = R_{90}\cdot d\mathbf{u}_p\left(\widehat{\frac{\partial \mathbf{r}}{\partial\lambda}(p)}\right)$ or $d\mathbf{u}_p\left(\widehat{\frac{\partial \mathbf{r}}{\partial\phi}(p)}\right) = R_{-90}\cdot d\mathbf{u}_p\left(\widehat{\frac{\partial \mathbf{r}}{\partial\lambda}(p)}\right)$.

■

We call

$$\mathbf{h} = d\mathbf{u}_p\left(\widehat{\frac{\partial \mathbf{r}}{\partial \phi}(p)}\right) = \begin{pmatrix} \frac{\partial u}{\partial \lambda}(p) & \frac{\partial u}{\partial \phi}(p) \\ \frac{\partial v}{\partial \lambda}(p) & \frac{\partial v}{\partial \phi}(p) \end{pmatrix} \begin{pmatrix} 0 \\ 1 \end{pmatrix} = \begin{pmatrix} \frac{\partial u}{\partial \phi}(p) \\ \frac{\partial v}{\partial \phi}(p) \end{pmatrix}$$

the *differential north vector* and

$$\mathbf{k} = d\mathbf{u}_p\left(\widehat{\frac{\partial \mathbf{r}}{\partial \lambda}(p)}\right) = \begin{pmatrix} \frac{\partial u}{\partial \lambda}(p) & \frac{\partial u}{\partial \phi}(p) \\ \frac{\partial v}{\partial \lambda}(p) & \frac{\partial v}{\partial \phi}(p) \end{pmatrix} \begin{pmatrix} \frac{1}{\cos(\phi)} \\ 0 \end{pmatrix} = \frac{1}{\cos(\phi)} \begin{pmatrix} \frac{\partial u}{\partial \lambda}(p) \\ \frac{\partial v}{\partial \lambda}(p) \end{pmatrix}$$

the *differential east vector*.

The lemma tells us that $\mathbf{u}$ conformal is equivalent to $\mathbf{h} = R_{90}\mathbf{k}$ or $\mathbf{h} = R_{-90}\mathbf{k}$. Both possibilities are shown in figure 2.7.

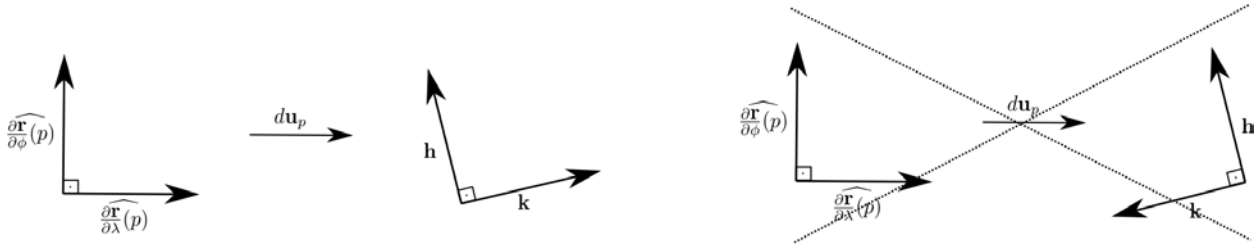

Figure 2.7: We exclude the second possibility above.

We ask $\mathbf{u}$ to preserve the orientation of the orthonormal basis of the tangent plane, i.e., we forbid $\mathbf{h} = R_{-90}\mathbf{k}$.

This choice avoids a *mirroring* effect that could appear on the final result.

With these new considerations we restate the lemma:

Theorem 2.1 *(Cauchy-Riemann Equations) Let* $p = (\lambda, \phi) \in (-\pi, \pi) \times \left(-\frac{\pi}{2}, \frac{\pi}{2}\right)$. $\boldsymbol{u} : \mathbb{S}^2 \to \mathbb{R}^2$ *is a conformal mapping that preserves the orientation of the orthonormal basis of* $T_p\mathbb{S}^2$ *if and only if*

$$\frac{\partial u}{\partial \phi}(p) = -\frac{1}{\cos(\phi)}\frac{\partial v}{\partial \lambda}(p) \text{ and } \frac{\partial v}{\partial \phi}(p) = \frac{1}{\cos(\phi)}\frac{\partial u}{\partial \lambda}(p).$$

Proof: $\mathbf{u}$ conformal mapping that preserves orientation $\Leftrightarrow \mathbf{h} = R_{90}\mathbf{k} \Leftrightarrow \begin{pmatrix} \frac{\partial u}{\partial \phi}(p) \\ \frac{\partial v}{\partial \phi}(p) \end{pmatrix} =$

$$= \begin{pmatrix} 0 & -1 \\ 1 & 0 \end{pmatrix} \begin{pmatrix} \frac{1}{\cos(\phi)}\frac{\partial u}{\partial \lambda}(p) \\ \frac{1}{\cos(\phi)}\frac{\partial v}{\partial \lambda}(p) \end{pmatrix} \Leftrightarrow \begin{cases} \frac{\partial u}{\partial \phi}(p) &= -\frac{1}{\cos(\phi)}\frac{\partial v}{\partial \lambda}(p) \\ \frac{\partial v}{\partial \phi}(p) &= \frac{1}{\cos(\phi)}\frac{\partial u}{\partial \lambda}(p) \end{cases}.$$

■

Despite of being a little abuse of nomenclature, from now on we consider the fact of $\mathbf{u} : \mathbb{S}^2 \to \mathbb{R}^2$ being conformal equivalent to $\mathbf{u}$ satisfying the Cauchy-Riemann Equations. The C-R equations are an analytical and practical way of checking conformality.

2.4.2 Examples

This section illustrates the theory that we just developed with two mappings **u** already discussed in chapter 1: there we just used intuition and perception to argument that Mercator (section 1.3.3) and Stereographic (section 1.3.2) projections are conformal. Here we argument it analytically.

The Mercator projection is a cylindrical projection designed to maintain conformality. The imposition $u = \lambda$ makes it cylindrical because u is proportional to λ.

To impose conformality, we use the C-R equations and determine the expression for the v coordinate: from the second equation

$$\frac{\partial v}{\partial \phi} = \frac{1}{\cos(\phi)} \cdot \underbrace{\frac{\partial u}{\partial \lambda}}_{1} = \frac{1}{cos(\phi)}.$$

From basic calculus, we know that one possible solution for the above differential equations is

$$v = \log(\sec(\phi) + \tan(\phi)).$$

Such v also satisfies the first C-R equation:

$$\frac{\partial u}{\partial \phi} = 0 = -\frac{1}{\cos(\phi)} \cdot 0 = -\frac{1}{\cos(\phi)} \frac{\partial v}{\partial \lambda}$$

Thus the projection $(\lambda, \phi) \rightarrow (u = \lambda, v = \log(\sec(\phi) + \tan(\phi)))$ is cylindrical and conformal. We show in fugure 2.8 an example of wide-angle image generated by the Mecator projection, where we can see that, in fact, shapes of objects are well-preserved:

Figure 2.8: Example of Mercator projection.

Now we consider the stereographic projection:

Statement 2.2 *The stereographic projection is conformal.*

Proof: As we saw in section 1.3.2, the coordinates of the stereographic projection are

$$u = \frac{2\sin(\lambda)\cos(\phi)}{\cos(\lambda)\cos(\phi)+1} \text{ and } v = \frac{2\sin(\phi)}{\cos(\lambda)\cos(\phi)+1}.$$

It's enough to check the two C-R equations in order to prove conformality, but here we check only the first one, since the second is analogous:

$$\begin{aligned}
\bullet\ \frac{\partial u}{\partial \phi} &= \frac{[\frac{\partial}{\partial\phi}(2\sin\lambda\cos\phi)][\cos\lambda\cos\phi+1]-[\frac{\partial}{\partial\phi}(\cos\lambda\cos\phi+1)][2\sin\lambda\cos\phi]}{(\cos\lambda\cos\phi+1)^2} \\
&= \frac{[-2\sin\lambda\sin\phi][\cos\lambda\cos\phi+1]-[-\cos\lambda\sin\phi][2\sin\lambda\cos\phi]}{(\cos\lambda\cos\phi+1)^2} \\
&= \frac{-2\sin\lambda\cos\lambda\sin\phi\cos\phi-2\sin\lambda\sin\phi+2\sin\lambda\cos\lambda\sin\phi\cos\phi}{(\cos\lambda\cos\phi+1)^2} \\
&= \frac{-2\sin\lambda\sin\phi}{(\cos\lambda\cos\phi+1)^2}.
\end{aligned}$$

$$\begin{aligned}
\bullet\ \frac{\partial v}{\partial \lambda} &= \frac{[\frac{\partial}{\partial\lambda}(2\sin\phi)][\cos\lambda\cos\phi+1]-[\frac{\partial}{\partial\lambda}(\cos\lambda\cos\phi+1)][2\sin\phi]}{(\cos\lambda\cos\phi+1)^2} \\
&= \frac{-[-\sin\lambda\cos\phi][2\sin\phi]}{(\cos\lambda\cos\phi+1)^2} = \frac{2\sin\lambda\sin\phi\cos\phi}{(\cos\lambda\cos\phi+1)^2}.
\end{aligned}$$

Thus $\frac{\partial u}{\partial\phi}(\lambda,\phi) = -\frac{1}{\cos\phi}\frac{\partial v}{\partial\lambda}(\lambda,\phi)$, $\forall(\lambda,\phi)\in(-\pi,\pi)\times\left(-\frac{\pi}{2},\frac{\pi}{2}\right)$.

■

We show in figure 2.9 an example of panoramic image produced by the stereographic projection, where the shapes of the objects are well preserved:

Figure 2.9: 285 degree longitude/180 degree latitude.

2.4.3 Energy Term

We now focus on measuring how conformal a mapping from the discretized viewing sphere (section 2.3) to the plane is.

For this task, we use the C-R equations obtained in section 2.4.1 among with a standard numerical technique for discretizing PDEs, named *finite differences*. We approximate the partial derivatives at the vertices of the discretized viewing sphere in the following way:

$$\frac{\partial u}{\partial \phi}(\lambda_{ij}, \phi_{ij}) \approx \left(\frac{u_{i+1,j} - u_{ij}}{\Delta\phi}\right), \quad \frac{\partial v}{\partial \lambda}(\lambda_{ij}, \phi_{ij}) \approx \left(\frac{v_{i,j+1} - v_{ij}}{\Delta\lambda}\right),$$
$$\frac{\partial v}{\partial \phi}(\lambda_{ij}, \phi_{ij}) \approx \left(\frac{v_{i+1,j} - v_{ij}}{\Delta\phi}\right), \quad \frac{\partial u}{\partial \lambda}(\lambda_{ij}, \phi_{ij}) \approx \left(\frac{u_{i,j+1} - u_{ij}}{\Delta\lambda}\right),$$

where $\Delta\phi = \dfrac{\pi}{m}$ and $\Delta\lambda = \dfrac{2\pi}{n}$.

Replacing the derivatives by their approximations in both C-R equations,

$$\frac{\partial u}{\partial \phi} = -\frac{1}{\cos\phi}\frac{\partial v}{\partial \lambda}, \quad \frac{\partial v}{\partial \phi} = \frac{1}{\cos\phi}\frac{\partial u}{\partial \lambda},$$

we obtain

$$\left(\frac{u_{i+1,j} - u_{ij}}{\Delta\phi}\right) = -\frac{1}{\cos(\phi_{ij})}\left(\frac{v_{i,j+1} - v_{ij}}{\Delta\lambda}\right), \ j = 0, \ldots, n-1, \ i = 0, \ldots, m-1$$

and

$$\left(\frac{v_{i+1,j} - v_{ij}}{\Delta\phi}\right) = \frac{1}{\cos(\phi_{ij})}\left(\frac{u_{i,j+1} - u_{ij}}{\Delta\lambda}\right), \ j = 0, \ldots, n-1, \ i = 0, \ldots, m-1.$$

Thus a discretized mapping should satisfy the following equations:

$$\frac{u_{i+1,j} - u_{ij}}{\Delta\phi} + \frac{1}{\cos\phi_{ij}}\frac{v_{i,j+1} - v_{ij}}{\Delta\lambda} = 0$$

and

$$\frac{1}{\cos\phi_{ij}}\frac{u_{i,j+1} - u_{ij}}{\Delta\lambda} - \frac{v_{i+1,j} - v_{ij}}{\Delta\phi} = 0.$$

If we take the left sides of both equations to measure the deviation of conformality, we will obtain similar values of deviations for quads with very different areas on the viewing sphere. This would cause an effect of biasing conformality in regions of the sphere with high quad densities and trying to minimize these conformality deviations would favor such regions.

We fix this problem by multiplying both equations by a fixed multiple of the area of each quad on the sphere.

The definition of area of a part of a surface can be found in ([15], page 98).

In our case, we want to know the area of $\mathbf{r}([\lambda_{ij}, \lambda_{i,j+1}] \times [\phi_{ij}, \phi_{i+1,j}]) = \mathbf{r}([\lambda_{ij}, \lambda_{ij} + \Delta\lambda] \times [\phi_{ij}, \phi_{ij} + \Delta\phi])$ on the viewing sphere, which is given by the following:

$$Area_{ij} = \int_{\phi_{ij}}^{\phi_{ij}+\Delta\phi} \int_{\lambda_{ij}}^{\lambda_{ij}+\Delta\lambda} \left\| \frac{\partial \mathbf{r}}{\partial \lambda}(\lambda, \phi) \times \frac{\partial \mathbf{r}}{\partial \phi}(\lambda, \phi) \right\| d\lambda d\phi.$$

Straightforward calculations give us:

$$\frac{\partial \mathbf{r}}{\partial \lambda} \times \frac{\partial \mathbf{r}}{\partial \phi} = \begin{pmatrix} \cos\lambda \cos^2\phi \\ \sin\lambda \cos^2\phi \\ \sin\phi \cos\phi \end{pmatrix}$$

and

$$\left\| \frac{\partial \mathbf{r}}{\partial \lambda} \times \frac{\partial \mathbf{r}}{\partial \phi} \right\| = \cos\phi.$$

Thus

$$\begin{aligned} Area_{ij} &= \int_{\phi_{ij}}^{\phi_{ij}+\Delta\phi} \int_{\lambda_{ij}}^{\lambda_{ij}+\Delta\lambda} \cos\phi d\lambda d\phi = \Delta\lambda \int_{\phi_{ij}}^{\phi_{ij}+\Delta\phi} \cos\phi d\phi = \\ &= \Delta\lambda\Delta\phi \cos\tilde{\phi} \approx \Delta\lambda\Delta\phi \cos\phi_{ij}, \end{aligned}$$

where $\tilde{\phi}$ is some value in $[\phi_{ij}, \phi_{ij} + \Delta\phi]$.

Since $\Delta\lambda\Delta\phi$ is constant, we conclude that $Area_{ij}$ is proportional to $\cos(\phi_{ij})$, and the discretized equations become

$$\frac{v_{i,j+1} - vij}{\Delta\lambda} + \cos(\phi_{ij}) \frac{u_{i+1,j} - u_{ij}}{\Delta\phi} = 0,$$

$$\frac{u_{i,j+1} - uij}{\Delta\lambda} - \cos(\phi_{ij}) \frac{v_{i+1,j} - v_{ij}}{\Delta\phi} = 0.$$

We define the conformality energy of $\mathbf{u}$ to be a weighted sum of the quadratic errors of both equations:

$$\begin{aligned} E_c &= \sum_{i=0}^{m-1} \sum_{j=0}^{n-1} w_{ij}^2 \left(\frac{v_{i,j+1} - v_{ij}}{\Delta\lambda} + \cos\phi_{ij} \frac{u_{i+1,j} - u_{ij}}{\Delta\phi} \right)^2 + \\ &+ \sum_{i=0}^{m-1} \sum_{j=0}^{n-1} w_{ij}^2 \left(\frac{u_{i,j+1} - u_{ij}}{\Delta\lambda} - \cos\phi_{ij} \frac{v_{i+1,j} - v_{ij}}{\Delta\phi} \right)^2. \end{aligned}$$

w_{ij} are spatially varying weights that depend on the content of the image and will be defined in section 2.7.

The definition of E_c is necessary because we need a way of measuring how much conformal a discretized mapping is. In order to produce the final result, we will join this energy to other ones and the task of looking for a conformal mapping will be replaced by looking for a mapping that minimizes a weighted sum of these energies.

E_c can be rewritten as $E_c = \| C\mathbf{x} \|^2$, where C is a matrix and $\mathbf{x}$ is a vector, since E_c is a sum of squares of linear terms.

Let $\mathbf{x} \in \mathbb{R}^{2(m+1)(n+1)}$, where

$$\mathbf{x}_{2(j+i(n+1))} = u_{ij} \text{ and } \mathbf{x}_{2(j+i(n+1))+1} = v_{ij}, \quad i = 0, \ldots, m, \ j = 0, \ldots, n.$$

Each entry of $C\mathbf{x}$ must correspond to the term that is in each double summation of E_c. So each line of C must correspond to a double summation and C must have $2mn$ lines.

Let $C \in \mathbb{R}^{2mn \times 2(m+1)(n+1)}$. The equality $E_c = \| C\mathbf{x} \|^2$ is achieved by defining:

$$C_{2(j+in),2((j+1)+i(n+1))+1} = \frac{w_{ij}}{\Delta\lambda}, \quad C_{2(j+in),2(j+i(n+1))+1} = -\frac{w_{ij}}{\Delta\lambda},$$
$$C_{2(j+in),2(j+(i+1)(n+1))} = \frac{w_{ij}\cos\phi_{ij}}{\Delta\phi}, \quad C_{2(j+in),2(j+i(n+1))} = -\frac{w_{ij}\cos\phi_{ij}}{\Delta\phi},$$
$$C_{2(j+in)+1,2((j+1)+i(n+1))} = \frac{w_{ij}}{\Delta\lambda}, \quad C_{2(j+in)+1,2(j+i(n+1))} = -\frac{w_{ij}}{\Delta\lambda},$$
$$C_{2(j+in)+1,2(j+(i+1)(n+1))+1} = -\frac{w_{ij}\cos\phi_{ij}}{\Delta\phi}, \quad C_{2(j+in)+1,2(j+i(n+1))+1} = \frac{w_{ij}\cos\phi_{ij}}{\Delta\phi},$$

$i = 0, \ldots, m-1$, $j = 0, \ldots, n-1$. The other entries of C are defined as 0.

We call C the *conformality matrix* and observe that it is sparse: only 4 nonzero entries per row.

We do not discuss the minimization of $E_c = \| C\mathbf{x} \|^2$ here, since E_c will be minimized with other energies in section 2.8. But in figure 2.10 we show a panoramic image that one obtains when minimizes such energy alone. As we can see, the object shapes are well preserved but lines that should be straight are too curved. We deal with this problem in next section.

Figure 2.10: A panoramic image obtained by minimizing E_c. Observe that it is the stereographic projection, which we already know to be conformal. It will be more clear in section 2.8.3 why between all possible conformal mappings, the stereographic one is the result for minimizing E_c using the method proposed in this section.

2.5 Straight Lines

In this section, we approach another important aspect in panoramic images mentioned on section 2.1: the preservation of straight lines.

In contrast to other energies, we do not model straightness of lines in a continuous manner and then discretize it. We directly use the discretization of the sphere to formulate

straight line energies.

Here we use the information given by the user (section 2.2) and constrain the curves marked by her to be lines in the final result. Figure 2.11 shows another example of a marked equirectangular image.

Figure 2.11: An image produced by the interface presented in section 2.2.

We consider three sets of lines[5]:

$$L = \{\text{All marked lines}\},$$

$$L_f = \{\text{Lines with fixed orientation}\},$$

$$L \backslash L_f = \{\text{Lines with general orientation}\}.$$

Thus L is the set of green, red and blue lines, L_f is the set of red and blue lines and $L \backslash L_f$ is the set of green lines.

Let $l \in L$. In general, the vertices Λ_{ij} of the discretization of the equirectangular domain do not belong to l.

We thus define a virtual vertex for each quad on the sphere that is intersected by l in the following way: Let $q_{ij} \in V_l = \{\text{Quads intersected by } l \text{ except the first and the last}\}$. Let $\mathbf{r}(\Lambda_0), \mathbf{r}(\Lambda_1)$ be the endpoints of $q_{ij} \cap l$ (see figure 2.12).

We define the virtual vertex P as:

$$P = \frac{\frac{1}{2}\mathbf{r}(\Lambda_0) + \frac{1}{2}\mathbf{r}(\Lambda_1)}{\| \frac{1}{2}\mathbf{r}(\Lambda_0) + \frac{1}{2}\mathbf{r}(\Lambda_1) \|},$$

which is approximately the midpoint of $q_{ij} \cap l$. We use the midpoints because they are evenly spaced along l.

For the first and last quads that l intersects, say q_{start} and q_{end}, the virtual vertices are the endpoints of l themselves, regardless of their positions (see figure 2.13).

[5]Here *line* stands for marked curves on the equirectangular domain.

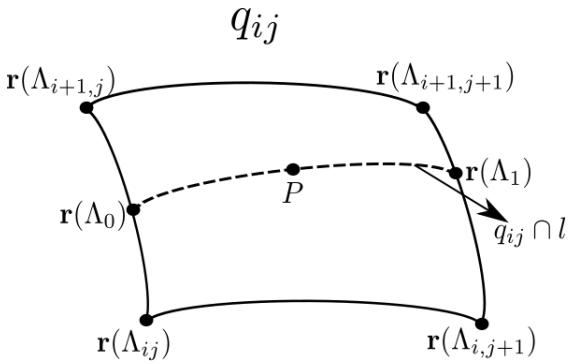

Figure 2.12: Intersection of q_{ij} and l and the virtual vertex P.

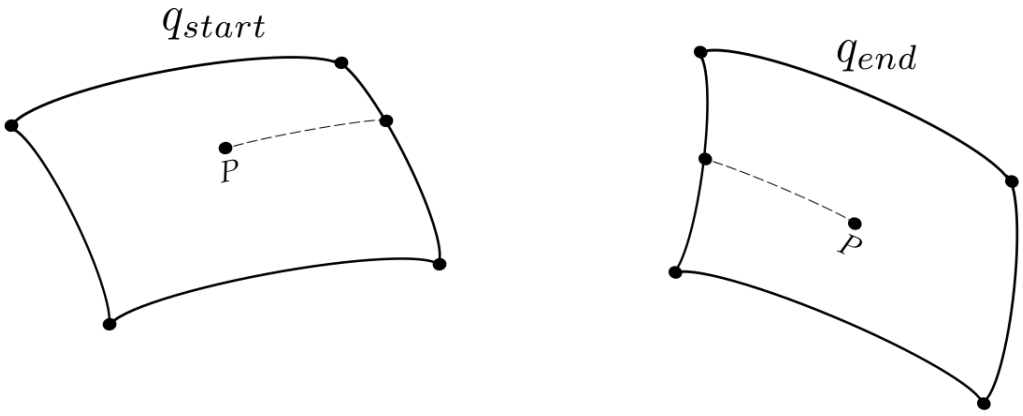

Figure 2.13: Virtual vertices for start and end quads.

Now, for each virtual vertex, we define an *output* virtual vertex in the following way: let $A = \mathbf{r}(\Lambda_{ij})$, $B = \mathbf{r}(\Lambda_{i,j+1})$, $C = \mathbf{r}(\Lambda_{i+1,j})$, $D = \mathbf{r}(\Lambda_{i+1,j+1})$. We project these four points orthogonally on the plane tangent to the sphere passing through P and obtain $\tilde{A}$, $\tilde{B}$, $\tilde{C}$, $\tilde{D}$. The result of this projection is shown in figure 2.14.

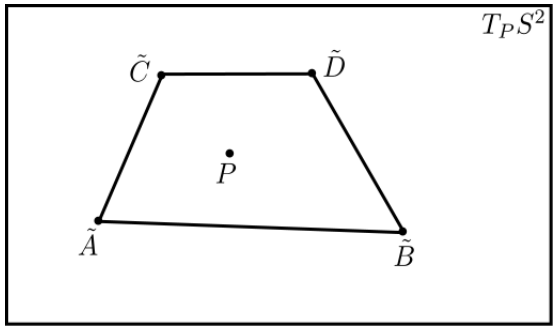

Figure 2.14: Projection of q_{ij} on $T_P\mathbb{S}^2$ and corresponding vertices.

We then obtain the bilinear coefficients a, b, c, d that express P as convex combination of $\tilde{A}$, $\tilde{B}$, $\tilde{C}$, $\tilde{D}$: $P = a\tilde{A} + b\tilde{B} + c\tilde{C} + d\tilde{D}$. The details of this process are given in section 2.5.2 (Inverting bilinear interpolation).

We use these coefficients to define the *output* virtual vertex

$$\mathbf{u}^l_{ij} = a\mathbf{u}_{ij} + b\mathbf{u}_{i,j+1} + c\mathbf{u}_{i+1,j} + d\mathbf{u}_{i+1,j+1},\ q_{ij} \in V_l.$$

The same is done to define $\mathbf{u}^l_{start}$ and $\mathbf{u}^l_{end}$, the virtual vertices corresponding to the endpoints of l.

We define our straight line energies as a function of the position of the output virtual vertices, that are linear combinations of actual output vertices $\mathbf{u}_{ij}$. Thus, in the end, the energies will depend only on the $\mathbf{u}_{ij}$'s.

In order to have all $\mathbf{u}^l_{ij}$'s collinear, we should have the distance from each $\mathbf{u}^l_{ij}$ to the line connecting $\mathbf{u}^l_{start}$ to $\mathbf{u}^l_{end}$ to be zero, $\forall q_{ij} \in V_l$ (see figure 2.15).

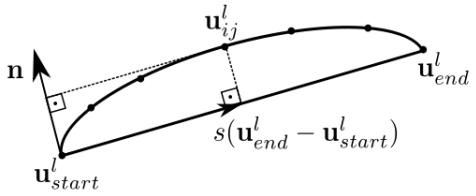

Figure 2.15: The distance should be zero.

One way of expressing this distance is as the coefficient of the orthogonal projection of $\mathbf{u}^l_{ij} - \mathbf{u}^l_{start}$ on the normal direction to $\mathbf{u}^l_{end} - \mathbf{u}^l_{start}$, which is given by

$$(\mathbf{u}^l_{ij} - \mathbf{u}^l_{start})^T \mathbf{n}(\mathbf{u}^l_{start}, \mathbf{u}^l_{end}),$$

where

$$\mathbf{n}(\mathbf{u}^l_{start}, \mathbf{u}^l_{end}) = R_{90} \frac{\mathbf{u}^l_{end} - \mathbf{u}^l_{start}}{\| \mathbf{u}^l_{end} - \mathbf{u}^l_{start} \|}.$$

Using such distance to measure how the $\mathbf{u}^l_{ij}$'s are not collinear leads to the following energy for line l:

$$E_l = \sum_{q_{ij} \in V_l} \left((\mathbf{u}^l_{ij} - \mathbf{u}^l_{start})^T \mathbf{n}(\mathbf{u}^l_{start}, \mathbf{u}^l_{end}) \right)^2.$$

This expression is not convenient because it involves cross products of variables. As a consequence, E_l becomes a sum of nonlinear squares. We want it to be a sum of linear squares, since the other energies have such form.

We now turn to an alternative way of expressing the distance from $\mathbf{u}^l_{ij}$ to the line connecting $\mathbf{u}^l_{start}$ to $\mathbf{u}^l_{end}$: as the norm of the difference between $\mathbf{u}^l_{ij} - \mathbf{u}^l_{start}$ and its orthogonal projection on the line connecting $\mathbf{u}^l_{start} - \mathbf{u}^l_{end}$:

$$\| (\mathbf{u}^l_{ij} - \mathbf{u}^l_{start}) - s(\mathbf{u}^l_{ij}, \mathbf{u}^l_{start}, \mathbf{u}^l_{end})(\mathbf{u}^l_{end} - \mathbf{u}^l_{start}) \|,$$

where

$$s(\mathbf{u}^l_{ij}, \mathbf{u}^l_{start}, \mathbf{u}^l_{end}) = \frac{(\mathbf{u}^l_{ij} - \mathbf{u}^l_{start})^T (\mathbf{u}^l_{end} - \mathbf{u}^l_{start})}{\| \mathbf{u}^l_{end} - \mathbf{u}^l_{start} \|}.$$

E_l can be rewritten in the following form:

$$E_l = \sum_{q_{ij} \in V_l} \| (\mathbf{u}^l_{ij} - \mathbf{u}^l_{start}) - s(\mathbf{u}^l_{ij}, \mathbf{u}^l_{start}, \mathbf{u}^l_{end})(\mathbf{u}^l_{end} - \mathbf{u}^l_{start}) \|^2.$$

It turns out that this way of expressing E_l is also a sum of nonlinear squares.

We simplify the two expressions for E_l by fixing the normal vector $\mathbf{n}$ on the first expression, which leads to

$$E_{lo} = \sum_{q_{ij} \in V_l} \left((\mathbf{u}_{ij}^l - \mathbf{u}_{start}^l)^T \mathbf{n} \right)^2 ,$$

and by fixing the projection s_{ij} on the second expression, which leads to

$$E_{ld} = \sum_{q_{ij} \in V_l} \| \, (\mathbf{u}_{ij}^l - \mathbf{u}_{start}^l) - s_{ij}(\mathbf{u}_{end}^l - \mathbf{u}_{start}^l) \, \|^2 .$$

Both these energies are now sums of linear squares.

They have a geometric interpretation: E_{lo} allows points to slide freely along the line, while fixing line's orientation (defined by the normal vector) and E_{ld} allows the line to change its direction while fixing the relative positions of the points, defined by the s_{ij}'s.

If $l \in L_f$, i.e., l has a specified orientation, the vector $\mathbf{n}$ is known and fixed, so we just minimize E_{lo} in this case.

If $l \in L \backslash L_f$, we use both E_{lo} and E_{ld} in an interactive minimization. The steps are described below:

• Initialize each s_{ij} using the arc length between $\mathbf{r}(\Lambda_{ij})$ and $\mathbf{r}(\Lambda_{start})$ on the viewing sphere;
• Minimize E_{ld} to obtain new values for $\mathbf{u}_{ij}$ (and thus obtain new values for $\mathbf{u}_{ij}^l$, $\mathbf{u}_{start}$ and $\mathbf{u}_{end}$);
• From the new values $\mathbf{u}_{start}$ and $\mathbf{u}_{end}$, calculate the normal vector

$$\mathbf{n} = R_{90} \frac{\mathbf{u}_{end}^l - \mathbf{u}_{start}^l}{\| \, \mathbf{u}_{end}^l - \mathbf{u}_{start}^l \, \|};$$

• Minimize E_{lo} to obtain new values for $\mathbf{u}_{ij}$ (and thus obtain new values for $\mathbf{u}_{ij}^l$, $\mathbf{u}_{start}$ and $\mathbf{u}_{end}$);
• From these new values, calculate

$$s_{ij} = \frac{(\mathbf{u}_{ij}^l - \mathbf{u}_{start}^l)^T (\mathbf{u}_{end}^l - \mathbf{u}_{start}^l)^2}{\| \, \mathbf{u}_{end}^l - \mathbf{u}_{start}^l \, \|} , \ \forall q_{ij} \in V_l;$$

• Return to the 2nd step and repeat the process until convergence[6].

2.5.1 Energy terms

In the last section, we analyzed one single line and obtained straight line energies associated to it.

[6]Although we do not have a theoretical proof of convergence, in practice the results always converged visually after repeating the steps above 4 times at most.

We now turn such energies into a matrix form and develop the straight line energies for the whole mapping $\mathbf{u}$.

We start by considering $l \in L_f$, which is the simplest case. Let $\mathbf{n} = (n_1, n_2)^T$ the normal vector ($\mathbf{n} = (1,0)^T$ for vertical lines and $\mathbf{n} = (0,1)^T$ for horizontal ones).

Developing the energy term we obtain:

$$\begin{aligned}
E_{lo}\big|_l &= \sum_{q_{ij}\in V_l} \left((\mathbf{u}^l_{ij} - \mathbf{u}^l_{start})^T \begin{pmatrix} n_1 \\ n_2 \end{pmatrix} \right)^2 \\
&= \sum_{q_{ij}\in V_l} \Bigg((a_{ij}\mathbf{u}_{ij} + b_{i,j+1}\mathbf{u}_{i,j+1} + c_{i+1,j}\mathbf{u}_{i+1,j} + d_{i+1,j+1}\mathbf{u}_{i+1,j+1} - a_{start}\mathbf{u}_{i_{start},j_{start}} - \\
&\quad - b_{start}\mathbf{u}_{i_{start},j_{start}+1} - c_{start}\mathbf{u}_{i_{start}+1,j_{start}} - d_{start}\mathbf{u}_{i_{start}+1,j_{start}+1})^T \begin{pmatrix} n_1 \\ n_2 \end{pmatrix} \Bigg)^2 \\
&= \sum_{q_{ij}\in V_l} (n_1 a_{ij}u_{ij} + n_1 b_{i,j+1}u_{i,j+1} + n_1 c_{i+1,j}u_{i+1,j} + n_1 d_{i+1,j+1}u_{i+1,j+1} - \\
&\quad - n_1 a_{start}u_{i_{start},j_{start}} - n_1 b_{start}u_{i_{start},j_{start}+1} - n_1 c_{start}u_{i_{start}+1,j_{start}} - \\
&\quad - n_1 d_{start}u_{i_{start}+1,j_{start}+1} + n_2 a_{ij}v_{ij} + n_2 b_{i,j+1}v_{i,j+1} + n_2 c_{i+1,j}v_{i+1,j} + \\
&\quad + n_2 d_{i+1,j+1}v_{i+1,j+1} - n_2 a_{start}v_{i_{start},j_{start}} - n_2 b_{start}v_{i_{start},j_{start}+1} - \\
&\quad - n_2 c_{start}v_{i_{start}+1,j_{start}} - n_2 d_{start}v_{i_{start}+1,j_{start}+1})^2,
\end{aligned}$$

where $a_{ij}, b_{i,j+1}, c_{i+1,j}, d_{i+1,j+1}, a_{start}, b_{start}, c_{start}, d_{start}$ are the bilinear coefficients used to define the output virtual vertices.

We can rewrite $E_{lo}\big|_l$ as $E_{lo}\big|_l = \| LO^{(l)}\mathbf{x} \|^2$, making each quad $q_{ij} \in V_l$ corresponds to a line in $LO^{(l)}$, say the q-th line [7]:

$$\begin{aligned}
LO^{(l)}_{q,2(j+i(n+1))} &= n_1 a_{ij}, & LO^{(l)}_{q,2((j+1)+i(n+1))} &= n_1 b_{i,j+1}, \\
LO^{(l)}_{q,2(j+(i+1)(n+1))} &= n_1 c_{i+1,j}, & LO^{(l)}_{q,2((j+1)+(i+1)(n+1))} &= n_1 d_{i+1,j+1}, \\
LO^{(l)}_{q,2(j_{start}+i_{start}(n+1))} &= -n_1 a_{start}, & LO^{(l)}_{q,2((j_{start}+1)+i_{start}(n+1))} &= -n_1 b_{start}, \\
LO^{(l)}_{q,2(j_{start}+(i_{start}+1)(n+1))} &= -n_1 c_{start}, & LO^{(l)}_{q,2((j_{start}+1)+(i_{start}+1)(n+1))} &= -n_1 d_{start}, \\
LO^{(l)}_{q,2(j+i(n+1))+1} &= n_2 a_{ij}, & LO^{(l)}_{q,2((j+1)+i(n+1))+1} &= n_2 b_{i,j+1}, \\
LO^{(l)}_{q,2(j+(i+1)(n+1))+1} &= n_2 c_{i+1,j}, & LO^{(l)}_{q,2((j+1)+(i+1)(n+1))+1} &= n_2 d_{i+1,j+1}, \\
LO^{(l)}_{q,2(j_{start}+i_{start}(n+1))+1} &= -n_2 a_{start}, & LO^{(l)}_{q,2((j_{start}+1)+i_{start}(n+1))+1} &= -n_2 b_{start}, \\
LO^{(l)}_{q,2(j_{start}+(i_{start}+1)(n+1))+1} &= -n_2 c_{start}, & LO^{(l)}_{q,2((j_{start}+1)+(i_{start}+1)(n+1))+1} &= -n_2 d_{start}.
\end{aligned}$$

The other entries of $LO^{(l)}$ are set to be zero.

We want the energy for all lines in $L_f = \{l^{(f)}_0, \ldots, l^{(f)}_{k_1-1}\}$, i.e.,

$$E_{lo} = \sum_{l\in L_f} E_{lo}\big|_l = \sum_{l\in L_f}\sum_{q_{ij}\in V_l} \left((\mathbf{u}^l_{ij} - \mathbf{u}^l_{start})^T \begin{pmatrix} n_1 \\ n_2 \end{pmatrix} \right)^2.$$

The above construction is made for each line, leading to matrices

$$LO^{(l^{(f)}_0)}, LO^{(l^{(f)}_1)}, \ldots, LO^{(l^{(f)}_{k_1-1})}$$

[7] We use here the notation of section 2.4.3 to construct $LO^{(l)}$ and $\mathbf{x}$.

that correspond to the inner sums and define

$$LO = \begin{pmatrix} LO^{(l_0^{(f)})} \\ \vdots \\ LO^{(l_{k_1-1}^{(f)})} \end{pmatrix}.$$

We call LO the *fixed orientation line matrix*. Observing that each line of LO has at most 8 nonzero entries per line (since $n_1 = 0$ or $n_2 = 0$, in this case), we conclude that LO is sparse.

The conclusion $E_{lo} = \| LO\mathbf{x} \|^2$ is straightforward:

$$\begin{aligned} \| LO\mathbf{x} \|^2 &= \left\| \begin{pmatrix} LO^{(l_0^{(f)})} \\ \vdots \\ LO^{(l_{k_1-1}^{(f)})} \end{pmatrix} \mathbf{x} \right\|^2 = \left\| \begin{pmatrix} LO^{(l_0^{(f)})}\mathbf{x} \\ \vdots \\ LO^{(l_{k_1-1}^{(f)})}\mathbf{x} \end{pmatrix} \right\|^2 \\ &= \| LO^{(l_0^{(f)})}\mathbf{x} \|^2 + \ldots + \| LO^{(l_{k_1-1}^{(f)})}\mathbf{x} \|^2 \\ &= E_{lo}\big|_{l_0^{(f)}} + \ldots + E_{lo}\big|_{l_{k_1-1}^{(f)}} = \sum_{l \in L_f} E_{lo}\big|_l = E_{lo}. \end{aligned}$$

We now focus on the lines that have no specified orientation, i.e., the set $L \backslash L_f = \{l_0^{(g)}, \ldots l_{k_2-1}^{(g)}\}$. As we explained, we alternate between minimizing E_{lo} and E_{ld} for such lines.

To turn E_{lo} into a matrix form, we do the same way we did for lines with fixed orientation: for each $l_k^{(g)} \in L \backslash L_f$, $k = 0, \ldots, k_2 - 1$, we construct the matrix $LO^{l_k^{(g)}}$ in the same way we did before and define

$$LOA = \begin{pmatrix} LO^{(l_0^{(g)})} \\ \vdots \\ LO^{(l_{k_2-1}^{(g)})} \end{pmatrix}.$$

We call LOA the *alternate fixed orientation line matrix*. Since now we can have $n_1 \neq 0$ and $n_2 \neq 0$, each line of LOA has at most 16 nonzero entries. So it is still sparse[8].

Let $l \in L \backslash L_f$. Developing the expression for $E_{ld}\big|_l$ we obtain:

$$\begin{aligned} E_{ld}\big|_l &= \sum_{q_{ij} \in V_l} \big\| a_{ij}\mathbf{u}_{ij} + b_{i,j+1}\mathbf{u}_{i,j+1} + c_{i+1,j}\mathbf{u}_{i+1,j} + d_{i+1,j+1}\mathbf{u}_{i+1,j+1} + \\ &\quad + (-1 + s_{ij}) a_{start}\mathbf{u}_{i_{start},j_{start}} + (-1 + s_{ij}) b_{start}\mathbf{u}_{i_{start},j_{start}+1} + \\ &\quad + (-1 + s_{ij}) c_{start}\mathbf{u}_{i_{start}+1,j_{start}} + (-1 + s_{ij}) d_{start}\mathbf{u}_{i_{start}+1,j_{start}+1} - \\ &\quad - s_{ij} a_{end}\mathbf{u}_{i_{end},j_{end}} - s_{ij} b_{end}\mathbf{u}_{i_{end},j_{end}+1} - s_{ij} c_{end}\mathbf{u}_{i_{end}+1,j_{end}} - s_{ij} d_{end}\mathbf{u}_{i_{end}+1,j_{end}+1} \big\|^2 \\ &= \sum_{q_{ij} \in V_l} [(a_{ij}u_{ij} + b_{i,j+1}u_{i,j+1} + \ldots - s_{ij} c_{end} u_{i_{end}+1,j_{end}} - s_{ij} d_{end} u_{i_{end}+1,j_{end}+1})^2 + \\ &\quad + (a_{ij}v_{ij} + b_{i,j+1}v_{i,j+1} + \ldots - s_{ij} c_{end} v_{i_{end}+1,j_{end}} - s_{ij} d_{end} v_{i_{end}+1,j_{end}+1})^2], \end{aligned}$$

[8]The system usually has thousands of variables (the number of variables is two times the number of vertices).

where '...' corresponds to the middle 8 terms that are being omitted by convenience.

To obtain $E_{ld}\big|_l = \| \ LD^{(l)}\mathbf{x} \ \|^2$ we associate 2 lines of $LD^{(l)}$ to each quad $q_{ij} \in V_l$, say q_1-th and (q_1+1)-th lines, and define its entries as:

$$\begin{aligned}
LD^{(l)}_{q_1,2(j+i(n+1))} &= a_{ij}, & LD^{(l)}_{q_1,2((j+1)+i(n+1))} &= b_{ij}, \\
&\vdots & &\vdots \\
LD^{(l)}_{q_1,2(j_{end}+(i_{end}+1)(n+1))} &= -s_{ij}c_{end}, & LD^{(l)}_{q_1,2((j_{end}+1)+(i_{end}+1)(n+1))} &= -s_{ij}d_{end}, \\
LD^{(l)}_{q_1+1,2(j+i(n+1))+1} &= a_{ij}, & LD^{(l)}_{q_1+1,2((j+1)+i(n+1))+1} &= b_{ij}, \\
&\vdots & &\vdots \\
LD^{(l)}_{q_1+1,2(j_{end}+(i_{end}+1)(n+1))+1} &= -s_{ij}c_{end}, & LD^{(l)}_{q_1+1,2((j_{end}+1)+(i_{end}+1)(n+1))+1} &= -s_{ij}d_{end}.
\end{aligned}$$

The other entries of $LD^{(l)}$ are zero.

If we do the above process for each line in $L \backslash L_f$ we obtain the matrices

$$LD^{(l_0^{(g)})}, LD^{(l_1^{(g)})}, \ldots, LD^{(l_{k_2-1}^{(g)})}.$$

We define the *alternate fixed projection line matrix* to be

$$LDA = \begin{pmatrix} LD^{(l_0^{(g)})} \\ \vdots \\ LD^{(l_{k_2-1}^{(g)})} \end{pmatrix}.$$

LDA is also sparse, since it has at most 12 nonzero entries per row.

It turns out that

$$E_{ld} = \sum_{l \in L \backslash L_f} E_{ld}\big|_l$$

which can be written as

$$E_{ld} = \| \ LDA\mathbf{x} \ \|^2 \ .$$

This conclusion is obtained in the same manner we did before to obtain $E_{lo} = \| \ LO\mathbf{x} \ \|^2$.

We now have both energies in a matrix form. The minimization for all lines (the set L) is performed by first minimizing

$$\sum_{l \in L_f} E_{lo}\big|_l + \sum_{l \in L \backslash L_f} E_{ld}\big|_l = \| \ LO\mathbf{x} \ \|^2 + \| \ LDA\mathbf{x} \ \|^2$$

and then plugging the obtained values into $\sum_{l \in L \backslash L_f} E_{lo}\big|_l$ and minimizing

$$\sum_{l \in L_f} E_{lo}\big|_l + \sum_{l \in L \backslash L_f} E_{lo}\big|_l = \| \ LO\mathbf{x} \ \|^2 + \| \ LOA\mathbf{x} \ \|^2 \ .$$

The obtained values are plugged into $\sum_{l \in L \backslash L_f} E_{ld}\big|_l$ and the process continues until convergence is reached.

More details of such minimization are left to section 2.8, where such energies are minimized with other ones.

An example that one would obtain when minimizing only line energies is shown in figure 2.16.

Figure 2.16: The method tries to straighten the specified lines, but due to the discontinuous nature of the straight line constrains, the result becomes very unpleasant.

2.5.2 Inverting Bilinear Interpolation

This section is devoted to obtain the bilinear coefficients a, b, c, d used to define the output virtual vertices.

As we explained, such coefficients are obtained in the following way:

• Given $A, B, C, D \in \mathbb{S}^2$, project them orthogonally on the plane tangent to $\mathbb{S}^2$ passing through $P = (P_1, P_2, P_3)$, say $\prod$, and obtain $\tilde{A}, \tilde{B}, \tilde{C}, \tilde{D}$;

• Obtain a, b, c, d such that $P = a\tilde{A} + b\tilde{B} + c\tilde{C} + d\tilde{D}$.

The first step is quite simple: the equation of $\prod$ is

$$\prod : P_1(x - P_1) + P_2(y - P_2) + P_3(z - P_3) = 0$$

which can be rewritten as

$$\prod : P_1 x + P_2 y + P_3 z = 1.$$

If $\tilde{A}$ is the orthogonal projection of A (see figure 2.17), it satisfies

$$\tilde{A} - A = \lambda P, \ \langle P, \tilde{A} \rangle = 1,$$

for some λ. Solving the above equations leads to

$$\tilde{A} = A + \lambda P, \text{ where } \lambda = 1 - \langle P, A \rangle.$$

The same holds for $\tilde{B}$, $\tilde{C}$ and $\tilde{D}$. Now we have the situation illustrated in figure 2.18.

Let $\mathbf{n}$ be the unit vector normal to $\prod$ (we know that in our case $\mathbf{n} = P$, but we ignore this for a while in order to obtain a general result).

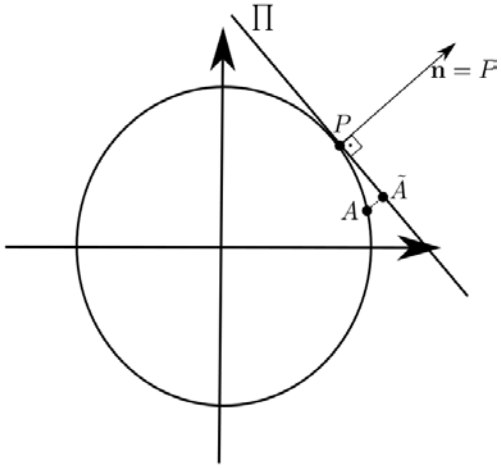

Figure 2.17: Orthogonal projection of A.

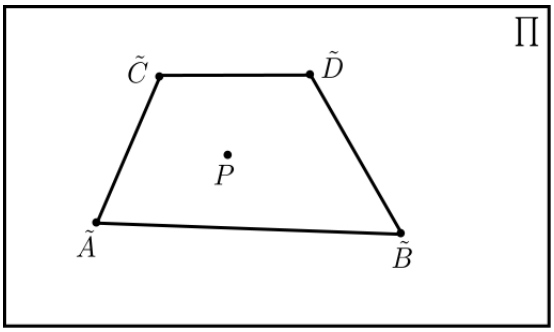

Figure 2.18: Projected vertices on tangent plane.

We first look for β such that $s_{1,\beta} = (1-\beta)\tilde{A} + \beta\tilde{C}$, $s_{2,\beta} = (1-\beta)\tilde{B} + \beta\tilde{D}$, and P are collinear (figure 2.19).

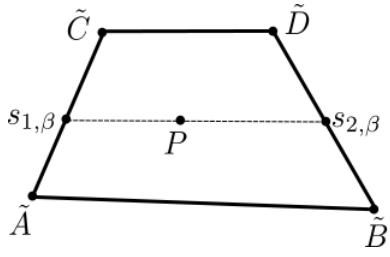

Figure 2.19: P, $s_{1,\beta}$ and $s_{2,\beta}$ must be collinear.

Since $\mathbf{n}$ is orthogonal to $\overrightarrow{s_{1,\beta}P} = P - s_{1,\beta}$ and $\overrightarrow{s_{1,\beta}s_{2,\beta}} = s_{2,\beta} - s_{1,\beta}$, this is equivalent to the volume defined by $\mathbf{n}$, $\overrightarrow{s_{1,\beta}P}$ and $\overrightarrow{s_{1,\beta}s_{2,\beta}}$ to be zero, i.e.,

$$\mathbf{n} \cdot ((P - s_{1,\beta}) \times (s_{2,\beta} - s_{1,\beta})) = 0,$$

where $\cdot$ denotes the usual inner product and $\times$ denotes the cross product in $\mathbb{R}^3$.

Developing the above expression we obtain

$$\begin{aligned}
0 &= \mathbf{n}\cdot((P-s_{1,\beta})\times(s_{2,\beta}-s_{1,\beta}))\\
&= \mathbf{n}\cdot(P\times s_{2,\beta}-P\times s_{1,\beta}-s_{1,\beta}\times s_{2,\beta}+\underbrace{s_{1,\beta}\times s_{1,\beta}}_{0})\\
&= \mathbf{n}\cdot[P\times((1-\beta)\tilde{B}+\beta\tilde{D})-P\times((1-\beta)\tilde{A}+\beta\tilde{C})-\\
&\quad -((1-\beta)\tilde{A}+\beta\tilde{C})\times((1-\beta)\tilde{B}+\beta\tilde{D})]\\
&= \mathbf{n}\cdot[(1-\beta)(P\times\tilde{B})+\beta(P\times\tilde{D})-(1-\beta)(P\times\tilde{A})-\beta(P\times\tilde{C})-\\
&\quad -(1-\beta)^2(\tilde{A}\times\tilde{B})-(1-\beta)\beta(\tilde{A}\times\tilde{D})-\beta(1-\beta)(\tilde{C}\times\tilde{D})-\beta^2(\tilde{C}\times\tilde{D})]\\
&= \mathbf{n}\cdot[(P\times\tilde{B})-(P\times\tilde{A})-(\tilde{A}\times\tilde{B})]+\beta\mathbf{n}\cdot[(P\times\tilde{B})+(P\times\tilde{D})+\\
&\quad +(P\times\tilde{A})-(P\times\tilde{C})+2(\tilde{A}\times\tilde{B})-(\times A\times\times D)-(\tilde{C}\times\tilde{B})]+\\
&\quad +\beta^2\mathbf{n}[-(\tilde{A}\times\tilde{B})+(\tilde{A}\times\tilde{D})+(\tilde{C}\times\tilde{B})-(\tilde{C}\times\tilde{D})]\\
\Leftrightarrow\ 0 &= [\mathbf{n}\cdot((\tilde{C}\times\tilde{A})\times(\tilde{D}-\tilde{B}))]\beta^2+[\mathbf{n}\cdot((\tilde{D}-\tilde{B})\times(P-\tilde{A})-\\
&\quad -(\tilde{C}-\tilde{A})\times(P-\tilde{B}))]\beta+[\mathbf{n}\cdot((P-\tilde{A})\times(P-\tilde{B}))].
\end{aligned}$$

Defining

$$a_1=\langle\mathbf{n},(\tilde{C}-\tilde{A})\times(\tilde{D}-\tilde{B})\rangle,\ a_2=\langle\mathbf{n},(\tilde{D}-\tilde{B})\times(P-\tilde{A})-(\tilde{C}-\tilde{A})\times(P-\tilde{B})\rangle,$$

$$a_3=\langle\mathbf{n},(P-\tilde{A})\times(P-\tilde{B}),$$

the equation becomes

$$a_1\beta^2+a_2\beta+a_3=0,$$

which has solutions

$$\beta=\frac{-a_2\pm\sqrt{a_2^2-4a_1a_3}}{2a_1}.$$

We choose the root by analyzing the sign of $a_1=\langle\mathbf{n},(\tilde{C}-\tilde{A})\times(\tilde{D}-\tilde{B})\rangle$.

First we observe that $a_1=0$ is not possible: $\mathbf{n}$ is parallel to $(\tilde{C}-\tilde{A})\times(\tilde{D}-\tilde{B})$. Since $\mathbf{n}\neq\mathbf{0}$, $a_1=0$ would imply $(\tilde{C}-\tilde{A})\times(\tilde{D}-\tilde{B})=\mathbf{0}$, which means $(\tilde{C}-\tilde{A})$ and $(\tilde{D}-\tilde{B})$ are collinear and this does not happen by construction.

Now suppose $a_1<0$. This means that $\mathbf{n}$, $(\tilde{C}-\tilde{A})$ and $(\tilde{D}-\tilde{B})$ have a negative orientation and thus $(\tilde{C}-\tilde{A})$ and $(\tilde{D}-\tilde{B})$ are diverging on $\prod$, as shown in figure 2.20.

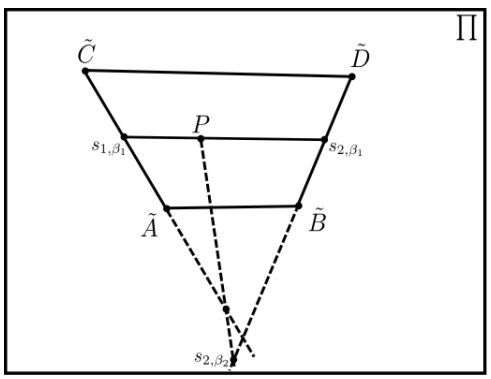

Figure 2.20: $(\tilde{C}-\tilde{A})$ and $(\tilde{D}-\tilde{B})$ diverging on $\prod$.

Figure 2.20 shows us the two possibilities for collinearity between P, $s_{1,\beta}$ and $s_{2,\beta}$. We do not want the smallest root β_2, because $\beta_2 < 0$ and $0 \leqslant \beta_1 \leqslant 1$. Since $a_1 < 0$, the largest (and desired) root is

$$\beta_1 = \frac{-a_2 - \sqrt{a_2^2 - 4a_1a_3}}{2a_1}.$$

For $a_1 > 0$ we have the situation illustrated in figure 2.21.

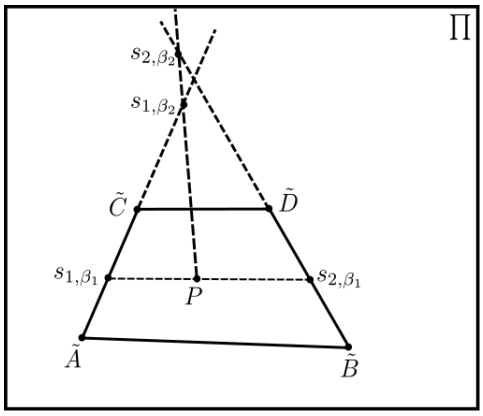

Figure 2.21: $(\tilde{C} - \tilde{A})$ and $(\tilde{D} - \tilde{B})$ converging on $\prod$.

Now the desired root β_1 is the smallest one. Since $a_1 > 0$, we have

$$\beta_1 = \frac{-a_2 - \sqrt{a_2^2 - 4a_1a_3}}{2a_1}.$$

Thus we conclude that the desired root is always obtained by taking the negative sign in the expression for β.

Now we want to find α such that

$$P = (1 - \alpha)s_{1,\beta} + \alpha s_{2,\beta},$$

as shown in figure 2.22.

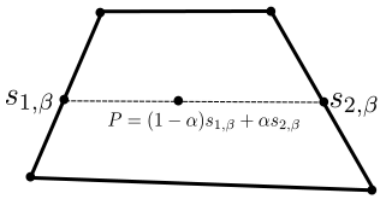

Figure 2.22: P as convex combination of $s_{1,\beta}$ and $s_{2,\beta}$.

This is achieved by defining α as the length of the projection of $\overrightarrow{s_{1,\beta}P}$ on the vector $\overrightarrow{s_{1,\beta}s_{2,\beta}}$, i.e.,

$$\alpha = \frac{\langle P - s_{1,\beta}, s_{2,\beta} - s_{1,\beta} \rangle}{\| s_{2,\beta} - s_{1,\beta} \|^2}.$$

Thus

$$\begin{aligned} P &= (1-\alpha)s_{1,\beta} + \alpha s_{2,\beta} = (1-\alpha)((1-\beta)\tilde{A} + \beta\tilde{C}) + \\ &\quad + \alpha((1-\beta)\tilde{B} + \beta\tilde{D}) = a\tilde{A} + b\tilde{B} + c\tilde{C} + d\tilde{D}, \end{aligned}$$

where

$$a = (1-\alpha)(1-\beta),\ b = \alpha(1-\beta),\ c = (1-\alpha)\beta,\ d = \alpha\beta.$$

2.6 Smoothness

Joining conformality and straight line energies and minimizing them leads to a result like in figure 2.23.

Figure 2.23: The mapping changes too much to satisfy the line constrains. We want the solution to be smoother.

We can observe huge changes of scale and orientation over the image, especially near line segments.

This behavior has an explanation: conformality imposes that the differential north vector $\mathbf{h}$ is a 90-degree rotation of the differential east vector $\mathbf{k}$, i.e., $\mathbf{h} = R_{90}\mathbf{k}$. Such imposition turns the mapping $\mathbf{u}$ *locally* into a rotation composed with a uniform scale. But this rotation and scale can be very different even for two points (λ_1, ϕ_1), (λ_2, ϕ_2) that are very close in the equirectangular domain. Figure 2.24 illustrates what was just said.

We avoid such behavior by imposing small variations for both $\mathbf{h}$ and $\mathbf{k}$. If we have

$$\frac{\partial \mathbf{h}}{\partial \lambda}(\lambda, \phi) = \frac{\partial \mathbf{h}}{\partial \phi}(\lambda, \phi) = \mathbf{0},\ \forall (\lambda, \phi) \in \left(-\frac{\pi}{2}, \frac{\pi}{2}\right) \times (-\pi, \pi),$$

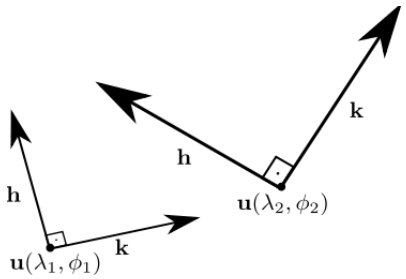

Figure 2.24: Vectors $\mathbf{h}$ and $\mathbf{k}$ varying too much for small variations of (λ, ϕ).

it follows that

$$\frac{\partial \mathbf{k}}{\partial \lambda}(\lambda,\phi) = \frac{\partial \mathbf{k}}{\partial \phi}(\lambda,\phi) = \mathbf{0},\ \forall (\lambda,\phi) \in \left(-\frac{\pi}{2}, \frac{\pi}{2}\right) \times (-\pi, \pi),$$

since $\mathbf{k} = R_{-90}\mathbf{h}$ (here we are assuming that $\mathbf{u}$ is conformal). Thus, it is enough to impose the constrains only on $\mathbf{h}$.

Hence, ideally we should have

$$\frac{\partial \mathbf{h}}{\partial(\lambda,\phi)} = \begin{pmatrix} \frac{\partial \mathbf{h}}{\partial \lambda} & \frac{\partial \mathbf{h}}{\partial \phi} \end{pmatrix} = \begin{pmatrix} \frac{\partial^2 u}{\partial \phi \partial \lambda} & \frac{\partial^2 u}{\partial \phi^2} \\ \frac{\partial^2 v}{\partial \phi \partial \lambda} & \frac{\partial^2 v}{\partial \phi^2} \end{pmatrix} = \begin{pmatrix} 0 & 0 \\ 0 & 0 \end{pmatrix},$$

i.e.,

$$\frac{\partial^2 u}{\partial \phi^2}(\lambda,\phi) = 0,\ \frac{\partial^2 v}{\partial \phi^2}(\lambda,\phi) = 0,\ \frac{\partial^2 u}{\partial \phi \partial \lambda}(\lambda,\phi) = 0,\ \frac{\partial^2 v}{\partial \phi \partial \lambda}(\lambda,\phi) = 0,\ \forall (\lambda,\phi).$$

2.6.1 Energy Term

We impose the last equations on the vertices $(\lambda_{ij}, \phi_{ij})$, $i = 1, \ldots, m-1$, $j = 0, \ldots, n-1$, of the discretization of the viewing sphere and approximate the second derivatives using second-order finite differences:

$$\frac{\partial^2 u}{\partial \phi^2}(\lambda_{ij},\phi_{ij}) \approx \frac{u_{i+1,j} - 2u_{ij} + u_{i-1,j}}{(\Delta\phi)^2},\quad \frac{\partial^2 v}{\partial \phi^2}(\lambda_{ij},\phi_{ij}) \approx \frac{v_{i+1,j} - 2v_{ij} + v_{i-1,j}}{(\Delta\phi)^2},$$
$$\frac{\partial^2 u}{\partial \lambda \partial \phi} \approx \frac{u_{i+1,j+1} - u_{i,j+1} - u_{i+1,j} + u_{i,j}}{\Delta\lambda\Delta\phi},\quad \frac{\partial^2 v}{\partial \lambda \partial \phi} \approx \frac{v_{i+1,j+1} - v_{i,j+1} - v_{i+1,j} + v_{i,j}}{\Delta\lambda\Delta\phi}.$$

To obtain the smoothness energy, we also multiply the equations by spatially varying weights (section 2.7) that control the strength of such energy on different areas of the panorama, and again by $\cos(\phi_{ij})$ to make the energy depend on the area of the quad:

$$\begin{aligned} E_s \;=\; & \sum_{i=1}^{m-1}\sum_{j=0}^{n-1} w_{ij}^2 \cos^2(\phi_{ij}) \left(\frac{u_{i+1,j} - 2u_{ij} + u_{i-1,j}}{(\Delta\phi)^2}\right)^2 + \\ & + \sum_{i=1}^{m-1}\sum_{j=0}^{n-1} w_{ij}^2 \cos^2(\phi_{ij}) \left(\frac{v_{i+1,j} - 2v_{ij} + v_{i-1,j}}{(\Delta\phi)^2}\right)^2 + \\ & + \sum_{i=1}^{m-1}\sum_{j=0}^{n-1} w_{ij}^2 \cos^2(\phi_{ij}) \left(\frac{u_{i+1,j+1} - u_{i,j+1} - u_{i+1,j} + u_{i,j}}{\Delta\lambda\Delta\phi}\right)^2 + \\ & + \sum_{i=1}^{m-1}\sum_{j=0}^{n-1} w_{ij}^2 \cos^2(\phi_{ij}) \left(\frac{v_{i+1,j+1} - v_{i,j+1} - v_{i+1,j} + v_{i,j}}{\Delta\lambda\Delta\phi}\right)^2. \end{aligned}$$

As the other energies, we turn E_s into a matrix form: $E_s = \| S\mathbf{x} \|^2$. Each double summation of the energy must correspond to a line in S. Thus S has $4(m-1)(n)$ lines. The entries of S are:

$$S_{4(j+(i-1)n),2(j+(i+1)(n+1))} = \frac{w_{ij}\cos\phi_{ij}}{(\Delta\phi)^2}, \quad S_{4(j+(i-1)n),2(j+i(n+1))} = -\frac{2w_{ij}\cos\phi_{ij}}{(\Delta\phi)^2},$$

$$S_{4(j+(i-1)n),2(j+(i-1)(n+1))} = \frac{w_{ij}\cos\phi_{ij}}{(\Delta\phi)^2}, \quad S_{4(j+(i-1)n)+1,2(j+(i+1)(n+1))+1} = \frac{w_{ij}\cos\phi_{ij}}{(\Delta\phi)^2},$$

$$S_{4(j+(i-1)n)+1,2(j+i(n+1))+1} = -\frac{2w_{ij}\cos\phi_{ij}}{(\Delta\phi)^2}, \quad S_{4(j+(i-1)n)+1,2(j+(i-1)(n+1))+1} = \frac{w_{ij}\cos\phi_{ij}}{(\Delta\phi)^2},$$

$$S_{4(j+(i-1)n)+2,2((j+1)+(i+1)(n+1))} = \frac{w_{ij}\cos\phi_{ij}}{\Delta\lambda\Delta\phi}, \quad S_{4(j+(i-1)n)+2,2((j+1)+i(n+1))} = -\frac{w_{ij}\cos\phi_{ij}}{\Delta\lambda\Delta\phi},$$

$$S_{4(j+(i-1)n)+2,2(j+(i+1)(n+1))} = -\frac{w_{ij}\cos\phi_{ij}}{\Delta\lambda\Delta\phi}, \quad S_{4(j+(i-1)n)+2,2(j+i(n+1))} = \frac{w_{ij}\cos\phi_{ij}}{\Delta\lambda\Delta\phi},$$

$$S_{4(j+(i-1)n)+3,2((j+1)+(i+1)(n+1))+1} = \frac{w_{ij}\cos\phi_{ij}}{\Delta\lambda\Delta\phi}, \quad S_{4(j+(i-1)n)+3,2((j+1)+i(n+1))+1} = -\frac{w_{ij}\cos\phi_{ij}}{\Delta\lambda\Delta\phi},$$

$$S_{4(j+(i-1)n)+3,2(j+(i+1)(n+1))+1} = -\frac{w_{ij}\cos\phi_{ij}}{\Delta\lambda\Delta\phi}, \quad S_{4(j+(i-1)n)+3,2(j+i(n+1))+1} = \frac{w_{ij}\cos\phi_{ij}}{\Delta\lambda\Delta\phi},$$

$i = 1, \ldots, m-1$, $j = 0, \ldots, n-1$. The other entries are defined as zero. S is called the *smoothness matrix*. S has at most 4 nonzero entries per row, so it is sparse.

Minimizing only the smoothness energy leads to results like the one in figure 2.25.

Figure 2.25: The solution for minimizing only E_s.

Joining the smoothness energy to conformality and straight line energies causes the expected result on the image in the beginning if this section, as shown in figure 2.26.

2.7 Spatially-Varying Weighting

In this section we present the weights w_{ij} used to define conformality and smoothness energies. Each w_{ij} is associated to a vertex on the viewing sphere Λ_{ij}. They control shape distortions and variation of the projection in different regions of the panoramic image.

Figure 2.26: Joining all the energies together leads to a smoother solution. Observe that the undesirable artifacts in figure 2.23 are corrected.

These weights strongly depend on the image content, which was pointed out as a desirable property in section 2.1.

We construct the weighting function based on three quantities: proximity to a line endpoint, a local image salience measure and proximity to a face.

• **Line endpoint weights:** The straight line constrains are very discontinuous along the projection: while a vertex may have no such constrain, another one very close to it may be the beginning of a line, where a strong constrain is imposed. This behavior leads to more distorted quads near line endpoints.

We thus define weights w_{ij}^L that are stronger near line endpoints, to make conformality and smoothness energies correct this problem.

Let $p = (\lambda, \phi)$ be an endpoint. Suppose $p \in [\lambda_{i_p,j_p}, \lambda_{i_p,j_p+1}] \times [\phi_{i_p,j_p}, \phi_{i_p+1,j_p}]$ (figure 2.27).

For each $i = 0, \ldots, m,\ j = 0, \ldots, n$ we calculate the value of a gaussian function centered on (i_p, j_p) with deviation $\sigma = \frac{n}{100}$ and height equal to 1:

$$w_{ij}^{(p)} = e^{\frac{(i-i_p)^2+(j-j_p)^2}{2\sigma^2}}.$$

To define the final weight w_{ij}^L for the vertex Λ_{ij}, we just sum over all endpoints:

$$w_{ij}^L = \sum_{p\ endpoint} w_{ij}^{(p)} = \sum_{p\ endpoint} e^{\frac{(i-i_p)^2+(j-j_p)^2}{2\sigma^2}}.$$

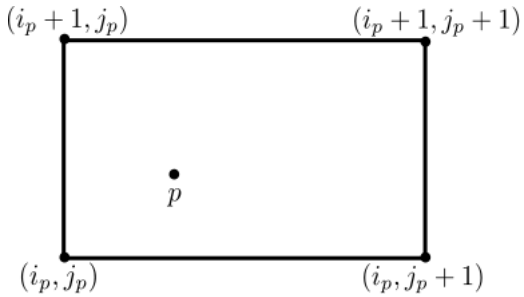

Figure 2.27: p and its corresponding quad.

In figure 2.28 we compare a result without and with such weights.

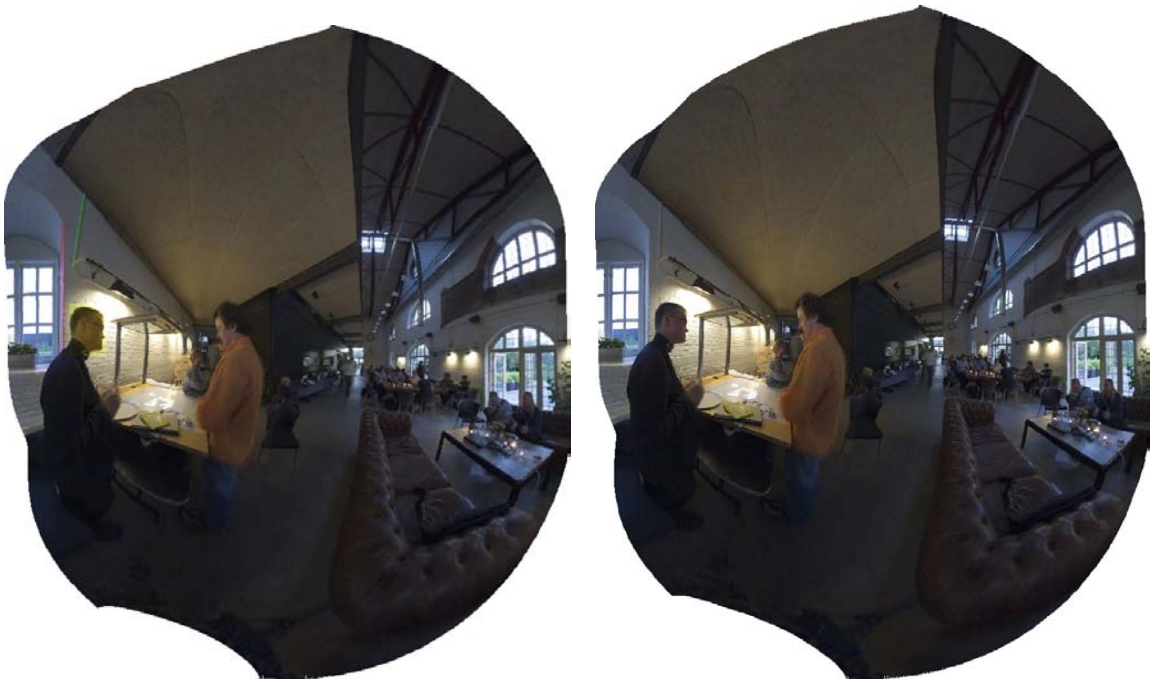

Figure 2.28: Left: Without line endpoint weights. Right: With them. Two close line segments in the left image (highlighted in red and green) have too different orientations, problem corrected in the right image. Also, the face highlighted in yellow in the left image is near a line segment and becomes too stretched, fact less noticeable in the right image.

• **Salience weights:** These weights w_{ij}^S are constructed based on the observation that in areas of the image with many details the projection should be smoother and in other ares like skies or walls the projection could have a worse behavior that it wouldn't be noticed.

We construct w_{ij}^S as follows: suppose $1 \leqslant i \leqslant m-1$, $1 \leqslant j \leqslant n-1$[9]. We take the mean value of luminance on the 3 by 3 window centered on Λ_{ij}:

$$mean_{ij} = \frac{L_{i-1,j-1} + L_{i-1,j} + L_{i-1,j+1} + L_{i,j-1} + L_{i,j} + L_{i.j+1} + L_{i+1,j-1} + L_{i+1,j} + L_{i+1,j+1}}{9},$$

where L_{ij} is the luminance of the corresponding pixel to Λ_{ij} on the equirectangular image.

[9]For boundary vertices the construction is similar.

Then we obtain the standard deviation of luminance on the window:

$$dev_{ij} = \sqrt{\frac{\sum_{k,l}(L_{k,l} - mean_{ij})^2}{9}}.$$

Finally we define w_{ij}^S by normalizing the deviations to be between 0 and 1:

$$w_{ij}^S = \frac{dev_{ij} - \min_{ij} dev_{ij}}{\max_{ij} dev_{ij} - \min_{ij} dev_{ij}}$$

In figure 2.29 we show a result without and with these weights:

Figure 2.29: Left: Without salience weights. Right: With them. The difference is very subtle.

• **Face detection weights:** Even little distortions in human faces are very noticeable. Thus we would like shapes of faces to be especially preserved. This is achieved by increasing conformality in face regions.

To do that, we should be able to detect faces in equirectangular images. This process is detailed in section 2.8, where we discuss theory and implementation of a standard face detector ([16]) and describe a way of applying it to equirectangular images. From this face detection process, a weight field w_{ij}^F is obtained. Such field has higher values in face regions.

In figure 2.30 we compare a result without and with the face weights w_{ij}^F.

• **Total weights:** We use the combination of the 3 kinds of weights suggested in [1] in order to define the total weights:

$$w_{ij} = 2w_{ij}^L + 2w_{ij}^S + 4w_{ij}^F + 1.$$

Figure 2.30: Result without and with face weights. Such weights are the most effective ones, as can be seen in the woman's face, that looks less distorted in the bottom image.

2.8 Minimization

Up to now in this chpater, we modeled some kinds of distortion in panoramic images and derived some energies (conformality, straight line and smoothness energies) that measure how distorted an image is.

Thus, ideally, we would like to find mappings $\mathbf{u}$ with null energies. We already discussed the difficulties of finding distortion-free mappings in Chapter 1. Also, in the result discussion in section 3.7, we prove an additional statement that says the only mappings that satisfy both conformality and smoothness conditions are the constant ones. Therefore, a more reasonable solution is to minimize all the energies in some sense.

In this section, we formulate an energy that is a sum of all energies obtained up to

here. Such quantity takes into account all types of distortions.

We then study two ways to minimize it: one that is exact but slow, and another that provides an approximate solution fast.

2.8.1 Total Energy

In order to formulate the total energy, we use weights w_c, w_s and w_l that control the relative importance of the conformality, smoothness and line energies. The total energy will be a weighted sum of such energies. The (fixed) values for such weights are defined in section 2.8.4.

If the values of the projections s_{ij} (section 2.5) are set, the energy to be minimized is:

$$E_d = w_c^2 E_c + w_s^2 E_s + w_l^2 \sum_{l \in L_f} E_{lo} + w_l^2 \sum_{l \in L \setminus L_f} E_{ld}.$$

If the normal vectors $\mathbf{n}$ (section 2.5) are set, the energy is:

$$E_o = w_c^2 E_c + w_s^2 E_s + w_l^2 \sum_{l \in L_f} E_{lo} + w_l^2 \sum_{l \in L \setminus L_f} E_{lo}.$$

We thus alternate between minimizing these two energies in the same way described in section 2.5.

By defining

$$A_d = \begin{pmatrix} w_c C \\ w_s S \\ w_l LO \\ w_l LDA \end{pmatrix} \text{ and } A_o = \begin{pmatrix} w_c C \\ w_s S \\ w_l LO \\ w_l LOA \end{pmatrix},$$

where C, S, LO, LDA and LOA are the conformality, smoothness and straight line matrices, we can rewrite both energies as

$$E_d = \|A_d \mathbf{x}\|^2 \text{ and } E_o = \|A_o \mathbf{x}\|^2.$$

We use here again the notation established in section 2.4.3:

$$\mathbf{x}_{2(j+i(n+1))} = u_{ij} \text{ and } \mathbf{x}_{2(j+i(n+1))+1} = v_{ij}.$$

2.8.2 Eigenvalue/Eigenvector Method

For this section and the next one, we drop off the indices of E_d and E_o and study two different ways of minimizing

$$E(\mathbf{x}) = \|A\mathbf{x}\|^2.$$

Let $\mathbf{x} \neq \mathbf{0}$[10]. The equality

$$E(\mathbf{x}) = E\left(\|\mathbf{x}\| \frac{\mathbf{x}}{\|\mathbf{x}\|}\right) = \left\| A\|\mathbf{x}\| \frac{\mathbf{x}}{\|\mathbf{x}\|} \right\|^2 = \|\mathbf{x}\|^2 E\left(\frac{\mathbf{x}}{\|\mathbf{x}\|}\right)$$

[10] $\mathbf{x} = \mathbf{0}$ is a minimizer for E but it's an undesirable solution since corresponds to mapping all the viewing sphere to the origin.

shows us that E is unbounded and has no minimum or maximum for $\mathbf{x} \neq \mathbf{0}$.

Since $E(\mathbf{x})$ is proportional to $E\left(\frac{\mathbf{x}}{\|\mathbf{x}\|}\right)$, it turns out that the set $\{\mathbf{x} : \|\mathbf{x}\| = 1\}$ is a good place to look for a minimizer. The result of

$$\min_{\|\mathbf{x}\|=1} E(\mathbf{x})$$

tells us the direction of minimal increase for E. For our purposes, the direction is the only thing that matters, since scaling the final mapping will not change its final shape.

Statement 2.3 *The solution of* $\min_{\|\boldsymbol{x}\|=1} \|A\boldsymbol{x}\|^2$ *is* $\boldsymbol{e}_1$*, the eigenvector of* A^TA *associated to its smallest eigenvalue* λ_1*. In addition,* $E(\boldsymbol{e}_1) = \lambda_1^2$*.*

Proof: Since A^TA is symmetric and positive semidefinite ($\mathbf{x}^TA^TA\mathbf{x} \geqslant 0$, $\forall \mathbf{x}$) it has an orthonormal basis of eigenvectors $\mathbf{e}_i$ $(i = 1, \ldots, q)$ with eigenvalues $0 \leqslant \lambda_1 \leqslant \lambda_2 \leqslant \ldots \leqslant \lambda_q$. Thus any unit vector can be written as

$$\mathbf{x} = \mu_1\mathbf{e}_1 + \ldots \mu_q\mathbf{e}_q,$$

where $\mu_1^2 + \ldots \mu_q^2 = 1$.
The first conclusion of the statement comes from

$$\begin{aligned} E(\mathbf{x}) - E(\mathbf{e}_1) &= \mathbf{x}^T(A^TA)\mathbf{x} - \mathbf{e}_1^T(A^TA)\mathbf{e}_1 \\ &= \lambda_1^2\mu_1^2 + \ldots + \lambda_q^2\mu_q^2 - \lambda_1^2 \\ &\geqslant \lambda_1^2\mu_1^2 + \ldots \lambda_1^2\mu_q^2 - \lambda_1^2 \\ &= \lambda_1^2(\mu_1^2 + \ldots \mu_q^2) - \lambda_1^2 = 0 \end{aligned}$$

$\Rightarrow E(\mathbf{x}) \geqslant E(\mathbf{e}_1), \forall \mathbf{x}$ s.t. $\|\mathbf{x}\| = 1$.
The other conclusion is straightforward.

■

One could think that the above statement solves our problem: it would be enough to find the smallest eigenvalue of A^TA and its associated eigenvector.

But a problem arises:

Statement 2.4 *The vectors* $\boldsymbol{x}$ *such that* $u_{ij} = k_u$ *and* $v_{ij} = k_v$*,* $\forall i, j$ *are eigenvectors of* A^TA *with corresponding eigenvalues equal to 0.*

Proof: We consider $A = A_d$. The case $A = A_o$ is analogous.
All energies E_c, E_s, E_{lo} and E_{ld} vanish if we plug into them constant values for u_{ij}'s and v_{ij}'s (this fact is straightforward from the expression for each energy).
Thus, for $u_{ij} = k_u$ and $v_{ij} = k_v$ we have

$$E_d = w_c^2E_c + w_s^2E_s + w_l^2\sum_{l\in L_f} E_{lo} + w_l^2\sum_{l\in L\setminus L_f} E_{ld} = w_c^2 0 + w_s^2 0 + w_l^2\sum_{l\in L_f} 0 + w_l^2\sum_{l\in L\setminus L_f} 0 = 0$$

which implies $\|A\mathbf{x}\|^2 = \|A_d\mathbf{x}\|^2 = 0$ and obviously $A\mathbf{x} = \mathbf{0}$. Then we have

$$A^TA\mathbf{x} = A^T \cdot \mathbf{0} = \mathbf{0} = 0 \cdot \mathbf{x}$$

and this proves the statement.

■

We do not want constant mapping as solutions because they do not satisfy the perceptual requirements that we discussed in the first chapter.

The subspace of constant mappings $K = \{\mathbf{x} : u_{ij} = k_u, v_{ij} = k_v\}$ has dimension 2, since $K = span\{\mathbf{vu}, \mathbf{vv}\}$, where $\mathbf{vu}$ has entries $v_{ij} = 0$ and $u_{ij} = \frac{1}{\sqrt{(m+1)(n+1)}}$ and $\mathbf{vv}$ has entries $u_{ij} = 0$ and $v_{ij} = \frac{1}{\sqrt{(m+1)(n+1)}}$.

If we look for $\min E(\mathbf{x})$ in $\{\mathbf{x} : \|\mathbf{x}\| = 1, \mathbf{x} \neq \mathbf{vu}, \mathbf{x} \neq \mathbf{vv}\}$ it may happen that E has no minimizer, since such set is not compact anymore.

Thus we restrict our minimization to $\{\mathbf{x} : \|\mathbf{x} = 1\|\} \cap K^{\perp}$. Assuming $\mathbf{e}_1 = \mathbf{vu}$, $\mathbf{e}_2 = \mathbf{vv}$[11] in the proof of Statement 2.3, we have

$$\{\mathbf{x} : \|\mathbf{x} = 1\|\} \cap K^{\perp} = \{\mu_3\mathbf{e}_3 + \ldots \mu_q\mathbf{e}_q : \mu_3^2 + \ldots + \mu_q^2 = 1\}.$$

In the same way we did in the proof of such statement, we conclude that the minimizer is $\mathbf{e}_3$ and $E(\mathbf{e}_3) = \lambda_3^2$. So it is enough that we look for the eigenvector of A^TA associated to the third smallest eigenvalue.

Although we found an exact solution for our problem, finding eigenvectors numerically is never an easy task. There are some reasons for this fact:

• The problem $A\mathbf{x} = \lambda\mathbf{x}$ is nonlinear itself;

• The methods usually find faster the eigenvector associated to the smallest eigenvalue. To find the third one takes longer;

• Our problem involves thousands of variables, and the problems above become more critical.

Next section presents a modification to the problem of minimizing $E(\mathbf{x})$ that provides a good quality approximate solution and is faster.

2.8.3 Linear System Method

We replace $E(\mathbf{x})$ by other energy $\tilde{E}(\mathbf{x})$ that is $E(\mathbf{x})$ plus a small perturbation that tells how much the mapping $\mathbf{x}$ deviates from some known mapping $\mathbf{y}$:

$$\tilde{E}(\mathbf{x}) = E(\mathbf{x}) + \varepsilon\|\mathbf{x} - \mathbf{y}\|^2 = \|A\mathbf{x}\|^2 + \varepsilon\|\mathbf{x} - \mathbf{y}\|^2,$$

where $\varepsilon > 0$ is a chosen (small) value. We use the stereographic mapping (section 1.3.2) for $\mathbf{y}$.

The advantages of using such perturbed energy are discussed further. Before that, consider the following statement:

Statement 2.5 *The minimizer of $\tilde{E}$ in $\mathbb{R}^n$ is*

$$\boldsymbol{x} = (A^TA + \varepsilon I)^{-1}(\varepsilon\boldsymbol{y}).$$

[11] It turns out that in practice $\lambda_3 > 0$. Then this requirement is always satisfied.

Proof: First we look for critic points of $\tilde{E}$, i.e., we look for $\mathbf{x} \in \mathbb{R}^n$ such that $\nabla\tilde{E}(\mathbf{x}) = \mathbf{0}$. Rewriting the expression for $\tilde{E}$ leads to

$$\tilde{E}(\mathbf{x}) = \mathbf{x}^T A^T A\mathbf{x} + \varepsilon(\mathbf{x}-\mathbf{y})^T(\mathbf{x}-\mathbf{y}).$$

Thus

$$\begin{aligned}\nabla\tilde{E}(\mathbf{x}) &= \nabla(\mathbf{x}^T A^T A\mathbf{x}) + \varepsilon\nabla[(\mathbf{x}^T-\mathbf{y}^T)(\mathbf{x}-\mathbf{y})] \\ &= \nabla(\mathbf{x}^T A^T A\mathbf{x}) + \varepsilon[\nabla(\mathbf{x}^T\mathbf{x}) - \nabla(\mathbf{x}^T\mathbf{y}) - \nabla(\mathbf{y}^T\mathbf{x}) + \nabla(\mathbf{y}^T\mathbf{y})]\end{aligned}$$

We know from multivariable Calculus that $\nabla(\mathbf{x}^T A^T A\mathbf{x}) = 2A^T A\mathbf{x}$ (since $A^T A$ is symmetric), $\nabla(\mathbf{x}^T\mathbf{x}) = \nabla(\mathbf{x}^T I\mathbf{x}) = 2I\mathbf{x} = 2\mathbf{x}$, $\nabla(\mathbf{x}^T\mathbf{y}) = \nabla(\mathbf{y}^T\mathbf{x}) = \mathbf{y}$ and $\nabla(\mathbf{y}^T\mathbf{y}) = \mathbf{0}$.
Then we have

$$\nabla\tilde{E}(\mathbf{x}) = 2A^T A\mathbf{x} + 2\varepsilon\mathbf{x} - 2\varepsilon\mathbf{y}$$

and

$$\nabla\tilde{E}(\mathbf{x}) = \mathbf{0} \Rightarrow (A^T A + \varepsilon I)\mathbf{x} = \varepsilon\mathbf{y}.$$

Observe that $A^T A + \varepsilon I$ is positive definite:

$$\mathbf{x}^T(A^T A + \varepsilon I)\mathbf{x} = \mathbf{x}^T A^T A\mathbf{x} + \varepsilon\mathbf{x}^T\mathbf{x} = \underbrace{\mathbf{x}^T A^T A\mathbf{x}}_{\geqslant 0} + \underbrace{\varepsilon\|\mathbf{x}\|^2}_{>0} > 0,\ \forall\mathbf{x} \neq \mathbf{0}.$$

We know that every positive definite matrix is invertible: in fact, if it were not, there would be a $\mathbf{w} \neq \mathbf{0}$ s.t. $(A^T A + \varepsilon I)\mathbf{w} = \mathbf{0}$ and $\mathbf{w}^T(A^T A + \varepsilon I)\mathbf{w} = \mathbf{w}^T \cdot \mathbf{0} = \mathbf{0}$, what contradicts the fact that $A^T A + \varepsilon I$ is positive definite.
Thus the unique critic point for $\tilde{E}$ is

$$\hat{\mathbf{x}} = (A^T A + \varepsilon I)^{-1}(\varepsilon\mathbf{y}).$$

It remains to prove that $\hat{\mathbf{x}}$ is a minimizer. In fact,

$$\nabla\tilde{E}(\mathbf{x}) = 2A^T A\mathbf{x} + 2\varepsilon\mathbf{x} - 2\varepsilon\mathbf{y} \Rightarrow H\tilde{E}(\mathbf{x}) = 2(A^T A + \varepsilon I),\ \forall\mathbf{x} \in \mathbb{R}^n.$$

Since $A^T A + \varepsilon I$ is positive definite, we conclude that the hessian $H\tilde{E}(\mathbf{x})$ is positive definite, $\forall\mathbf{x} \in \mathbb{R}^n$, and then $\tilde{E}$ is a convex function. Also, the positiveness of $H\tilde{E}(\hat{\mathbf{x}})$ implies $\hat{\mathbf{x}}$ is a local minimizer of $\tilde{E}$. Since for convex functions all local minimizers are global minimizers, we conclude that $\hat{\mathbf{x}}$ is the global minimizer for $\tilde{E}$.

■

The main advantage of minimizing $\tilde{E}$ instead of E is that we replace an eigenvalue problem by solving a linear system.

Furthermore, $A^T A + \varepsilon I$ is sparse (since A is sparse), symmetric and positive definite. For example, Matlab (software that we used to perform the optimizations) has specific routines to solve sparse linear systems and produces results much faster.

One point that remains open is what value we choose for ε. On one hand, $\varepsilon \approx 0 \Rightarrow \tilde{E}(\mathbf{x}) = E(\mathbf{x})$ and the minimizer for $\tilde{E}$ would be very close to the minimizer for E. On the other hand, ε too small leads to instability problems when solving $(A^T A + \varepsilon I)\mathbf{x} = \varepsilon \mathbf{y}$.

Since we are dealing with a perceptual problem, we can say that a good choice for ε is a value that produces visually identical results when comparing the minimizers for E and $\tilde{E}$ and does not causes instability problems.

We show with an example in figure 2.31 that $\varepsilon = 10^{-6}$ is a good choice. We used a coarse grid (only 1,369 vertices) for the viewing sphere, because a finer one would turn the minimization of E (eigenvalue/eigenvector method) impractical.

Figure 2.31: Left: final result minimizing in each iteration energy E with the eigenvalue/eigenvector method. Right: final result minimizing in each iteration energy $\tilde{E}$ with the linear system method, $\varepsilon = 10^{-6}$.

While the eigenvalue/eigenvector method took some minutes long to perform all iterations and produce a final result, the linear system method took just some seconds.

For all reasons discussed in this section, from now on we only use the linear system method to produce the results, i.e., the function to be minimized in each iteration will be $\tilde{E}$.

Now we can understand why minimizing only E_c in section 2.4.3 led to the stereographic projection: to do such minimization, we set $w_s = w_l = 0$, $w_c \neq 0$ in E_d:

$$E_d = w_c^2 E_c + \underbrace{w_s^2}_{0} E_s + \underbrace{w_l^2}_{0} \sum_{l \in L_f} E_{lo} + \underbrace{w_l^2}_{0} \sum_{l \in L \setminus L_f} E_{ld} = w_c^2 E_c,$$

in this case.

Among all possible mappings that vanish E_c (the conformal ones), the linear system method chose the stereographic one because it also minimizes the term $\varepsilon\|\mathbf{x}-\mathbf{y}\|^2$, i.e., the stereographic projection minimizes

$$\tilde{E}(\mathbf{x}) = E_d(\mathbf{x}) + \varepsilon\|\mathbf{x}-\mathbf{y}\|^2 = w_c E_c(\mathbf{x}) + \varepsilon\|\mathbf{x}-\mathbf{y}\|^2.$$

2.8.4 Results in each iteration

In the last section, we showed how to minimize E_o and E_d separately. But, as mentioned in section 2.8.1, in order to produce a final result, we have to alternate between minimizing each one at a time. Such alternation is detailed in this section, where we also show the intermediate results produced by each iteration.

This process is necessary to to straighten the lines marked by the user with no specified orientation (the green ones in figure 2.32).

Figure 2.32: Alternating between minimizing E_o and E_d straighten the general orientation lines.

The *initial iteration* consists in minimizing

$$E_d = w_c^2 E_c + w_s^2 E_s + w_l^2 \sum_{l\in L_f} E_{lo} + w_l^2 \sum_{l\in L\setminus L_f} E_{ld} = \|A_d\mathbf{x}\|^2,$$

where A_d is defined in section 2.8.1.

As explained in section 2.5.1, in this initial iteration we define the coefficients s_{ij} (which are necessary to define E_{ld}) as the arc length between $\mathbf{r}(\Lambda_{ij})$ and $\mathbf{r}(\Lambda_{start})$ in the viewing sphere. Since this choice may be imprecise in terms of expected final result, we set a lower value for w_l in this iteration: $w_l = 10$. The other weights are $w_s = 0.05$ and $w_c = 0.4$.

The minimization process explained in last section produces $\hat{\mathbf{x}} \in \mathbb{R}^{2(m+1)(n+1)}$ that contains the positions (u_{ij}, v_{ij}) where each vertex Λ_{ij} of the viewing sphere is mapped to. In other words, $(u_{ij}, v_{ij}) = \mathbf{u}(\Lambda_{ij})$, $i = 0, 1, \ldots, m$, $j = 0, 1, \ldots, n$.

Since E is multiplicative ($E(K\mathbf{x}) = KE(\mathbf{x}), \forall K \geqslant 0$), what matters is the direction of $\hat{\mathbf{x}}$ and not its norm. We chose each iteration to return a unitary vector. Thus we return $\mathbf{x} = \dfrac{\hat{\mathbf{x}}}{\|\hat{\mathbf{x}}\|}$.

From this vector $\mathbf{x}$ we produce a function defined on the entire sphere (or on the specified field of view $S \subseteq \mathbb{S}^2$) that is a bilinear interpolation of both u_{ij}'s and v_{ij}'s values. This process is detailed in section A.2.3.

Now that we have a continuous function defined in the equirectangular domain, we just map the texture in the equirectangular image according to such function.

The result for this initial iteration is shown in figure 2.33. This partial result and the other ones shown in this section were produced with 62,000 vertices and field of view 180/180.

Figure 2.33: The initial result is not very good because the initialization of the s_{ij}'s is imprecise. For this result, the value of the energy is $E = E_d = 0.0832$.

From the vector $\mathbf{x}$ returned by the initial iteration, we compute the normal vectors $\mathbf{n}$ for each line as described in section 2.5 and minimize

$$E_o = w_c^2 E_c + w_s^2 E_s + w_l^2 \sum_{l \in L_f} E_{lo} + w_l^2 \sum_{l \in L \setminus L_f} E_{lo} = \|A_o \mathbf{x}\|^2.$$

For this iteration and all following iterations we always use $w_c = 0.4$, $w_s = 0.05$ and $w_l = 1000$. The only iteration that used different weights was the initial one.

After obtaining $\hat{\mathbf{x}}$ from the optimization, we again normalize and obtain $\mathbf{x} = \frac{\hat{\mathbf{x}}}{\|\hat{\mathbf{x}}\|}$.

From this new solution vector, we calculate the projections s_{ij} as described in section 2.5 and minimize

$$E_d = w_c^2 E_c + w_s^2 E_s + w_l^2 \sum_{l \in L_f} E_{lo} + w_l^2 \sum_{l \in L \setminus L_f} E_{ld} = \|A_d \mathbf{x}\|^2,$$

where $w_c = 0.4$, $w_s = 0.05$ and $w_l = 1000$.

Again, we normalize the solution of the optimization $\hat{\mathbf{x}}$ and obtain $\mathbf{x} = \frac{\hat{\mathbf{x}}}{\|\hat{\mathbf{x}}\|}$.

This process of first minimizing E_o and then minimizing E_o we call a *double iteration*.

The results for the first, second and third double iterations are shown in figures 2.34, 2.35 and 2.36, respectively.

Figure 2.34: Left: The minimizer of E_o. Energy value $E_o = 0.0740$. Right: The minimizer of E_d. Energy value $E_d = 0.0531$.

As can be seen, minimizing E_o produces perceptually better intermediate results. Thus, we chose to use as *final iteration* the minimization of just E_o. Figure 2.37 shows the final result for this example.

The number of double iterations needed to obtain convergence varies from case to case, but usually three double iterations are enough.

The weights w_c, w_s and w_l were empirically determined. The main criterion used was to set parameters such that the results were very similar to the ones obtained in Carroll et al. ([1]). We tried to use the same parameters presented in that article ($w_c = 1$, $w_s = 12$, $w_l = 1000$) but they did not work well in our case. One explanation for that is that the

Figure 2.35: Left: The minimizer of E_o. Energy value $E_o = 0.0609$. Right: The minimizer of E_d. Energy value $E_d = 0.0518$.

Figure 2.36: Left: The minimizer of E_o. Energy value $E_o = 0.0609$. Right: The minimizer of E_d. Energy value $E_d = 0.0518$.

Figure 2.37: Result for the final iteration. Comparing with figure 2.36 (left) we see that the visual convergence was already reached. Energy value $E_o = 0.0609$.

authors do not consider the terms $\Delta\lambda$ and $\Delta\phi$ used to discretize the partial derivatives in energies E_s and E_c. This choice can become a problem if $\Delta\lambda \neq \Delta\phi$, thus we decided to use such terms to have more general discretized partial derivatives.

Other explanation for this difference of weights is that the authors of [1] do not provide implementation details of their system. Thus, slight differences with respect to our implementation may exist.

But the most important thing about the weights we chose is that *all results in this thesis were generated with a fixed set of weights*: $w_c = 0.4$, $w_s = 0.05$ and $w_l = 1000$.

Chapter 3

Results

This chapter is devoted to show and explain many results produced by the method described in this chapter and in the previous one. All results were produced using the application software explained in Appendix A.

We first show four examples for which we consider the method was successful. We compare each one to the three standard projections presented in section 1.3 and to the perspereographic and recti-perspective projections, presented in section 1.4. For both these projections, we chose parameters such that the result was the best possible.

We give the following information about each example:

• **Field of View:** The field of view $S \subseteq \mathbb{S}^2$ chosen by the user to be projected. It is always a rectangular subset of the equirectangular domain.

• **Number of vertices:** The number of vertices used to discretize $S \subseteq \mathbb{S}^2$, according to the discretization explained in section 2.3.

• **Number of double iterations:** Number of double iterations necessary to reach visual convergence, as explained in section 2.8.4.

• **Final energy:** Energy obtained after the final iteration (section 2.8.4).

• **Time to construct the matrices:** Time necessary to construct the matrices C and S (sections 2.4 and 2.6) in a Intel Core 2 Quad Q8400 2.66 Ghz, using Matlab Version 7.6.0.324 (R2008a). All times in this section were obtained in the same computer.

• **Time to perform the optimizations:** Time required to perform all the iterations detailed in section 2.8.4.

• **Time to generate the final result:** After a final solution $\mathbf{x}$ is obtained, we turn it into an image, using bilinear interpolation. Details are given in section A.2.

In addition, for each example, we make specific comments emphasizing what properties the example illustrates. We also show an example comparing the result of this method with the result produced by [7], method that was explained in section 1.5.3.

To finish this chapter, we show some results produced by the method that are not as desired. For each example, we explain why the result showed an unpleasant behavior. We also provide a qualitative discussion about the results.

3.1 Result 1

- **Source image:** "Britomart in 360", by Flickr user Craigsydnz;
- **Field of view:** 220 degree longitude/ 140 degree latitude;
- **Number of vertices:** 58,479 vertices;
- **Number of double iterations:** 4;
- **Final energy:** $E_o = 9.9924 \cdot 10^{-5}$;
- **Time to construct the matrices:** 4 seconds;
- **Time to perform the optimizations:** 58 seconds;
- **Time to generate the final result:** 10 seconds.

Input image and marked lines

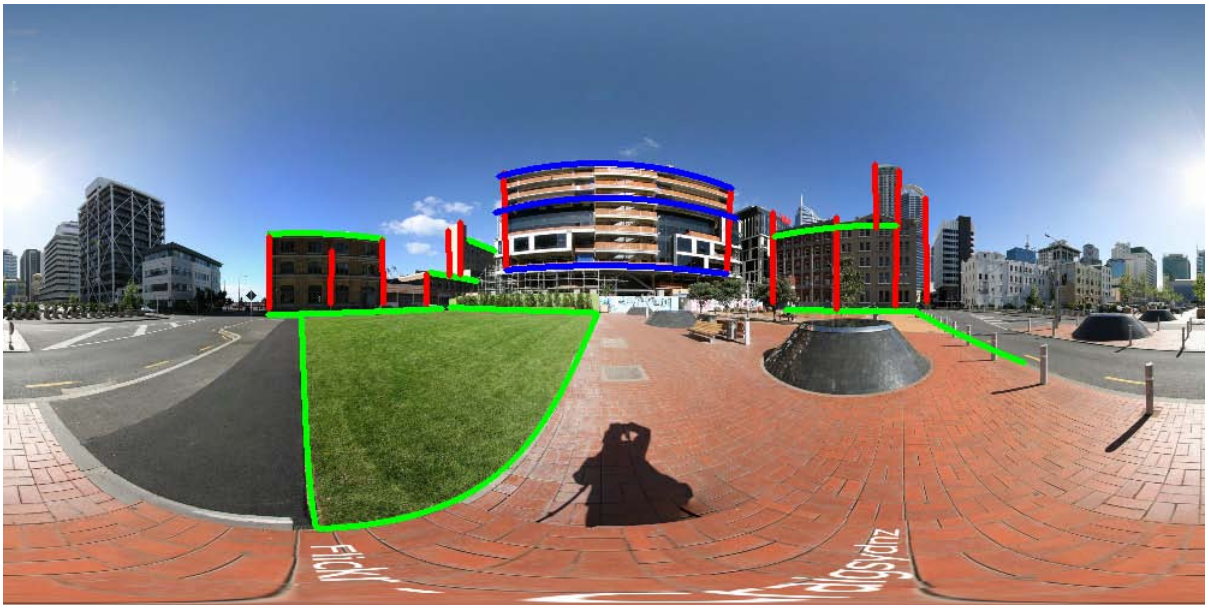

Standard projections: perspective, stereographic and Mercator

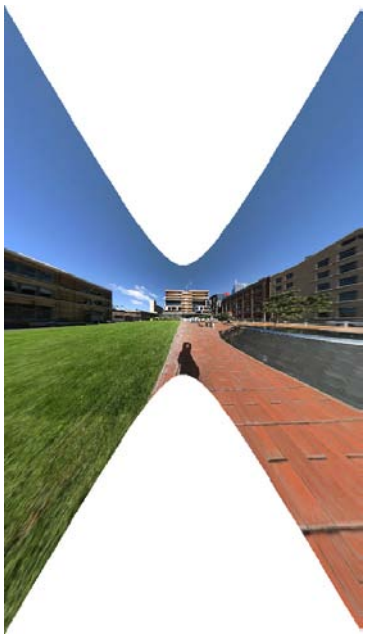

Modified standard projections: perspereographic (for $K = 0.5$) and recti-perspective ($\alpha = 2.5$, $\beta = 0.9$)

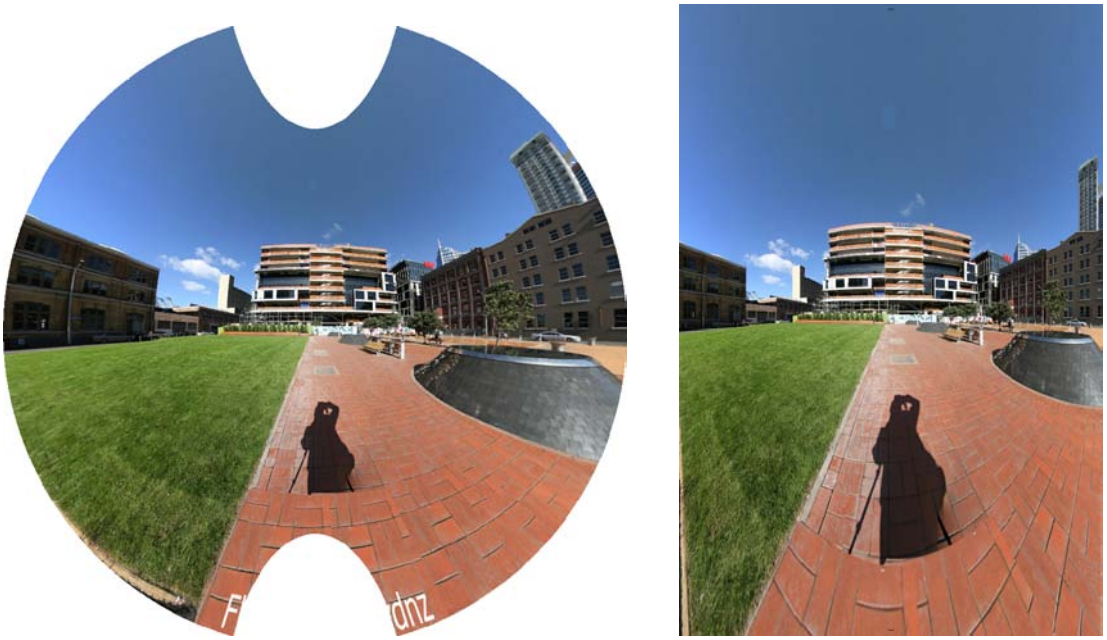

Result of the method (uncropped)

Result of the method (cropped)

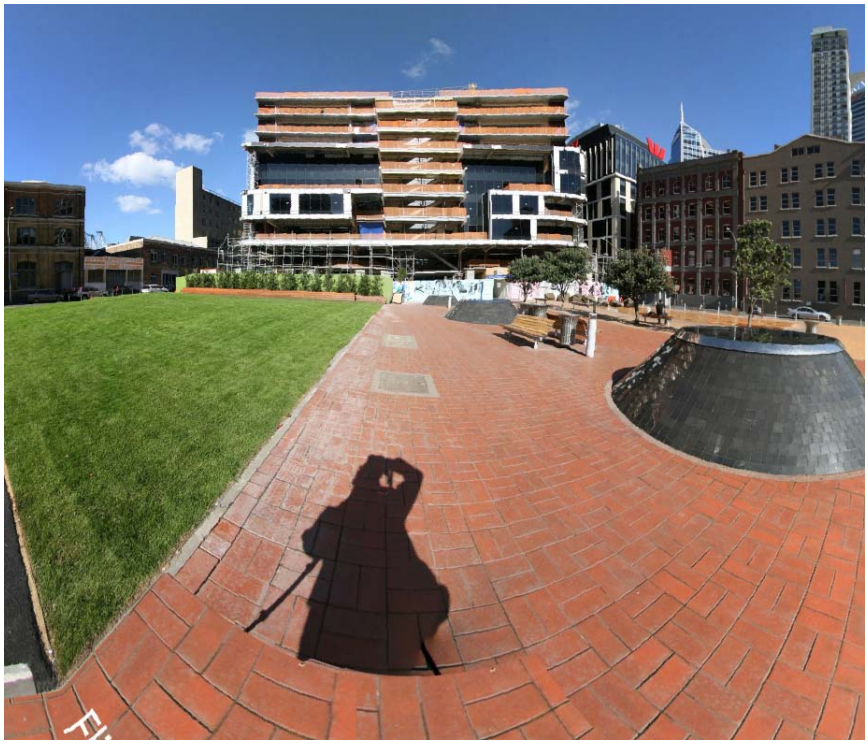

• **Comments for this example:** The method took about one minute long to produce the result, which is average for the method. As expected, the step that took longer was the optimizations and alternations between energies.

All the marked lines are straight, according to the orientation specified by the user: for example the side buildings are all vertical and the front building is horizontal. In addition, all the shapes are well preserved: no stretching is evident. All these properties make the result produced by the method better than all standard and modified projections.

One problem of the final result is the highly detailed floor. Since the user did not mark any straight lines on it, it looked curved in the final result. This will be a common problem: the user usually does not mark lines on the ground and, if she does, it will take too long to mark all the lines.

3.2 Result 2

• **Source image:** "Saint-Guénolé Church of Batz-Surmer Equirectangular 360º", by Flickr user Vincent Montibus;
• **Field of view:** 210 degree longitude/ 140 degree latitude;
• **Number of vertices:** 55,970 vertices;
• **Number of double iterations:** 6;
• **Final energy:** $E_o = 4.9531 \cdot 10^{-5}$;
• **Time to construct the matrices:** 17 seconds;
• **Time to perform the optimizations:** 124 seconds;
• **Time to generate the final result:** 10 seconds.

Input image and marked lines

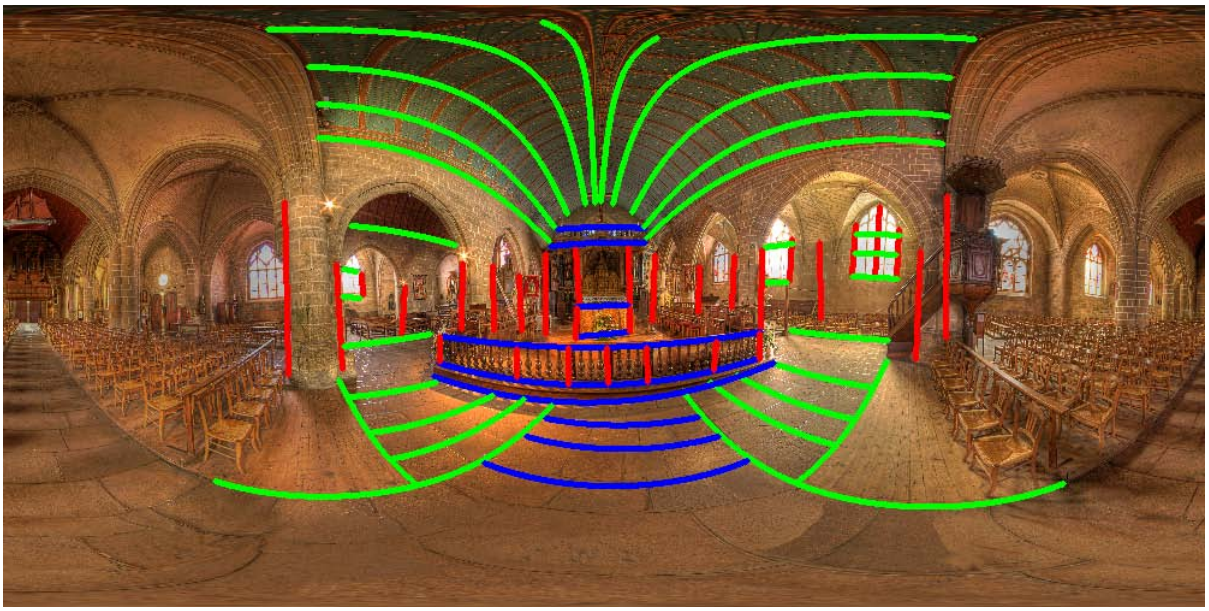

Standard projections: perspective, stereographic and Mercator

Modified standard projections: perspereographic (for $K = 0.6$) and recti-perspective ($\alpha = 2$, $\beta = 0.6$)

Result of the method (uncropped)

Result of the method (cropped)

• **Comments for this example:** This example illustrates that, even if many lines are marked on the input image, the method returns a good result. Sixty-nine lines were marked and covered a good part of the field of view that would be projected, and this fact was well handled.

Because of the quantity of green lines, more double iterations were needed to reach visual convergence. Thus, the method took longer than two minutes to obtain visual convergence.

3.3 Result 3

- **Source image:** "*La Caverne Aux Livre*", by Flickr user Gadl;
- **Field of view:** 150 degree longitude/ 140 degree latitude;
- **Number of vertices:** 39,758 vertices;
- **Number of double iterations:** 3;
- **Final energy:** $E_o = 2.8807 \cdot 10^{-4}$;
- **Time to construct the matrices:** 4 seconds;
- **Time to perform the optimizations:** 38 seconds;
- **Time to generate the final result:** 4 seconds.

Input image and marked lines

Detected faces

Standard projections: perspective, stereographic and Mercator

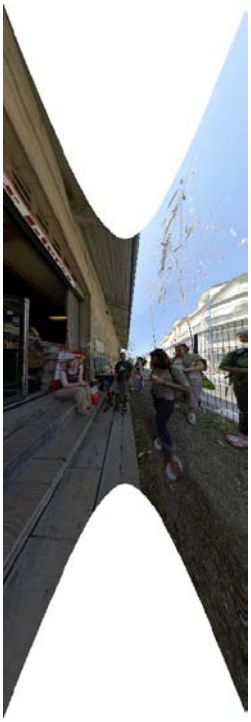

Modified standard projections: perspereographic (for $K = 0.4$) and recti-perspective ($\alpha = 1.7$, $\beta = 0.8$)

Result of the method (uncropped)

Result of the method (cropped)

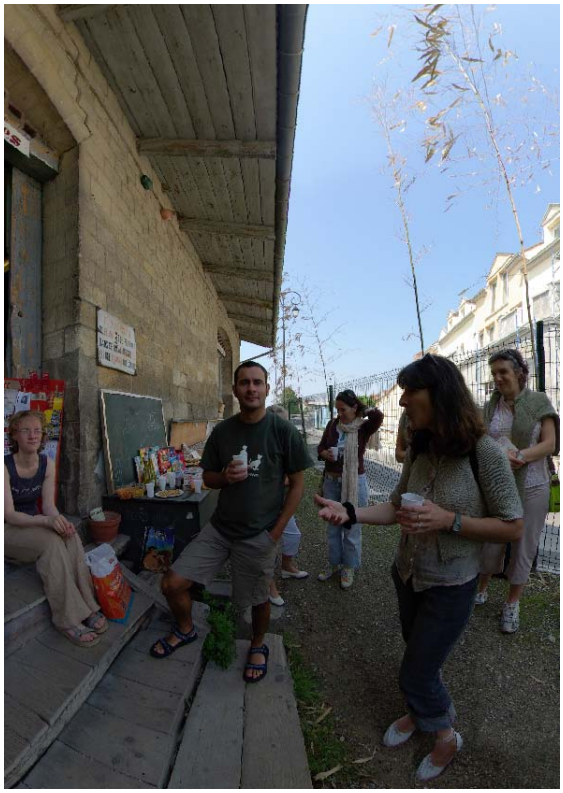

• **Comments for this example:** This example shows that the face detection process works well. All the frontal faces were detected by the method that will be explained in section B.1.

The face detection helped to preserve the shapes of the faces of the man in the center and of the woman in the left of the result. Their faces would be more stretched without the face detection, since many lines are passing near them.

3.4 Result 4

- **Source image:** "*Entrée du Parc Floral de Paris*", by Flickr user Gadl;
- **Field of view:** 360 degree longitude/ 180 degree latitude;
- **Number of vertices:** 78,804 vertices;
- **Number of double iterations:** 3;
- **Final energy:** $E_o = 0.0553$;
- **Time to construct the matrices:** 3 seconds;
- **Time to perform the optimizations:** 51 seconds;
- **Time to generate the final result:** 14 seconds.

Input image and marked lines

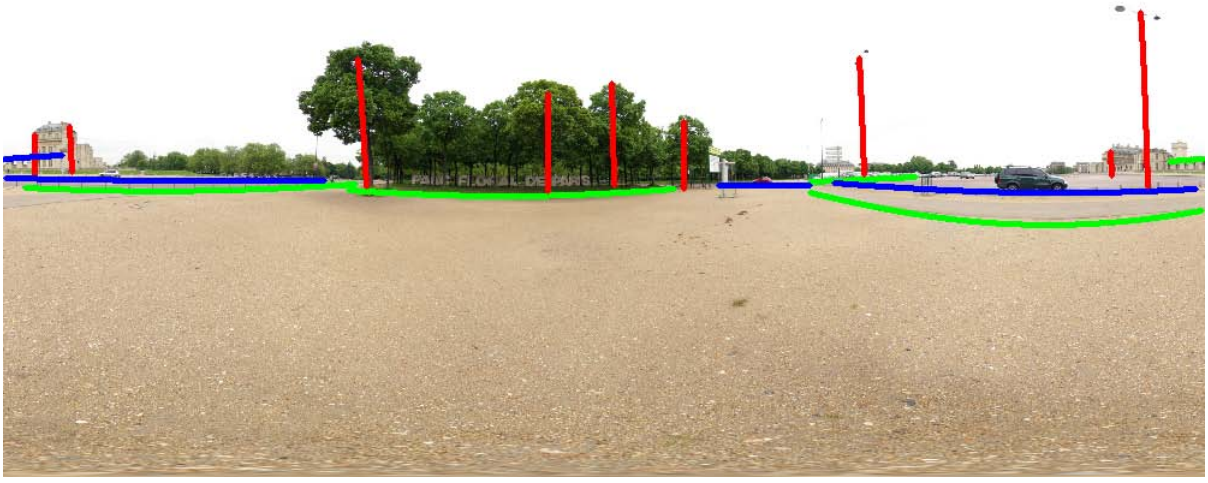

Standard projections: perspective, stereographic and Mercator

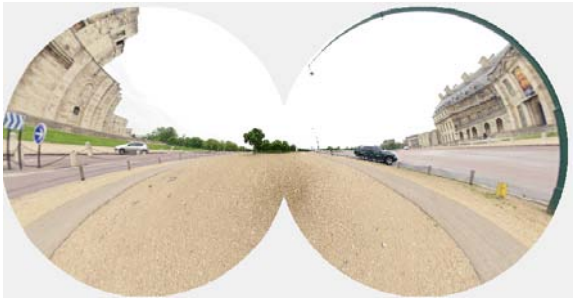

Modified standard projections: perspereographic (for $K = 1$) and recti-perspective ($\alpha = 50$, $\beta = 0.7$)

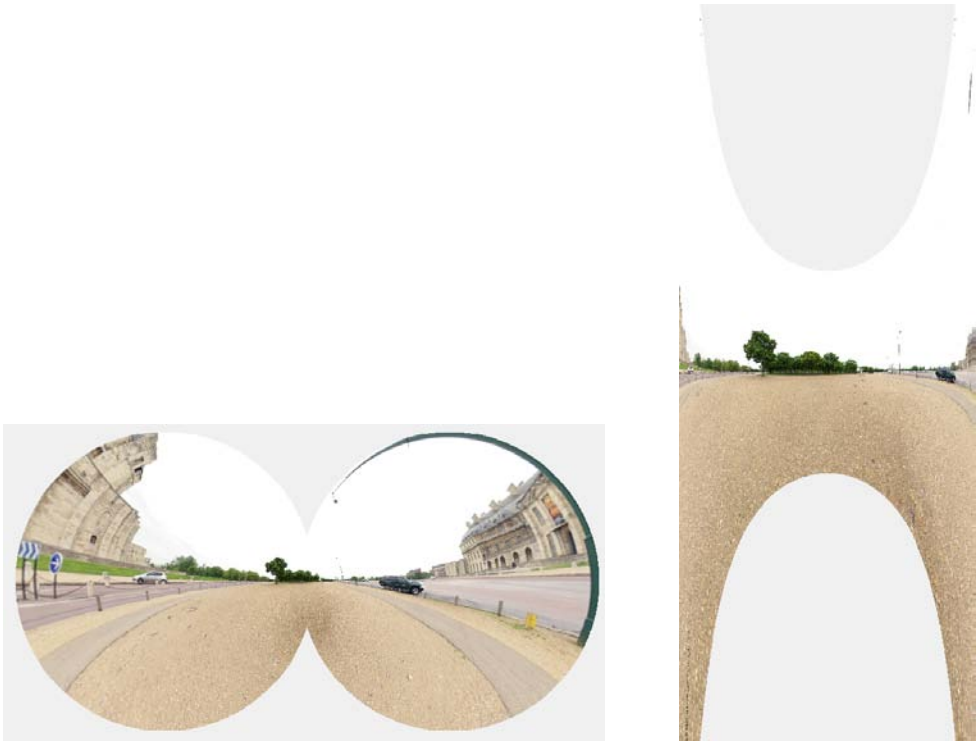

Result of the method (uncropped)

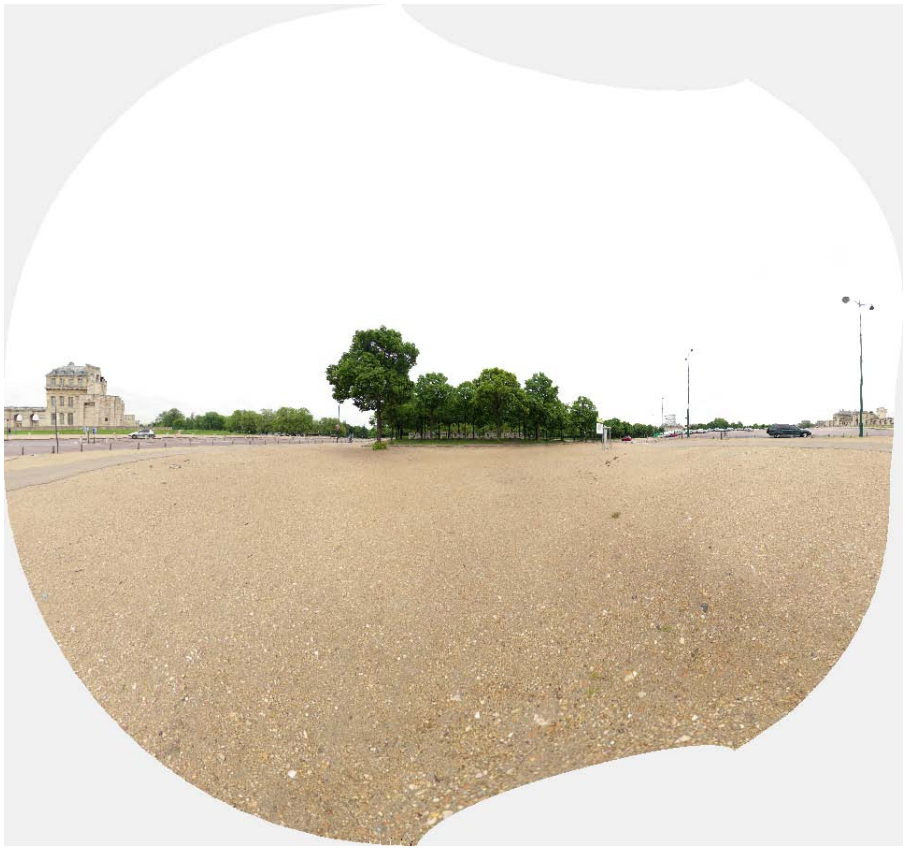

Result of the method (cropped)

• **Comments for this example:** This example shows that the method is applicable for wide fields of view, even the entire viewing sphere. The standard and modified projections have the problem of not being defined for such FOVs or infinity stretching. For example, the Mercator projection for this example was obtained by projecting a subset of the viewing sphere, actually 160 degree latitude, since the projection stretches to infinity when $\phi \rightarrow \pm\frac{\pi}{2}$.

The possibility of projecting the entire viewing sphere allows the construction of a viewer of panoramas based on the method approached on this thesis. The method would return the solution vector $\mathbf{x}$ and the user would specify what FOV of the sphere she wants to see. Thus, the viewer would collect only the positions of the vertices of the chosen FOV, construct an image and display on the screen. Some topological problems could appear, since the borders of the final result are irregular. There would not be the possibility of looking all around the viewing sphere, for example.

3.5 Result 5

- **Source image:** "Posters", by Flickr user Simon S.;
- **Field of view:** 180 degree longitude/ 100 degree latitude;
- **Number of vertices:** 44,431 vertices;
- **Number of double iterations:** 3;
- **Final energy:** $E_o = 4.0658 \cdot 10^{-5}$;
- **Time to construct the matrices:** 4 seconds;
- **Time to perform the optimizations:** 43 seconds;
- **Time to generate the final result:** 4 seconds.

Input image and marked lines

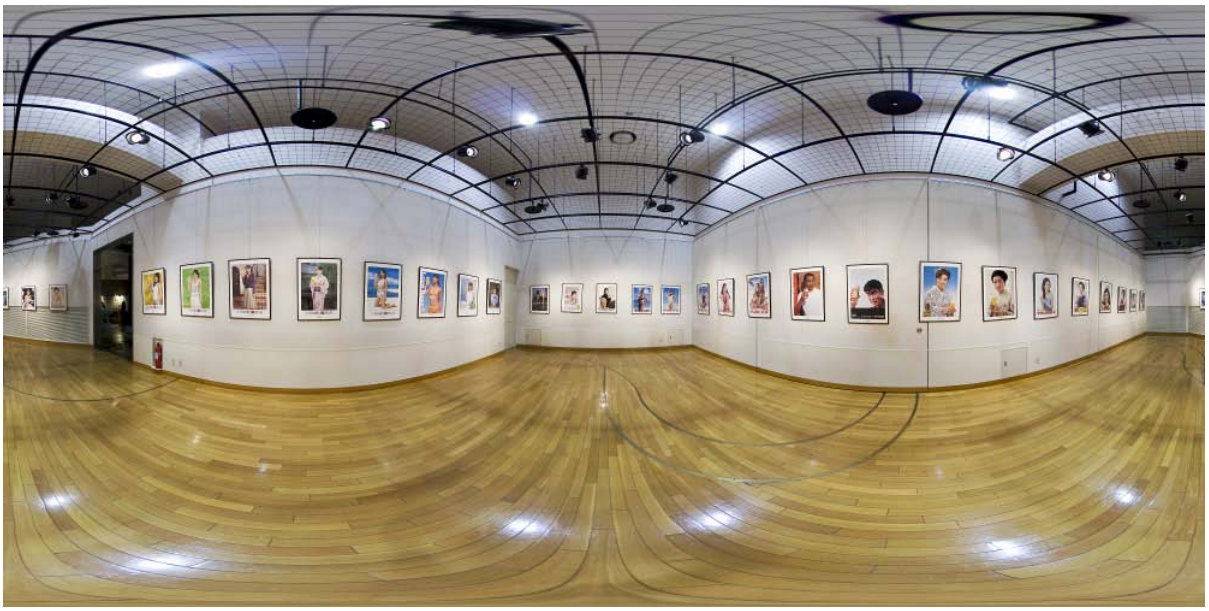

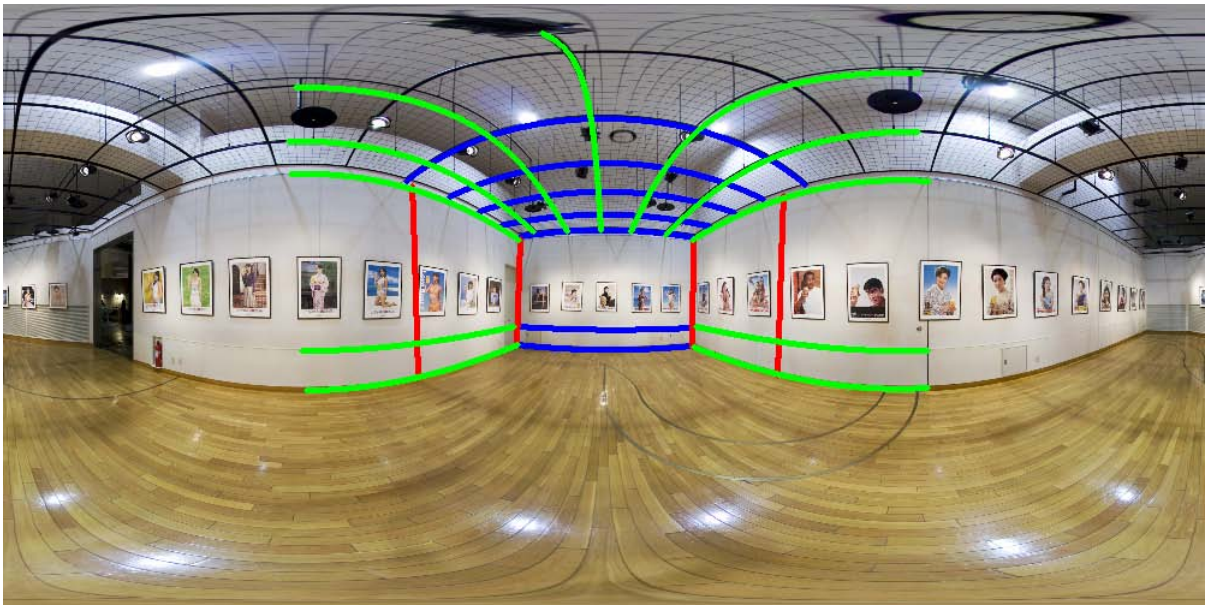

Result of the method described in [7] (cropped)

Result of the method described in this thesis (cropped)

• **Comments for this example:** The method in [7] breaks the lines on the ceiling. This is not a problem for the method described in this thesis, as can be seen above.

3.6 Failure cases

The first failure case we show is when a scene is covered by multiple parallel lines that cover near 180^o. An example of such scene is shown in figure 3.1, where long horizontal lines are present in the scene. Straightening such lines unavoidably causes distortions in the region that is between them. In figure 3.2 we show the final result where the train is distorted.

Figure 3.1: A scene with two horizontal lines covering near 180^o of the equirectangular image. Source image: "Express Shirasagi", by Flickr user Vitroid.

Figure 3.2: Final result. Observe how the train is distorted.

Another failure case happens when the user forgets to mark important lines in the scene and/or forgets to specify some important orientation. We show in figure 3.3 the same example shown in result 5, but with other lines marked. As can be seen in figure 3.4 the result produced by the method is very undesirable.

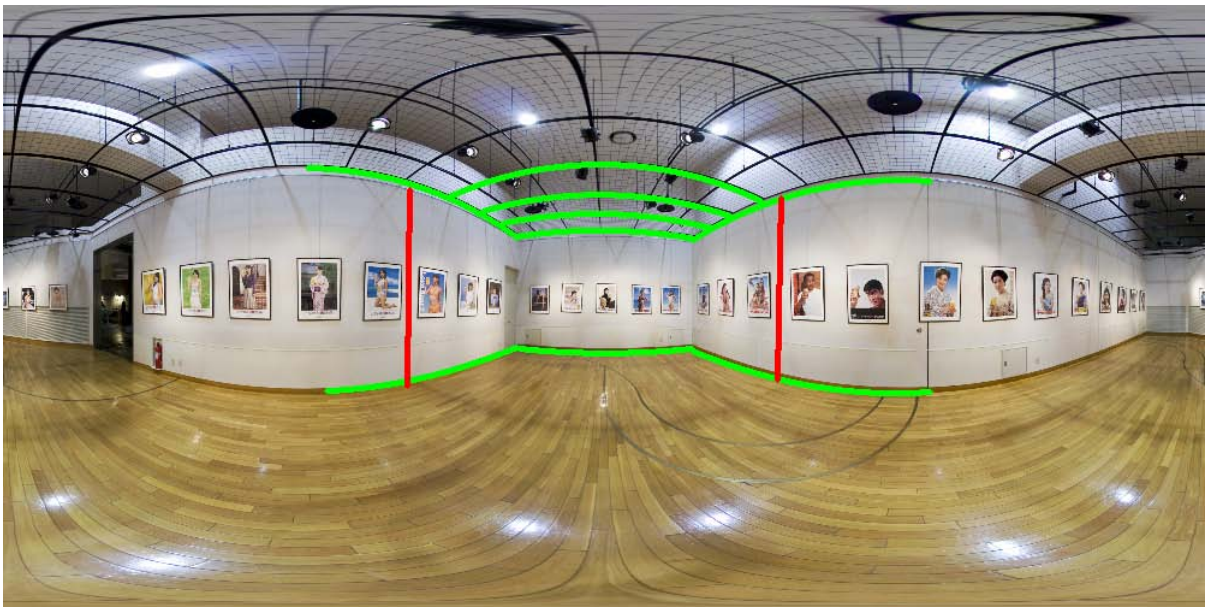

Figure 3.3: The same example as in result 5, but with other lines specified.

Figure 3.4: Final undesirable result.

The method shows to be user dependent in some situations. It requires precision of the user to specify lines. The semiautomatic detection of lines described in section B.2 may help the user in this task.

3.7 Result Discussion

The results shown in the last section prove the precision of the method studied in this thesis. In all the cases where the user marked correctly the important lines in the scene, the method returned a perceptually great result.

In this section, we finish the discussion about the results presenting some properties that all of them share.

The first one is that the projection is very uniform far from the lines. We plot in figure 3.5 results 2 and 3 together with a base mesh (which is *not* the same mesh used to obtain the result, it is a coarser one).

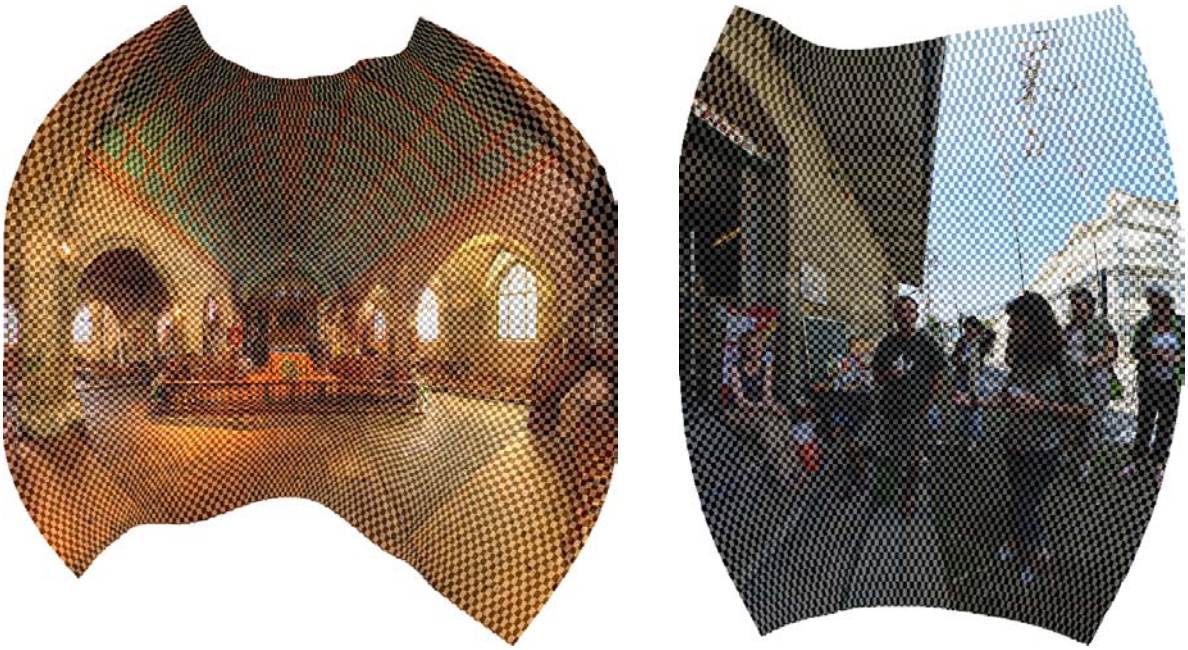

Figure 3.5: The projection is more distorted near the line segments.

Another property that all the results share is that the final result never has null energy. Since we want a mapping with as least distortions as possible, mappings with null energy would be the ideal ones.

Such behavior has a clear explanation: the smoothness, conformality and line constraints can not be satisfied at the same time. We show, in particular, that the smoothness and conformality energy can not be null at the same time in the continuous context.

Remember from section 2.4 that a mapping $\mathbf{u} : \mathbb{S}^2 \to \mathbb{R}^2$ is conformal if

$$\frac{\partial u}{\partial \phi} = -\frac{1}{\cos\phi}\frac{\partial v}{\partial \lambda}, \ \frac{\partial v}{\partial \phi} = \frac{1}{\cos\phi}\frac{\partial u}{\partial \lambda},$$

and, from section 2.6, $\mathbf{u}$ is smooth if

$$\frac{\partial^2 u}{\partial \phi^2} = 0, \ \frac{\partial^2 v}{\partial \phi^2} = 0, \ \frac{\partial^2 u}{\partial \phi \partial \lambda} = 0, \ \frac{\partial^2 v}{\partial \phi \partial \lambda} = 0.$$

The following statement shows that the only mapping that satisfy the above six equations are the constant mappings:

Statement 3.1 *$\boldsymbol{u}: \mathbb{S}^2 \to \mathbb{R}^2$ is conformal and smooth $\Leftrightarrow$ $\boldsymbol{u}(\lambda, \phi) = (u_0, v_0)$, $\forall(\lambda, \phi)$.*

Proof: ($\Leftarrow$) Constant mappings have all derivatives equal to zero and the above six equations are trivially verified.
($\Rightarrow$) We use the above six equations to obtain expressions for u and v:
- $\dfrac{\partial^2 u}{\partial\phi\partial\lambda} = 0 \Rightarrow \dfrac{\partial u}{\partial\phi} = F_1(\phi) \Rightarrow u = \displaystyle\int F_1(\phi)d\phi + F_2(\lambda)$, for some functions F_1 and F_2.
- $\dfrac{\partial^2 u}{\partial\phi^2} = 0 \Rightarrow \dfrac{\partial^2}{\partial\phi^2}\left[\displaystyle\int F_1(\phi)d\phi + F_2(\lambda)\right] = 0 \Rightarrow \dfrac{\partial}{\partial\phi}\left[\dfrac{\partial}{\partial\phi}\displaystyle\int F_1(\phi)d\phi + \dfrac{\partial}{\partial\phi}F_2(\lambda)\right] = 0 \Rightarrow$

$F_1'(\phi) = 0 \Rightarrow F_1(\phi) = K_1 \Rightarrow u = \displaystyle\int K_1 d\phi + F_2(\lambda) \Rightarrow u = K_1\phi + F_2(\lambda)$, for some constant K_1. Thus, we have the following expression for u:

$$u = K_1\phi + F_2(\lambda).$$

Analogously, using the equations $\dfrac{\partial^2 v}{\partial\phi^2} = 0$ and $\dfrac{\partial^2 v}{\partial\phi\partial\lambda}$, one obtains the following expression for v:

$$v = K_2\phi + F_4(\lambda),$$

for some constant K_2 and some function F_4.
Now, considering the Cauchy-Riemann equations, we have:
- $\dfrac{\partial u}{\partial\phi} = -\dfrac{\partial v}{\partial\lambda}\dfrac{1}{\cos\phi} \Rightarrow K_1 = -\dfrac{F_4'(\lambda)}{\cos\phi} \Rightarrow K_1\cos\phi = -F_4'(\lambda)$. Since $\cos(\phi)$ only depends on ϕ and $-F_4'(\lambda)$ depends only on λ, the last equation implies $K_1 = F_4'(\lambda) = 0$. Hence, $K_1 = 0$, $F_4 = K_3$ and $u = F_2(\lambda)$ and $v = K_2\phi + K_3$, for some constant K_3.
- $\dfrac{\partial v}{\partial\phi} = \dfrac{\partial u}{\partial\lambda}\dfrac{1}{\cos\phi} \Rightarrow K_2 = \dfrac{F_2'(\lambda)}{\cos\phi} \Rightarrow F_2'(\lambda) = K_2\cos(\phi) \Rightarrow K_2 = 0, F_2 = K_4$, for some constant K_4.

Thus, $u = K_4$ and $v = K_3$, which proves that $\mathbf{u} = (u, v)$ is a constant mapping.

■

We have proved that the only mappings that are smooth and conformal in the continuous case are the constant ones. We extend this result for the discrete case assuming that the discretization is fine enough such that the result holds.

Since our optimization method returns a nonconstant solution (which is a desirable property), we conclude that such solution must have nonzero energy, since the total energy ia a sum of conformality, smoothness and line energies.

To finish the discussion about the results, we argue about the time of computation of them. We used Matlab implementations that will be discussed in A.2.3 to compute the results. Despite of being very practical, Matlab tends to be slower than using Linear Algebra Routines in C or C++. A future work would be to convert our implementation to C++.

But even in the Matlab context, we think the result could be produced faster. It is taking longer than desired to alternate between energies, i.e., to compute the normal

vectors $\mathbf{n}$ and the projections s_{ij} as described in section 2.8.4. Also, in order to produce the final result with bilinear interpolation, it is taking longer than expected and we think this procedure could be improved. We leave these both tasks to future work.

Despite of these procedures that have to be improved, we think that about one minute to produce the results is a satisfactory time.

Chapter 4

Panoramic Videos

In this chapter we study the problem of producing perceptually good *panoramic videos*. A *panoramic video* is a video where each frame is a panoramic image. In order to produce these videos, we join the theory developed in previous chapters to novel ideas that model *temporal coherence* in wide-angle videos.

It is important to emphasize that this chapter is the beginning of a research that probably will last some years. In this chapter, we model the panoramic video problem, discuss cases and desirable properties, suggest a solution for one of the cases and point directions to solve the other cases.

As far as we know, the problem that we address in this chapter was not solved yet. Previous works as [17], [18], [19] and [20] produce from a temporally variable viewing sphere (which we call in this chapter *temporal viewing sphere*) a video in which each frame has a narrow FOV, for immersion purposes.

The work that has closest goals to the ones we have is [21]. They produce a video with wide-angle frames from a set of common photographs, by transferring textures between frames in a coherent way. Our method takes as input a temporal viewing sphere that represents much better an entire scene, since it is not limited to some field of view. Also, we consider geometric distortions in wide-angle videos, which are not considered in [21]. Furthermore, their method is very restricted to scenes with particular structures. We develop a more general method.

4.1 Overview

We start the study of the panoramic video problem by separating it in three cases. This separation is done in section 4.2 and considers if viewpoint, field of view and objects are stationary or moving through time.

In section 4.3 we discuss perceptual properties that we believe to be the most important in wide-angle videos. Our discussion is not based on any perceptual study, it takes into account only intuitive ideas.

Sections 4.4 and 4.5 are devoted to model the general case, through the mathematical definition of temporal viewing sphere, panoramic videos and transition functions.

In section 4.6 we suggest a solution for the first case of panoramic videos, when the viewpoint and the FOV are stationary and there are moving objects in the scene. Some first results are shown.

We finish the chapter by briefly discussing solutions for the other cases and making some concluding remarks.

4.2 The three cases

We separate the panoramic video in three categories, according to the movement of the viewpoint (VP), the field of view and the objects in the scene. The general case is a combination of theses three cases. This separation was done because we think it is easier to solve first simpler cases in order to get the general solution. We list below the three cases:

• **Case 1 - Stationary VP, stationary FOV and moving objects:** In this case, the viewpoint and the field of view (the rectangle $[\alpha_1, \alpha_2] \times [\beta_1, \beta_2] \subseteq [-\pi, \pi] \times [-\frac{\pi}{2}, \frac{\pi}{2}]$) that will be projected do not change across time. Only objects are moving. For this case, it is expected that the background is always the same and the objects move in a temporally coherent way. This coherence will be explained further.

• **Case 2 - Stationary VP, moving FOV and stationary objects:** In this case, the viewpoint and all the scene are stationary. The only thing that is different through time is the rectangle $[\alpha_1, \alpha_2] \times [\beta_1, \beta_2]$. This case may be seen as panoramic visualizer of scenes, where one could navigate through a scene with panoramic views of it.

• **Case 3 - Moving VP:** This case is the most difficult, since everything in the scene is changing through time, even still objects. The separation between scene and objects is harder in this case and so is the modeling of temporal coherence.

Table 4.1 illustrates the separation we just did.

4.3 Desirable Properties

We divide the requirements for a perceptually good panoramic video in two categories: *per frame requirements* and *temporal requirements*.

Stationary VP		
	Stationary objects	Moving objects
Stationary FOV	**Trivial case**	**Case 1**
Moving FOV	**Case 2**	**Cases 1 + 2**
Moving VP		
Case 3		

Table 4.1: Separation of the panoramic video problem.

The per frame requirements are the properties that each frame must satisfy, independent of the other frames. We propose the following two requirements:
1) Each frame must be a good panoramic image: Undesirable distortions in individual frames would be noticeable in videos, especially if these distortions were transported to other frames using temporal coherence. A state-of-the-art method for computing panoramic images turns out to be necessary, and we use the method discussed in chapters 2 and 3.
2) Moving objects must be well preserved: The regions of a video to which one most pay attention when watching are the moving objects. Thus, conformality and smoothness should be increased in such regions, when there are moving objects in the scene.

The temporal requirements impose that objects and scene change in a temporally coherent manner. Thus, they are requirement to be satisfied by the frames depending on other frames. We make two temporal requirements:
3) Temporal coherence of the scene: This is an imposition made for all points that are being projected. It depends on the movement of the viewpoint. For example, if the VP and the FOV are stationary, the background should be the same through time.
4) Temporal coherence of the objects: This imposition is made over moving object regions. It tells us that size and orientation of objects should only change if such properties change in the temporal viewing sphere. For example, if an object becomes twice larger from on time to another on the temporal viewing sphere, it should be twice larger from one frame to another in the panoramic video. An important observation is that the object should not have the same size and orientation through all panoramic video. If an object is moving away from the viewpoint its size should not be preserved, it should be smaller from one time to another. That is the reason why me model this property depending on the temporal viewing sphere.

The mathematical modeling of requirements 3 and 4 is made with definition of *transition functions*, definition that will be stated in section 4.5.

4.4 The Temporal Viewing Sphere and Problem Statement

In this section, we mathematically define the concept of *temporal viewing sphere*. Temporal viewing spheres will be the input for our methods and contains the information of a scene that varies through time. We also state the *panoramic video problem*. All this section is an immediate extension of the definitions we gave for the panoramic image problem.

Let $[0, t_0]$ be a time interval and consider the function

$$\begin{array}{rccl} \mathbf{R}: & [-\pi,\pi]\times\left[-\frac{\pi}{2},\frac{\pi}{2}\right]\times[0,t_0] & \rightarrow & \mathbb{R}^4 \\ & (\lambda,\phi,t) & \mapsto & (\cos(\lambda)\cos(\phi),\sin(\lambda)\cos(\phi),\sin(\phi),t) \end{array}$$

We call the image of $\mathbf{R}$ the *temporal viewing sphere*. It is just a set of viewing spheres with one more coordinate (t) that tells which time they are representing. We denote the temporal viewing sphere by $\mathbb{TS}^2$. We give in figure 4.1 an illustration of the concept we have just defined:

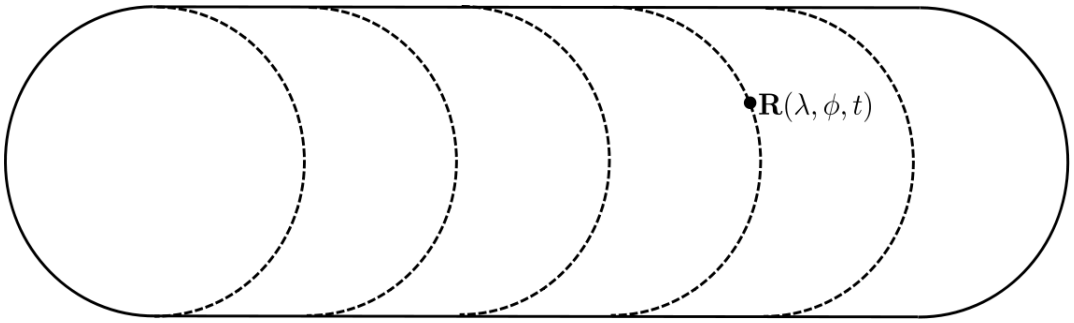

Figure 4.1: An illustration of the temporal viewing sphere. The variation of the fourth coordinate is represented by the variation of position of the center of each sphere.

We represent the temporal viewing sphere by its corresponding *equirectangular video*. For each $t \in [0, t_0]$ we associate a frame in the equirectangular video containing the equirectangular image for this time. Thus, the equirectangular video is just a set of equirectangular images representing the set $[-\pi,\pi]\times\left[-\frac{\pi}{2},\frac{\pi}{2}\right]\times\{t\}$, for each $t \in [0, t_0]$.

There are some special devices that capture equirectangular videos. The one we used was *Ladybug2*. For more information about this and other cameras, one can see [9].

In figures 4.2 and 4.3 we show some frames of the equirectangular video we captured using this camera.

With the definition of temporal viewing sphere, we now can state the panoramic video problem. We look for a function

$$\begin{array}{rccl} \mathbf{U}: & S\subseteq\mathbb{TS}^2 & \rightarrow & \mathbb{R}^3 \\ & (\lambda,\phi,t) & \mapsto & (U(\lambda,\phi,t),V(\lambda,\phi,t),t) \end{array},$$

with desirable properties.

Figure 4.2: First frame of the video we use in this chapter. The camera we used does not capture the lower part of the entire field of view, i.e., the points with latitude near to $-\frac{\pi}{2}$.

Figure 4.3: Last frame of the video we use in this chapter.

We now consider tangent vectors in $\mathbb{TS}^2$ and in $\mathbf{U}(\mathbb{TS}^2)$. Let $p = (\lambda, \phi, t) \in (-\pi, \pi) \times (-\frac{\pi}{2}, \frac{\pi}{2}) \times (0, t_0)$. A tangent basis for $T_p\mathbb{TS}^2$ is:

- $\mathbf{R}_\lambda = \dfrac{\partial \mathbf{R}}{\partial \lambda}(\lambda, \phi, t) = (-\sin(\lambda)\cos(\phi), \cos(\lambda)\cos(\phi), 0, 0)^T$;
- $\mathbf{R}_\phi = \dfrac{\partial \mathbf{R}}{\partial \phi}(\lambda, \phi, t) = (-\cos(\lambda)\sin(\phi), \sin(\lambda)\sin(\phi), 0, 0)^T$;
- $\mathbf{R}_t = \dfrac{\partial \mathbf{R}}{\partial t}(\lambda, \phi, t) = (0, 0, 0, 1)^T$.

The basis above is already orthogonal, but $\mathbf{R}_\lambda$ is not unitary. An orthonormal tangent basis for $T_p\mathbb{TS}^2$ is:

$$\widehat{\mathbf{R}_\lambda} = \frac{1}{\cos\phi}, \ \widehat{\mathbf{R}_\phi} = \mathbf{R}_\phi \text{ and } \widehat{\mathbf{R}_t} = \mathbf{R}_t.$$

Given a panoramic video function $\mathbf{U}$, its derivative $d\mathbf{U}_p$ written in the basis $\{\mathbf{R}_\lambda, \mathbf{R}_\phi, \mathbf{R}_t\}$

is represented by the following matrix:

$$(d\mathbf{U}_p)_{\{\mathbf{R}_\lambda,\mathbf{R}_\phi,\mathbf{R}_t\}} = \begin{pmatrix} \frac{\partial U}{\partial \lambda}(\lambda,\phi,t) & \frac{\partial U}{\partial \phi}(\lambda,\phi,t) & \frac{\partial U}{\partial t}(\lambda,\phi,t) \\ \frac{\partial V}{\partial \lambda}(\lambda,\phi,t) & \frac{\partial V}{\partial \phi}(\lambda,\phi,t) & \frac{\partial V}{\partial t}(\lambda,\phi,t) \\ \frac{\partial t}{\partial \lambda}(\lambda,\phi,t) & \frac{\partial t}{\partial \phi}(\lambda,\phi,t) & \frac{\partial t}{\partial t}(\lambda,\phi,t) \end{pmatrix} = \begin{pmatrix} \frac{\partial U}{\partial \lambda} & \frac{\partial U}{\partial \phi} & \frac{\partial U}{\partial t} \\ \frac{\partial V}{\partial \lambda} & \frac{\partial V}{\partial \phi} & \frac{\partial V}{\partial t} \\ 0 & 0 & 1 \end{pmatrix}.$$

We define the differential north, east and time vectors (respectively $\mathbf{H}$, $\mathbf{K}$ and $\mathbf{T}$) as the image of $d\mathbf{U}_p$ in the vectors $\widehat{\mathbf{R}_\phi}$, $\widehat{\mathbf{R}_\lambda}$ and $\widehat{\mathbf{R}_t}$:

$$\mathbf{H} = d\mathbf{U}_p(\widehat{\mathbf{R}_\phi}) = (d\mathbf{U}_p)_{\{\mathbf{R}_\lambda,\mathbf{R}_\phi,\mathbf{R}_t\}} \begin{pmatrix} 0 \\ 1 \\ 0 \end{pmatrix} \Rightarrow \mathbf{H}(\lambda,\phi,t) = \begin{pmatrix} \frac{\partial U}{\partial \phi}(\lambda,\phi,t) \\ \frac{\partial V}{\partial \phi}(\lambda,\phi,t) \\ 0 \end{pmatrix},$$

$$\mathbf{K} = d\mathbf{U}_p(\widehat{\mathbf{R}_\lambda}) = (d\mathbf{U}_p)_{\{\mathbf{R}_\lambda,\mathbf{R}_\phi,\mathbf{R}_t\}} \begin{pmatrix} \frac{1}{\cos\phi} \\ 0 \\ 0 \end{pmatrix} \Rightarrow \mathbf{K}(\lambda,\phi,t) = \frac{1}{\cos\phi} \begin{pmatrix} \frac{\partial U}{\partial \lambda}(\lambda,\phi,t) \\ \frac{\partial V}{\partial \lambda}(\lambda,\phi,t) \\ 0 \end{pmatrix},$$

$$\mathbf{T} = d\mathbf{U}_p(\widehat{\mathbf{R}_t}) = (d\mathbf{U}_p)_{\{\mathbf{R}_\lambda,\mathbf{R}_\phi,\mathbf{R}_t\}} \begin{pmatrix} 0 \\ 0 \\ 1 \end{pmatrix} \Rightarrow \mathbf{T}(\lambda,\phi,t) = \begin{pmatrix} \frac{\partial U}{\partial t}(\lambda,\phi,t) \\ \frac{\partial V}{\partial t}(\lambda,\phi,t) \\ 1 \end{pmatrix}.$$

The three vectors we just defined tell the variation of the projection $\mathbf{U}$ considering all coordinates λ, ϕ and t. We illustrate in figure 4.4 the panoramic video projection $\mathbf{U}$ and the tangent vectors in $T_p\mathbb{TS}^2$ and in $\mathbf{U}(\mathbb{TS}^2)$.

4.5 Transition Functions

In order to model temporal coherence, we define transition functions between points in different times on the temporal viewing sphere.

In other words, given $t_1, t_2 \in [0, t_0]$, a *a transition function between* t_1 *and* t_2 is given by

$$\begin{array}{rccc} \varphi_{t_1,t_2}: & \mathbb{S}^2 \times \{t_1\} & \rightarrow & \mathbb{S}^2 \times \{t_2\} \\ & (\lambda,\phi,t_1) & \mapsto & (\lambda_{t_1,t_2}(\lambda,\phi,t_1), \phi_{t_1,t_2}(\lambda,\phi,t_1), t_2) \end{array}.$$

We illustrate the transition function concept in figure 4.5.

We make some comments on the definition above:

• A transition function defined on time t_1 may not be defined in the entire $\mathbb{S}^2 \times t_1$. The definition above may be extended to subsets $S \times t_1 \subseteq \mathbb{S}^2 \times t_1$.

• Given (λ, ϕ, t_0), if for all $t \in [0, t_0]$ there is a transition function $\varphi_{t_0,t}$ defined on (λ, ϕ, t_0), the set $\{\varphi_{t_0,t}(\lambda,\phi,t_0)\}_{t\in[0,t_0]}$ is the *orbit* of (λ, ϕ, t_0). Other dynamical properties could be derived from the definition of transition functions but they are not important now.

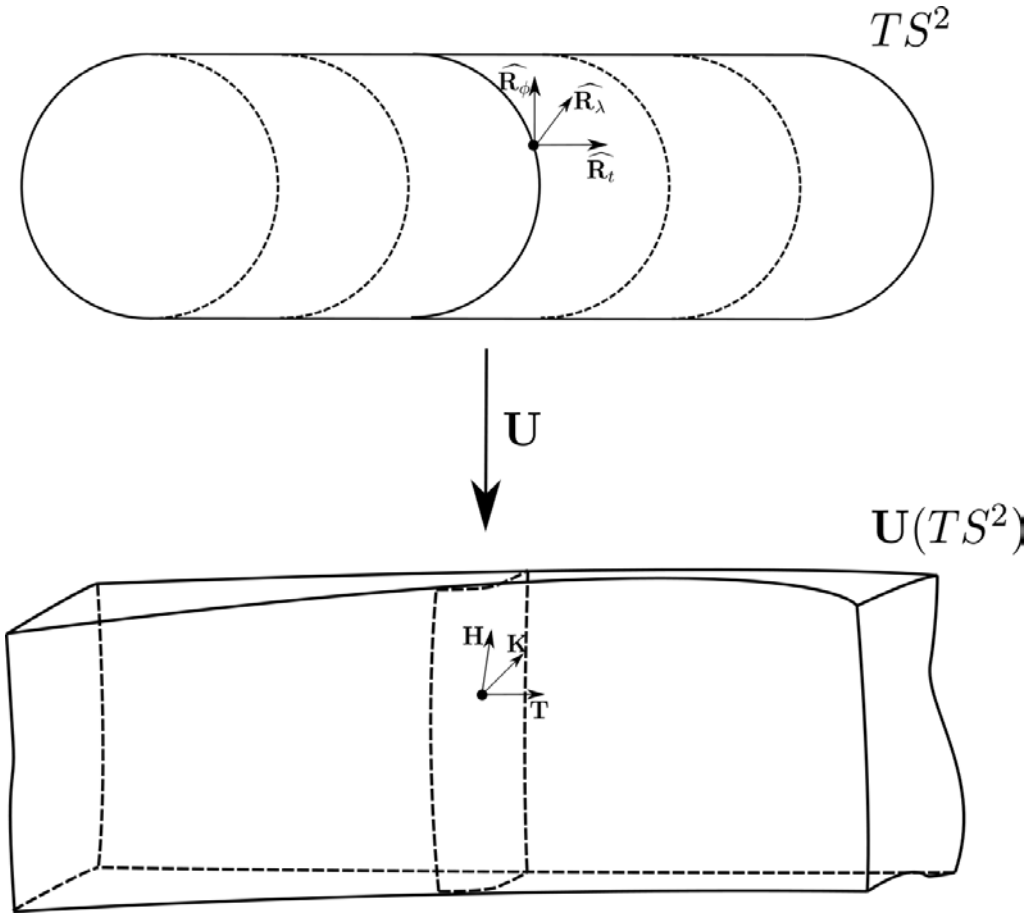

Figure 4.4: Projection **U**, tangent basis of the temporal viewing sphere and tangent basis of the final panoramic video.

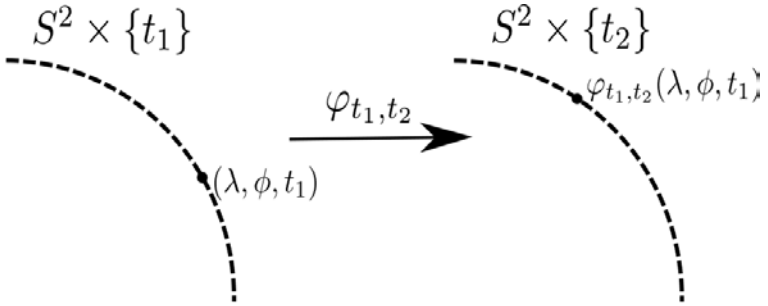

Figure 4.5: Transition function from time t_1 to time t_2.

• The transition functions consider occlusions: if a point (λ, ϕ, t) of an object is occluded in time $t + \Delta t$ then $\varphi_{t,t+\Delta t}$ is not defined at (λ, ϕ, t).

We consider two kinds of transition functions: the scene transition function (denoted by $\varphi^{sc}_{t_1,t_2}$) and the object transition functions (denoted by $\varphi^{ob}_{t_1,t_2}$).

$\varphi^{sc}_{t_1,t_2}$ is defined in the entire $\mathbb{S}^2 \times \{t_1\}$ and model the temporal coherence of all points that are being projected. It must depend on the movement of the viewpoint. For example, if the VP is stationary, we have

$$\varphi^{sc}_{t_1,t_2}(\lambda, \phi, t_1) = (\lambda, \phi, t_2),\ \forall (\lambda, \phi, t_1) \in \mathbb{S}^2 \times \{t_1\},$$

since all points in $\mathbb{S}^2 \times \{t_1\}$ are stationary (except for the moving objects).

$\varphi^{ob}_{t_1,t_2}$ is defined only in object regions and tells the correspondence of points of an object between different times. For example, if an object is translated by (λ_0, ϕ_0) in the equirectangular domain, the transition function for it will be

$$\varphi^{ob}_{t_1,t_2}(\lambda, \phi, t_1) = (\lambda + \lambda_0, \phi + \phi_0, t_2),\ \forall (\lambda, \phi, t_1) \in \text{ object at time } t_1.$$

4.6 Case 1 - Stationary VP, Stationary FOV and Moving Objects

In this section, we propose a solution for the 1st case of panoramic videos. This solution is strongly based on the solution we studied for images: we derive equations for temporal coherence, discretize the domain, obtain energy terms for the temporal coherence equations and compute a panoramic video using an optimization framework.

We simplify this case by assuming there is only one moving object in the scene, but our solution is easily extendable for n objects. Since the FOV is stationary, the part of the temporal viewing sphere that will be projected is a cube of the form $[\alpha_1, \alpha_2] \times [\beta_1, \beta_2] \times [0, t_0]$.

4.6.1 Temporal Coherence Equations

In this section, we obtain partial differential equations that model temporal coherence for case 1 of panoramic videos. We obtain these equations for the object in the scene (using the transition functions $\varphi^{ob}_{t_1,t_2}$) and extend them for the entire scene, using the transition functions $\varphi^{ob}_{t_1,t_2}$.

Let $S \times \{t_1\} \subseteq \mathbb{S}^2 \times \{t_1\}$ be the moving object in the scene at time t_1 and assume $\varphi^{ob}_{t_1,t_2}$ to be defined in $S \times \{t_1\}$. Let $(\lambda_1, \phi_1, t_1) \in S \times \{t_1\}$ and $(\lambda_2, \phi_2, t_2) = \varphi_{t_1,t_2}(\lambda_1, \phi_1, t_1)$.

The perceptual requirement that we make (property 4 in section 4.3) is that the object changes size and orientation according to such changes in the temporal viewing sphere. Consider a ball of radius $\varepsilon > 0$ around (λ_1, ϕ_1, t_1) in $S \times \{t_1\}$ and assume, with no loss of generality, that $B((\lambda_1, \phi_1, t_1), \varepsilon)$ is projected on a ball with radius $\delta > 0$ in $\mathbf{U}(\mathbb{TS}^2)$: $\mathbf{U}(B((\lambda_1, \phi_1, t_1), \varepsilon)) = B(\mathbf{U}(\lambda_1, \phi_1, t_1), \delta)$. We illustrate what was just said in figure 4.6.

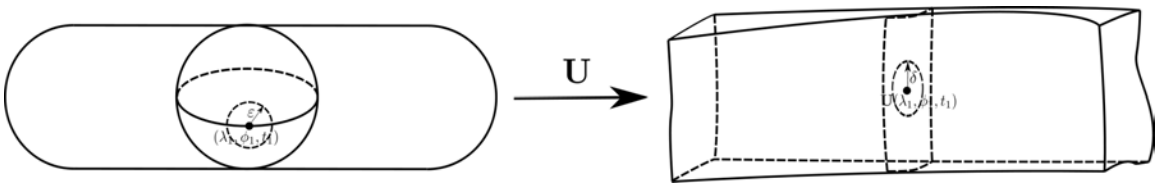

Figure 4.6: For our analysis, we suppose a ball in the domain is projected on a ball on the final panoramic video.

Suppose, for example, that φ_{t_1,t_2} scales $B((\lambda_1, \phi_1, t_1), \varepsilon)$ twice and changes its position

(from (λ_1, ϕ_1, t_1) to (λ_2, ϕ_2, t_2)). We illustrate this transformation in both tangent planes $T_{(\lambda_1,\phi_1,t_1)}\mathbb{TS}^2$ and $T_{(\lambda_2,\phi_2,t_2)}\mathbb{TS}^2$ in figure 4.7.

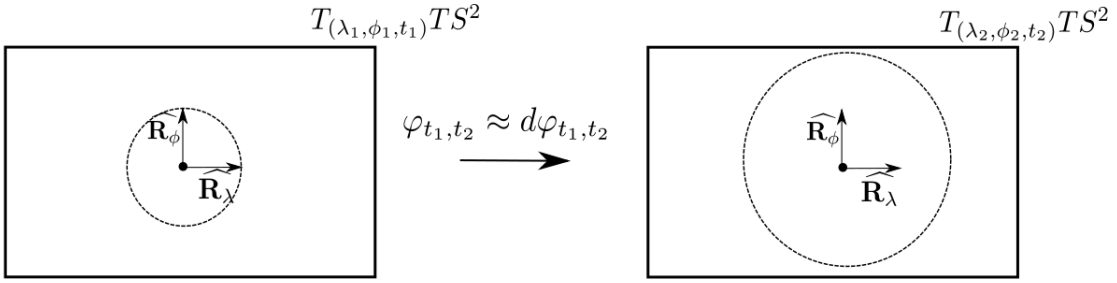

Figure 4.7: The action of the transition function for this example: it doubles the ball and changes its position.

Observe that φ_{t_1,t_2} only transforms textures from one viewing sphere to another, it does not change the geometry of any of the spheres.

In order to transport the scaling for the final panoramic video we have to *preserve* the tangent vectors $\mathbf{H}$ and $\mathbf{K}$ and the change of texture between the equirectangular domains will cause the expected result. Figure 4.8 shows what we just explained.

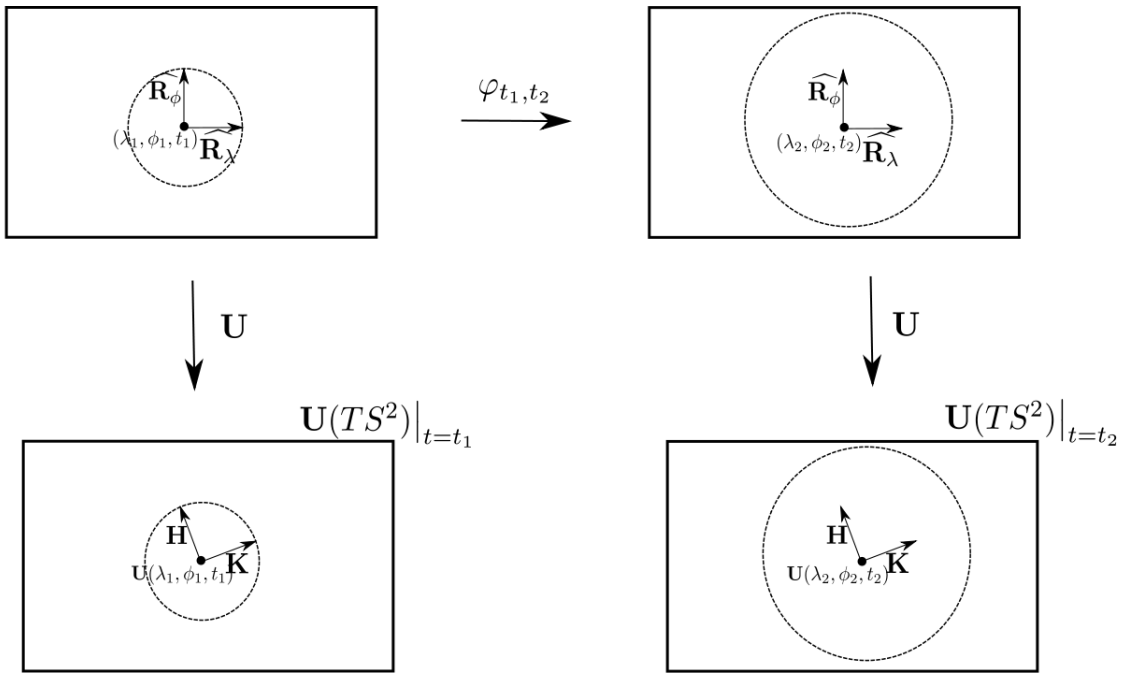

Figure 4.8: The ball in the panoramic video will be doubled from one time to another if $\mathbf{H}(\varphi_{t_1,t_2}(\lambda, \phi, t_1)) = \mathbf{H}(\lambda, \phi, t_1)$ and $\mathbf{K}(\varphi_{t_1,t_2}(\lambda, \phi, t_1)) = \mathbf{K}(\lambda, \phi, t_1)$.

The construction we just did holds for any transition function. Thus we obtain the following temporal coherence equations for object movement:

$$\begin{cases} \mathbf{H}(\varphi^{ob}_{t_1,t_2}(\lambda, \phi, t_1)) &= \mathbf{H}(\lambda, \phi, t_1) \\ \mathbf{K}(\varphi^{ob}_{t_1,t_2}(\lambda, \phi, t_1)) &= \mathbf{K}(\lambda, \phi, t_1) \end{cases}.$$

Assuming conformality for each time ($\mathbf{H}(\lambda, \phi, t) = R_{90}\mathbf{K}(\lambda, \phi, t)$), we use only the equation involving the differential north vector, the first one.

If $\varphi^{ob}_{t_1,t_2}(\lambda,\phi,t_1) = (\lambda^{ob}_{t_1,t_2}(\lambda,\phi,t_1), \phi^{ob}_{t_1,t_2}(\lambda,\phi,t_1), t_2)$, the equation can be rewritten as

$$\begin{cases} \dfrac{\partial U}{\partial \phi}(\lambda^{ob}_{t_1,t_2}(\lambda,\phi,t_1), \phi^{ob}_{t_1,t_2}(\lambda,\phi,t_1), t_2) &= \dfrac{\partial U}{\partial \phi}(\lambda,\phi,t_1) \\ \dfrac{\partial V}{\partial \phi}(\lambda^{ob}_{t_1,t_2}(\lambda,\phi,t_1), \phi^{ob}_{t_1,t_2}(\lambda,\phi,t_1), t_2) &= \dfrac{\partial V}{\partial \phi}(\lambda,\phi,t_1) \end{cases},$$

$\forall (\lambda,\phi,t_1) \in S^{ob}_{t_1} \times \{t_1\}$, $\forall t_1, t_2 \in [0,t_0]$, where $S^{ob}_{t_1} \times \{t_1\}$ is the region that the object occupies at time t_1 in the equirectangular domain. These are the *temporal coherence equations for moving objects* in the scene.

An analogous development lead to *temporal coherence equations for the entire scene*:

$$\begin{cases} \dfrac{\partial U}{\partial \phi}(\lambda^{sc}_{t_1,t_2}(\lambda,\phi,t_1), \phi^{sc}_{t_1,t_2}(\lambda,\phi,t_1), t_2) &= \dfrac{\partial U}{\partial \phi}(\lambda,\phi,t_1) \\ \dfrac{\partial V}{\partial \phi}(\lambda^{sc}_{t_1,t_2}(\lambda,\phi,t_1), \phi^{sc}_{t_1,t_2}(\lambda,\phi,t_1), t_2) &= \dfrac{\partial V}{\partial \phi}(\lambda,\phi,t_1) \end{cases},$$

$\forall (\lambda,\phi,t_1) \in S^{sc}_{t_1} \times \{t_1\}$, $\forall t_1, t_2 \in [0,t_0]$, where $S^{sc}_{t_1} \times \{t_1\}$ is the set of all points in the scene at time t_1 that will be projected.

In the particular case we are considering (case 1), $\lambda^{sc}_{t_1,t_2}(\lambda,\phi,t_1) = \lambda$ and $\phi^{sc}_{t_1,t_2}(\lambda,\phi,t_1) = \phi$, since the viewpoint is stationary. Thus, in this case, the equations are the following:

$$\begin{cases} \dfrac{\partial U}{\partial \phi}(\lambda,\phi,t_2) &= \dfrac{\partial U}{\partial \phi}(\lambda,\phi,t_1) \\ \dfrac{\partial V}{\partial \phi}(\lambda,\phi,t_2) &= \dfrac{\partial V}{\partial \phi}(\lambda,\phi,t_1) \end{cases},$$

$\forall (\lambda,\phi,t_1) \in [\alpha_1,\alpha_2] \times [\beta_1,\beta_2] \times \{t_1\}$, $\forall t_1, t_2 \in [0,t_0]$.

4.6.2 Discretization of the temporal viewing sphere

In this section, we discretize the temporal viewing sphere in an analogous manner we did to discretize the viewing sphere (section 2.3). We discretize the entire temporal viewing sphere $\mathbb{S}^2 \times [0,t_0] = \mathbb{TS}^2$, but all the development is analogous if we use a cube of the form $[\alpha_1,\alpha_2] \times [\beta_1,\beta_2] \times [0,t_0]$, which is the domain of projection for case 1.

We stated the panoramic video problem as the one of finding a function

$$\begin{array}{rccc} \mathbf{U}: & \mathbb{TS}^2 & \to & \mathbb{R}^3 \\ & (\lambda,\phi,t) & \mapsto & (U(\lambda,\phi,t), V(\lambda,\phi,t), t) \end{array}.$$

We replace this continuous problem by finding $\mathbf{U}$ on a discrete mesh $((\Lambda_{ijk}) = (\lambda_j, \phi_i, t_k))$, where

$$\lambda_j = -\pi + j\frac{2\pi}{n},\ j = 0,\dots,n,$$
$$\phi_i = -\frac{\pi}{2} + i\frac{\pi}{m},\ i = 0,\dots,m,$$
$$t_k = 0 + k\frac{t_0}{l},\ k = 0,\dots,l.$$

The parameters m and n can be chosen (as we did for panoramic images) and the parameter l is the number of frames in the input equirectangular video.

The values of $\mathbf{U}$ at Λ_{ijk} will be denoted by

$$\mathbf{U}_{ijk} = (U_{ijk}, V_{ijk}, t_k),\ j = 0,\dots,n,\ i = 0,\dots,m,\ k = 0,\dots,l.$$

4.6.3 Total energy, minimization and results

In this section, we produce a panoramic video using all the theory developed in this chapter.

We use as input equirectangular video the video shown in figures 4.2 and 4.3 with 16 frames. We mark the lines for the first frame. Since the viewpoint is stationary, they do not move across time, so it is enough to mark them only in the first frame. The marked lines are shown in figure 4.9.

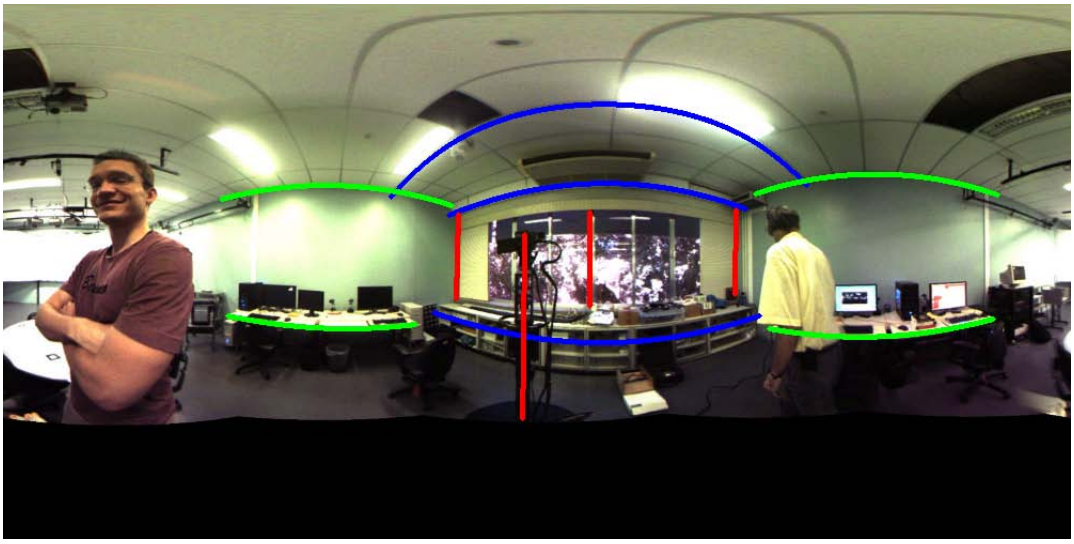

Figure 4.9: Marked lines for the example video.

The first step is to obtain an optimal panoramic image for the first frame. Since the background is stationary, we use the orientations of lines obtained from this frame to use in all frames in the video. This avoids the alternation between minimizing E_{ld} and E_{lo} which may be a computational time problem for videos.

We now introduce some notation. The solution vector $\mathbf{X}$ will be composed by solution vectors for each frame with the notation of last chapters. For example, the first entries of $\mathbf{X}$ will correspond to entries of the solution of frame $k = 0$, using the order of the previous chapters:

$$\mathbf{X} = \begin{pmatrix} U_{000} & V_{000} & \cdots & U_{mn0} & V_{mn0} & \cdots & \cdots & U_{00l} & V_{00l} & \cdots & U_{mnl} & V_{mnl} \end{pmatrix}^T.$$

We also construct a vector $\mathbf{Y}$ which is the stereographic mapping $\mathbf{y}$ for each instant:

$$\mathbf{Y} = \begin{pmatrix} \mathbf{y} \\ \vdots \\ \mathbf{y} \end{pmatrix}.$$

We start to determine a panoramic video by satisfying the first desirable property: each frame should be a good panoramic image. The sum of (image) energies for each

frame can be written in matrix form as

$$E = \left\| \begin{pmatrix} & A_o & & \\ & & \ddots & \\ & & & A_o \end{pmatrix} \begin{pmatrix} U_{000} \\ \vdots \\ V_{mn0} \\ \vdots \\ U_{00l} \\ \vdots \\ V_{mnl} \end{pmatrix} \right\|^2 .$$

We minimize this energy in the same way we did for images:

$$\mathbf{X} = (A^T A + \varepsilon I)^{-1}(\varepsilon \mathbf{Y}).$$

The solution, as it is expected, is always the same projection, the only thing that changes is the texture that is being projected. This solution leads to temporal incoherence for the objects in the scene. In figures 4.10 and 4.11, we see that the man walking starts with an orientation and finishes with another, which is undesirable since this behavior does not happen in the input video.

Figure 4.10: 8th frame for the video produced using only image energies. The man has a well defined vertical orientation in this frame. FOV: 180 longitude/120 latitude.

To correct this problem, we use the temporal coherence equations for the object. Doing that, we also satisfy desirable property 4. Rewriting the equations, we have:

$$\begin{cases} \dfrac{\partial U}{\partial \phi}(\lambda^{ob}_{t_1,t_2}(\lambda,\phi,t_1),\phi^{ob}_{t_1,t_2}(\lambda,\phi,t_1),t_2) - \dfrac{\partial U}{\partial \phi}(\lambda,\phi,t_1) &= 0 \\ \dfrac{\partial V}{\partial \phi}(\lambda^{ob}_{t_1,t_2}(\lambda,\phi,t_1),\phi^{ob}_{t_1,t_2}(\lambda,\phi,t_1),t_2) - \dfrac{\partial V}{\partial \phi}(\lambda,\phi,t_1) &= 0 \end{cases},$$

Figure 4.11: 16th frame for the video produced using only image energies. Due to the lines near the man, he is very curved in this frame. This fact demonstrates temporal incoherence, since he remains vertical in the input video.

$\forall(\lambda, \phi, t_1) \in S^{ob}_{t_1} \times \{t_1\}$, $\forall t_1, t_2 \in [0, t_0]$. In the discretized version of the equations, we only use the transition functions from one frame to the next, i.e., we take $t_1 = t_k$ and $t_2 = t_{k+1}$.

We denote $(\lambda^{ob}_{t_1,t_2}(\lambda, \phi, t_1), \phi^{ob}_{t_1,t_2}(\lambda, \phi, t_1))$ by $(j_{k,k+1(i,j,k)}, i_{k,k+1(i,j,k)})$. We always map vertices to vertices on the discretization. If that does not happen, we map to the closest vertex. The discretization of the equations is:

$$\begin{cases} \dfrac{U_{i_{k,k+1(i,j,k)+1},j_{k,k+1(i,j,k)},k+1} - U_{i_{k,k+1(i,j,k)},j_{k,k+1(i,j,k)},k+1}}{\Delta\phi} - \left(\dfrac{U_{i+1,j,k} - U_{ijk}}{\Delta\phi}\right) &= 0 \\ \dfrac{V_{i_{k,k+1(i,j,k)+1},j_{k,k+1(i,j,k)},k+1} - V_{i_{k,k+1(i,j,k)},j_{k,k+1(i,j,k)},k+1}}{\Delta\phi} - \left(\dfrac{V_{i+1,j,k} - V_{ijk}}{\Delta\phi}\right) &= 0 \end{cases},$$

$\forall(\lambda_j, \phi_i, t_k) \in S^{ob}_{t_k} \times \{t_k\}$.

We use the last equations to formulate the *object temporal coherence energy:*

$$\begin{aligned} E_{ob} &= \sum_{k=0}^{l-1} \sum_{(i,j)\in S^{ob}_{t_k}} \cos^2(\phi_i) \left(\frac{U_{i_{k,k+1(i,j,k)+1},j_{k,k+1(i,j,k)},k+1} - U_{i_{k,k+1(i,j,k)},j_{k,k+1(i,j,k)},k+1} - U_{i+1,j,k} + U_{ijk}}{\Delta\phi}\right)^2 \\ &+ \sum_{k=0}^{l-1} \sum_{(i,j)\in S^{ob}_{t_k}} \cos^2(\phi_i) \left(\frac{V_{i_{k,k+1(i,j,k)+1},j_{k,k+1(i,j,k)},k+1} - V_{i_{k,k+1(i,j,k)},j_{k,k+1(i,j,k)},k+1} - V_{i+1,j,k} + V_{ijk}}{\Delta\phi}\right)^2 \end{aligned}$$

It is not difficult to rewrite E_{ob} in the matrix form $E_{ob} = \|OB\mathbf{X}\|^2$, but we do not detail this part here. We join this new energy to the previous one and obtain

$$E = \|A\mathbf{X}\|^2,$$

where

$$A = \begin{pmatrix} A_o & & & \\ & \ddots & & \\ & & A_o & \\ & w_{ob}OB & & \end{pmatrix}.$$

w_{ob} is a weight that controls the strength of this new energy. Using $w_{ob} = 4$ in our example corrects the problem of too much orientation change in the object. We show the new result in figures 4.12 and 4.13.

Figure 4.12: 8th frame for the video produced using image energies and object energy.

Now the scene starts to change in order to preserve shape and orientation of the object. Thus, it becomes necessary to impose temporal coherence for the scene, which was stated as desirable property 3 in section 4.3.

We rewrite the temporal coherence equations for this case:

$$\begin{cases} \dfrac{\partial U}{\partial \phi}(\lambda, \phi, t_2) - \dfrac{\partial U}{\partial \phi}(\lambda, \phi, t_1) &= 0 \\ \dfrac{\partial V}{\partial \phi}(\lambda, \phi, t_2) - \dfrac{\partial V}{\partial \phi}(\lambda, \phi, t_1) &= 0 \end{cases},$$

$\forall (\lambda, \phi, t_1) \in [\alpha_1, \alpha_2] \times [\beta_1, \beta_2] \times \{t_1\}$, $\forall t_1, t_2 \in [0, t_0]$. Using the discretization of the temporal viewing sphere and only transitions between t_k and t_{k+1}, we obtain the following

Figure 4.13: 16th frame for the video produced using image energies and object energy. Comparing to figure 4.11 the man is less curved, as expected. Now other problem arises: the projection for the entire scene changes too much to satisfy object constrains. One can observe, for example, that the borders of the projection from 8th frame to 16th frame change.

discretized equations:

$$\begin{cases} \dfrac{U_{i+1,j,k+1} - U_{i,j,k+1}}{\Delta\phi} - \left(\dfrac{U_{i+1,j,k} - U_{i,j,k}}{\Delta\phi}\right) &= 0 \\ \dfrac{V_{i+1,j,k+1} - V_{i,j,k+1}}{\Delta\phi} - \left(\dfrac{V_{i+1,j,k} - V_{i,j,k}}{\Delta\phi}\right) &= 0 \end{cases},$$

$i = 0, \ldots, m-1$, $j = 0, \ldots, n$, $k = 0, \ldots, l-1$. The above equations lead to the *scene temporal coherence energy*:

$$\begin{aligned} E_{sc} &= \sum_{i=0}^{m-1}\sum_{j=0}^{n}\sum_{k=0}^{l-1} \cos^2(\phi_i)\left(\frac{U_{i+1,j,k+1} - U_{i,j,k+1} - U_{i+1,j,k} + U_{ijk}}{\Delta\phi}\right)^2 \\ &+ \sum_{i=0}^{m-1}\sum_{j=0}^{n}\sum_{k=0}^{l-1} \cos^2(\phi_i)\left(\frac{V_{i+1,j,k+1} - V_{i,j,k+1} - V_{i+1,j,k} + V_{ijk}}{\Delta\phi}\right)^2 . \end{aligned}$$

We rewrite E_{sc} in matrix form $E_{sc} = \|SC\mathbf{X}\|^2$. The new total energy is

$$E = \|A\mathbf{X}\|^2 ,$$

where

$$A = \begin{pmatrix} A_o & & & \\ & \ddots & & \\ & & A_o & \\ w_{ob}OB & & & \\ w_{sc}SC & & & \end{pmatrix}.$$

We set $w_{sc} = 12$ and corrected the problem of the background "shaking" to preserve the object. We show some frames of the new result in figures 4.14 and 4.15.

Figure 4.14: 8th frame for the video produced using image, object and scene energies.

We observe now that the object regions lose conformality and smoothness due to the extra constrains imposed on them. For example, see figure 4.15.

In order to correct this problem (and also to satisfy desirable property 2) we increase conformality and smoothness in object regions using *spatially-temporally-varying weights*. For each time t_k, the image weights ($w_{i,j}$ in section 2.7) will be replaced by

$$w_{i,j,k} = 2w^L_{i,j} + 2w^S_{i,j} + 4w^F_{i,j} + 1 + w^{ob}_{i,j,k} = w_{i,j} + w^{ob}_{i,j,k}.$$

The weights $w^{ob}_{i,j,k}$ are defined in the following way: Let (λ_c, ϕ_c, t_k) be the center of the object and σ_k the radius of the object at time t_k. We define

$$w^{ob}_{i,j,k} = e^{-\frac{\left\|(\lambda_j,\phi_i,t_k)-(\lambda_j,\phi_i,t_k)\right\|^2}{2\sigma_k^2}},$$

Figure 4.15: 16th frame for the video produced using image, object and scene energies.

a gaussian centered at (λ_c, ϕ_c, t_k) with radius σ_k and height 1. Since we have only one object, we do not need to sum over all objects to determine the final weights.

To plug this weight into our energy, we have to change the matrices C and S in A_o, leading to different matrices $A_o^{(k)}$ for different times. The new matrix will be

$$A = \begin{pmatrix} A_o^0 & & & \\ & \ddots & & \\ & & A_o^l & \\ w_{ob}OB & & & \\ w_{sc}SC & & & \end{pmatrix}.$$

The effect of these new weights is shown in figure 4.16.

We make available all partial results (with and without energies and weights) that we discussed in this section in [22].

4.6.4 Implementation Details

All results in last section were generated using a discretization of the temporal viewing sphere of 60,000 vertices, 3,705 vertices per frame. The time to compute the final video was about 8 minutes. The part of the method that is the most time consuming is solving

Figure 4.16: 16th frame for the video produced using image, object and scene energies and object weights. The man is less stretched if compared to 4.15.

the final linear system

$$(A^T A + \varepsilon I)\mathbf{X} = \varepsilon \mathbf{Y}.$$

We did a very simple implementation to determine the transition functions for the object in the scene. For each frame, we drew a box around the object. We identified the box as the object and assumed it to have same size for all frames, thus the transition functions were only translations. We show in figure 4.17 a frame illustrating what was just said.

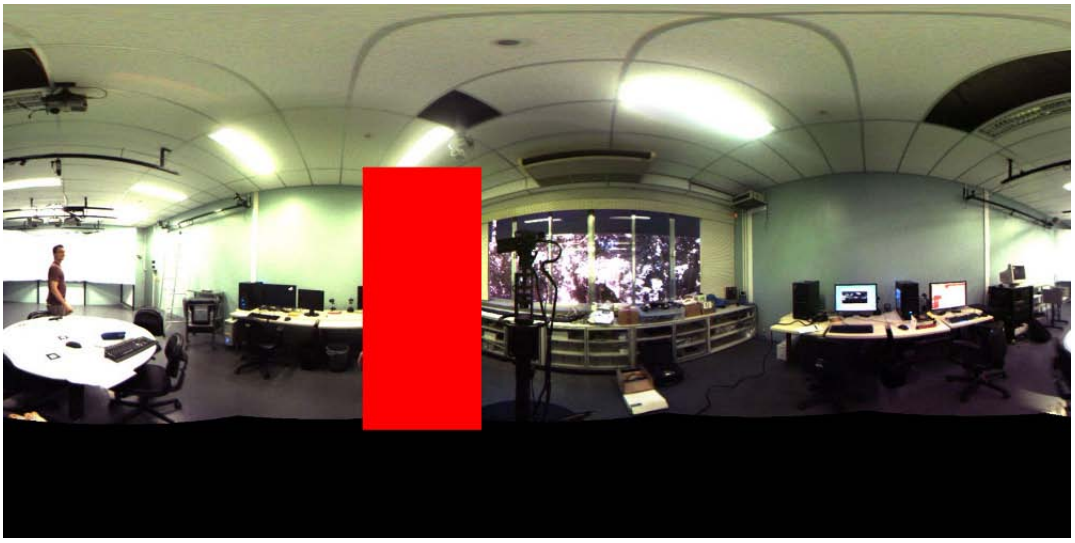

Figure 4.17: For each frame, a box around the object was drawn.

4.6.5 Other Solutions

In this section, we discuss other possible solutions for case 1.

One other solution, which is actually an extension to the one we proposed is to involve more precise object extraction and transition functions. Since the background is stationary, background subtraction could be used to this end. Also, the way we modeled object constrains introduce many constrain discontinuities in the equirectangular video. A way of making such constrains smoother becomes necessary.

Other possible solution is to solve separately the projection for the background and foreground and combine them after. This separation would lead to two simpler problems. The final combination could be achieved by combining the projections or composting the resulting images. Some problems like incoherence between background and foreground could appear. Also, interactions between background and foreground would be difficult to model.

We intend to implement these different solution soon and compare them to the one we proposed in this thesis.

4.7 Case 2 - Stationary VP, Moving FOV and Stationary Objects

We propose in this section a solution for case 2. For each time $t \in [0, t_0]$, we project the set $[\alpha_1^{(t)}, \alpha_2^{(t)}] \times [\beta_1^{(t)}, \beta_2^{(t)}] \times \{t\} = S^{(t)} \times \{t\}$, i.e., the FOV that will be projected depends on time.

This case may be seen as a viewer of panoramas where each view is a panoramic image.

4.7.1 Temporal Coherence Equations

For case 2, we do not have moving objects in the scene. Thus, there is no transition function $\varphi^{ob}_{t_1,t_2}$.

Since all the scene is stationary on the temporal viewing sphere, the transition function for the scene is

$$\begin{array}{rccc} \varphi_{t_1,t_2}: & S^{(t_1)} \cap S^{(t_2)} \times \{t_1\} & \rightarrow & S^{(t_1)} \cap S^{(t_2)} \times \{t_2\} \\ & (\lambda, \phi, t_1) & \mapsto & (\lambda, \phi, t_2) \end{array} .$$

Again, imposing the preservation of the differential north vector, we obtain the *scene temporal coherence equations* for this case:

$$\left\{ \begin{array}{rcl} \dfrac{\partial U}{\partial \phi}(\lambda, \phi, t_2) & = & \dfrac{\partial U}{\partial \phi}(\lambda, \phi, t_1) \\ \dfrac{\partial V}{\partial \phi}(\lambda, \phi, t_2) & = & \dfrac{\partial V}{\partial \phi}(\lambda, \phi, t_1) \end{array} \right. ,$$

$\forall (\lambda, \phi, t_1) \in S^{(t_1)} \cap S^{(t_2)} \times \{t_1\}$, $\forall t_1, t_2 \in [0, t_0]$.

4.7.2 A solution

A naive solution for case 2 would be, for each t_k in the discretization of the temporal viewing sphere, to obtain the optimal panoramic image for projecting $[\alpha_1^{(t_k)}, \alpha_2^{(t_k)}] \times [\beta_1^{(t_k)}, \beta_2^{(t_k)}] \times \{t_k\}$. As the FOV moves, marked lines in the scene come in and out the FOV, what leads to different constrains from one time to another and leads to problems of size and orientation in the scene. An example of temporally incoherent video constructed in this way is available in [22].

Another solution, which considers temporal coherence, would be to discretize the scene temporal coherence equations, obtain an energy term and compute a panoramic video by optimizing an energy that joins panoramic image energies and this new term, just as we did for case 1. Due to time constrains, we have not implemented this solution and we leave it to future work.

We propose a simpler solution for case 1. We obtain an optimal panoramic image for a FOV that contains all FOVs $[\alpha_1^{(t_k)}, \alpha_2^{(t_k)}] \times [\beta_1^{(t_k)}, \beta_2^{(t_k)}]$. We take

$$S = \bigcup_{k=0}^{l} [\alpha_1^{(t_k)}, \alpha_2^{(t_k)}] \times [\beta_1^{(t_k)}, \beta_2^{(t_k)}]$$

we calculate the optimal panoramic image function

$$\begin{array}{rccl} \mathbf{u}: & S & \to & \mathbb{R}^2 \\ & (\lambda, \phi) & \mapsto & (u(\lambda, \phi), v(\lambda, \phi)) \end{array}$$

and, for each t_k we define

$$\begin{array}{rccl} \mathbf{U}: \ [\alpha_1^{(t_k)}, \alpha_2^{(t_k)}] \times [\beta_1^{(t_k)}, \beta_2^{(t_k)}] \times \{t_k\} & \to & \mathbb{R}^3 \\ (\lambda, \phi, t_k) & \mapsto & (u(\lambda, \phi), v(\lambda, \phi), t_k) \end{array},$$

i.e., each frame of the panoramic video will be the region of the panoramic image corresponding to the FOV that is being projected.

It is not difficult to see that this construction satisfies the temporal coherence equations: since the projections are the same for different times, the derivatives will also be the same. The final video is not an optimal panoramic video because each frame of the video may not be an optimal panoramic image for the FOV that is being projected (it is optimal only for S).

We make available in [22] an example of panoramic video constructed in the way we just explained. This example may be compared to the temporally incoherent solution.

We think the optimization framework would lead to similar results, and this comparison is also left to future work.

4.8 Concluding Remarks

As we mentioned in the beginning of this chapter, what we developed here was just first step in our research on panoramic videos. But even here we could see how important

temporal aspects are in modeling panoramic videos.

We left aside in this chapter case 3 of panoramic videos. This case is the most difficult one, since all the scene is moving, not only moving objects. Separation between moving objects and scene is less trivial, and also it will be more difficult to model the transition functions. Maybe a way of modeling them is with the help of perspective projections, since the geometry of such projections is well understood. For narrow fields of view, the perspective projection could be used to determine transition functions on neighborhoods of points and also determine if the point is a part of a moving object.

Many things in this chapter were pointed as future work. We make a summary of future work related to panoramic videos in the conclusion of this thesis.

Appendix A

Application Software

This chapter intends to complement the theory developed in chapters 2 and 3, through the exposition of an application that implements everything that was discussed in such chapters and is user friendly. We provide a manual of how to use such application and give implementation details.

In section A.1, we show our application working. It consists in two windows where the user interacts, and a processing step performed in Matlab that computes the final panoramic based on the information passed by the user into the two windows. We also explain how to use the program, thus the reader of this thesis can try it and produce her own results.

Section A.2 is devoted to explain how the application was implemented. Although we do not show many source codes, the details we consider most essential for the overall process will be provided. We assume the reader is familiarized to programming in C/C++ and Matlab languages for a complete understanding of this section.

A.1 Application and user's manual

We developed a software application that implements all the theory of chapters 2 and 3 but isolates it from the user, i.e., even people who do not know the theoretical details of the method can use the application.

We made a video of our interface working, which can be found in the home page of this thesis ([22]). For a better understanding of what will be explained here we recommend the reader to download such video and watch it together with the explanation.

The reader that is interested on having our application can contact us through the e-mail that is also in [22]. The application will be sent as a compressed folder containing the binary files corresponding to compiled programs in C++ and Matlab programs (.m files).

To run our program, the system must have installed Matlab and OpenCV and FLTK libraries.

The input is an equirectangular image in the PPM format. It is recommended that it has a good resolution, 4000 by 2000 pixels for example. It will be more clear further why we make this requirement. The input image for our example is shown in figure A.1.

Figure A.1: Source image: "*Musée du Louvre*", by Flickr user Gadl.

On the terminal the user goes to the directory corresponding to the application (we named it as *panorama*). There she just types

```
./run.sh images/test_image
```

In this example, the input image must be in the directory '*images*' with the name '*test_image.ppm*'.

This command will open window 1, which is shown in figure A.2.

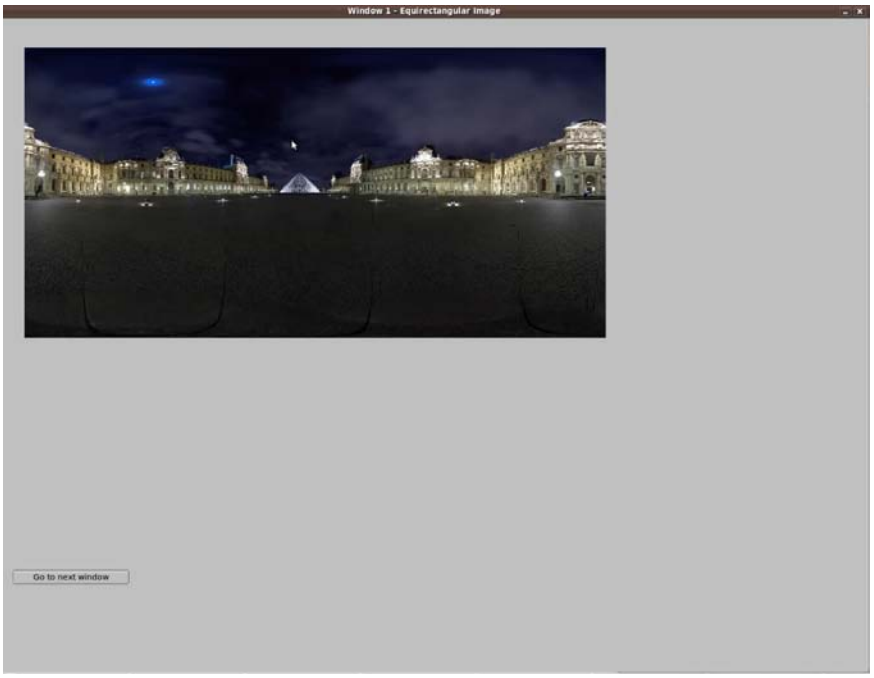

Figure A.2: Window 1 loads the input image and allows the user to mark lines on it.

This window corresponds to the user interface explained in section 2.2, where the user mark the lines that she expects to be straight in the final result. Clicking on the two

endpoints of the line will plot the corresponding curve in black. Then the user types 'v', 'h' or 'g' to specify if the line should be vertical, horizontal or with general orientation on the final result. After marking such lines, window 1 is as shown in figure A.3.

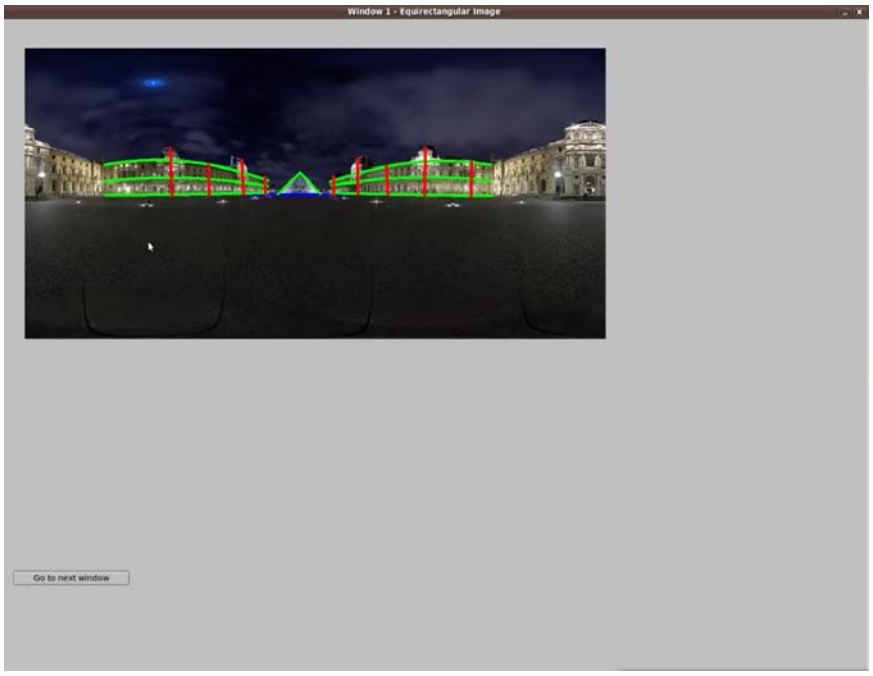

Figure A.3: Window 1 after the process of marking lines.

Clicking on "*go to next window*" button takes the user to window 2, which is shown in figure A.4.

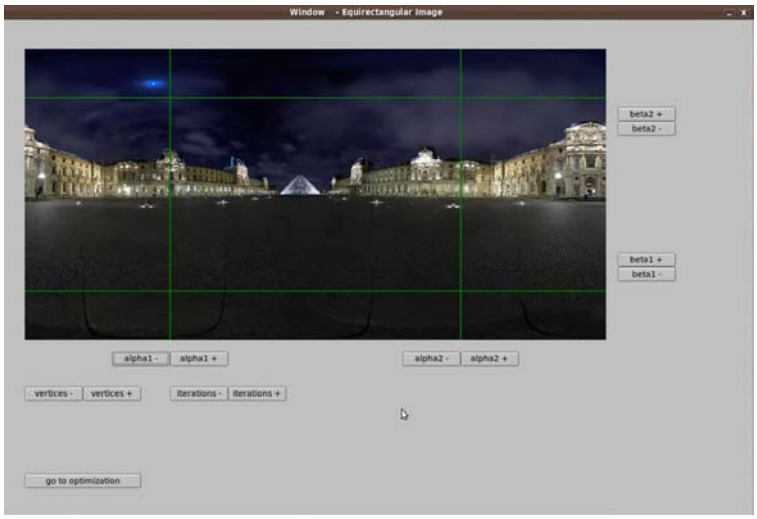

Figure A.4: Window 2 shows and allows to specify the field of view that is going to be projected.

This second window was not done in [1], it is a new feature from our implementation. It allows the user to choose the field of view that is going to be projected, the number of vertices for the discretization of the viewing sphere and the number of double iterations.

The buttons "*alpha 1 -*", "*alpha 1 +*", "*alpha 2 -*", "*alpha 2 +*", "*beta 1 -*", "*beta 1 +*", "*beta 2 -*" and "*beta 2 +*" allows the user to choose the FOV $[\alpha_1, \alpha_2] \times [\beta_1, \beta_2] \subseteq$

$[-\pi, \pi] \times [-\frac{\pi}{2}, \frac{\pi}{2}]$ that is going to be projected. When the user clicks these buttons, the image changes in order to show the FOV in the rectangle determined by the four green lines.

If the buttons "*iterations -*", "*iterations +*" or "*vertices -*", "*vertices +*" are clicked, the user sees in the command line the number of iterations or number of vertices that she is specifying (figure A.5).

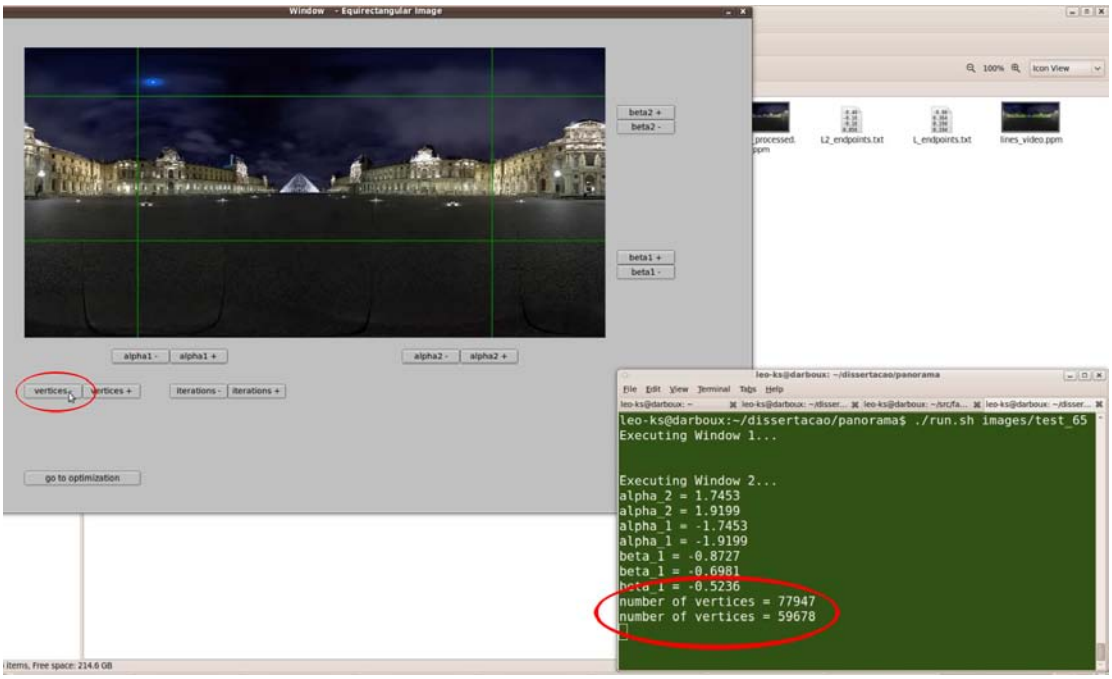

Figure A.5: The user sees the number of vertices she is specifying, for example.

When the user clicks "*go to optimization*", Matlab is run to perform the optimizations. Each time that an iteration is finished, the user sees the energy value in the terminal, as shown in figure A.6.

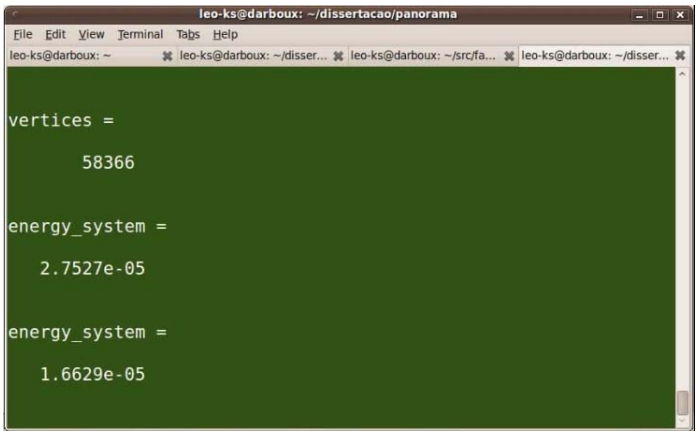

Figure A.6: The energy value is displayed at the end of each iteration.

After the optimization, the result is saved as "*result.ppm*" in the folder of the application (*panorama*, in our case). The result for the example in this section is shown in figure A.7.

Figure A.7: The final result obtained for this example. Field of view: 220 degree longitude/ 90 degree latitude.

A.2 Implementation Details

This section is devoted to explain how we developed the application presented in the last section. We try not to get too deep into all details, but show the most essential ones for the understanding of our implementation.

Figure A.8 shows the structure of our application software.

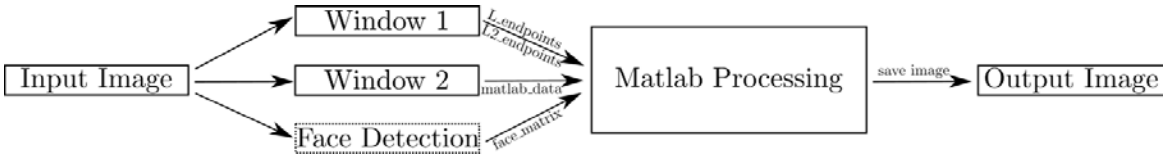

Figure A.8: Structure of our application software.

We developed a shell script to perform all these steps in an integrated way. When the user runs the script, it seems that is only one program running, but actually all the steps described in figure A.8 are performed each one at a time. This script is run by the command '*./run.sh*', as explained in the previous section.

In this section, we explain implementation details of windows 1 and 2 and Matlab processing, which is the most important module, since it implements most of the theory explained in chapters 2 and 3.

Face detection module is detailed in the next section. We placed it in a different section to emphasize the face detection process in equirectangular images, which is a method itself.

A.2.1 Window 1

Window 1 was implemented in C++ language, using FLTK (Fast Light Toolkit) API (application programming interface). Window 1 was shown in figures A.2 and A.3. It consists basically in a box that shows the marked equirectangular image and a close button.

We developed a class *Box* that inherits the properties of the class *Fl_box*. The difference of this new class is that it handles mouse click events and typing 'h', 'v' or 'g' events. When two points are clicked and one of the keys 'h', 'v' or 'g' are pressed, the class calls a function named *draw_arc* that draws the corresponding arc connecting these two points. Finally, the image on the *Box* is reloaded.

The curve drawn is only useful for interaction purposes. The *draw_arc* function also saves in a text file the coordinates of the endpoints, an index for the line and the specified orientation[1].

After the process of marking lines is finished, the user clicks on the "*close window*" button, which has a callback to close the window. Then another function is called to separate the points in the generated text file into points corresponding to lines with specified orientation and points corresponding to lines with general orientation. These files are saved as *L_endpoints* and *L2_endpoints*. Such files will be loaded by Matlab into a matrix form.

We show below an example of an *L_endpoints* file:

```
-0.80423999 -0.01256000 1 2
0.36442399 -0.01256000 1 2
0.19477800 0.18849500 2 1
0.19477800 -0.02513000 2 1
0.45867199 0.38327399 3 1
0.45867199 -0.01256000 3 1
0.76654798 0.30159199 4 1
0.78539801 -0.01256000 4 1
1.18752205 0.49637100 5 1
1.18123806 -0.02513000 5 1
1.69017601 0.33929199 6 1
1.68389297 -0.03769000 6 1
-0.54663002 0.18221200 7 1
-0.54035002 -0.01256000 7 1
-0.79795998 0.36442399 8 1
-0.77911001 -0.01256000 8 1
-1.15610003 0.31415901 9 1
-1.14981997 -0.03141000 9 1
```

[1] 1 stands for vertical lines, 2 for horizontal lines and three for general orientation lines.

```
-1.57079005 0.49637100 10 1
-1.55193996 -0.03141000 10 1
-1.99804997 0.33929199 11 1
-2.01061010 -0.03141000 11 1
```

A.2.2 Window 2

Window 2 was also developed with C++ language using FLTK API. Window 2 was shown in figures A.4 and A.5. It consists in a box, some buttons that regulate the parameters that will be passed to the optimization and a close button.

A class with the parameters for the optimization was developed. This class was named *alg_parameters*:

```
class alg_parameters{
public:
    float alpha_1;
    float alpha_2;
    float beta_1;
    float beta_2;
    int iterations;
    int factor;
    char input_image[100];
    char output_image[100];
    int m;
    char work_image_name[100];
public:
    alg_parameters(char* input_image2, char* output_image2, int m2); //constructor
    alg_parameters(); //empty constructor
    void print();
};
```

alpha_1, *alpha_2*, *beta_1*, and *beta_2* determine what field of view $[\alpha_1, \alpha_2] \times [\beta_1, \beta_2] \subseteq [-\pi, \pi] \times [-\frac{\pi}{2}, \frac{\pi}{2}]$ will be projected. The buttons "*alpha 1 -*", "*alpha 1 +*", "*alpha 2 -*", "*alpha 2 +*", "*beta 1 -*", "*beta 1 +*", "*beta 2 -*" and "*beta 2 +*" update these values and the image inside the box is also updated. For this window, the box with the image only has function of loading an updated image, whenever the parameters *alpha_1*, *alpha_2*, *beta_1*, and *beta_2* are updated.

The parameter *iterations* stands for the number of double iterations (section 3.3). The buttons "*iterations -*", "*iterations +*" update these values.

factor controls the number of vertices in the following way: if the size in the equirectangular image of the field of view that will be projected is $m \times n$ pixels, the number of

vertices of the discretization of $[\alpha_1, \alpha_2] \times [\beta_1, \beta_2]$ will be $\frac{m}{factor} \times \frac{n}{factor}$.

The output of this window is a text file containing the parameters *alpha_1*, *alpha_2*, *beta_1*, *beta_2*, *factor* and *iterations*. The name of this file is *matlab_data.txt*. We show below an example of such file:

```
-1.9199 1.9199 -0.5236 1.0472 9 3
```

A.2.3 Matlab processing

This module consists in four submodules as illustrated in figure A.9.

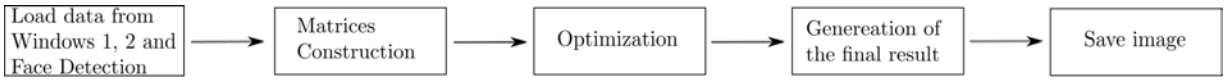

Figure A.9: The steps performed in Matlab.

Next, we explain each of the submodules briefly.

• **Loading data:** Files *L_endpoints.txt*, *L2_endpoints.txt*, *matlab_data.txt* and *face_matrix.txt* are loaded using command *load* from Matlab. Each text archive is transformed in a matrix with the same structure of the text file. For example, for *matlab_data.txt* like below

```
-1.9199 1.9199 -0.5236 1.0472 9 3
```

the command returns the following matrix

```
matlab_data =

    [-1.9199 1.9199 -0.5236 1.0472 9 3]
```

• **Matrices construction:** This step constructs the conformality and smoothness matrices C and S (sections 2.4 and 2.6) and the stereographic mapping $\mathbf{y}$, that will be used to minimize $\tilde{E}$ as explained in section 2.8.3.

At this point, it is important to construct the matrices having in mind their sparse structure and how a sparse matrix is stored in Matlab. A naive way of constructing them leads this step to take longer than the optimization. We fixed this problem but we do not discuss it here.

• **Optimization:** This step starts by calculating the midpoint of each quad-line intersection (as described in section 2.5) and then obtaining the bilinear coefficients for each virtual output vertex (section 2.5.2).

With these values, the matrix LO is constructed. Also, the matrix LDA for the initial iteration is defined. Then the initial iteration (section 2.8.4) is performed using the code below:

```
function f = all_energies_initial_forsyth_minimization_2(L,L2,
C,S,LO,LDinit,m2,n2,alpha_1,alpha_2,beta_1,beta_2,y)

A = [0.4*C;0.05*S;10*LO;10*LDinit];

epsilon = 10^(-6);
B = sparse(2*m2*n2,2*m2*n2);
B = A'*A;
for i=1:2*m2*n2
    B(i,i) = B(i,i) + epsilon;
end
x = B\(epsilon*y);

f = x/norm(x);
```

To solve the linear system we used just the backslash tool ($x = B\backslash(epsilon * y)$) provided by Matlab, that uses the proper numerical method to solve such linear system.

The next step is to perform the number of double iterations specified by the user in Window 2 and the final iteration. The code is almost the same as the one used for the initial iteration.

• **Generation of the final result:** As we already mentioned, our discretization of $[\alpha_1, \alpha_2] \times [\beta_1, \beta_2]$ depends on the value *factor* returned by Window 2. This dependence is illustrated in figure A.10.

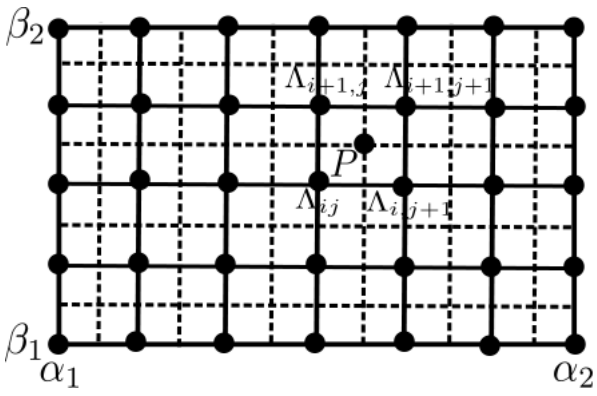

Figure A.10: The portion of the equirectangular image corresponding to $[\alpha_1, \alpha_2] \times [\beta_1, \beta_2]$ has 2 times more pixels (represented with dashed lines) than the number of vertices of the discretization of $[\alpha_1, \alpha_2] \times [\beta_1, \beta_2]$ (represented with solid lines). For this example, $factor = 2$.

As mentioned before, we do not have any control on the positions that the solution $\mathbf{x}$ of the optimization will return. Let

$$u_{min} = \min_{i,j} u_{ij},\ u_{max} = \max_{i,j} u_{ij},\ v_{min} = \min_{i,j} v_{ij},\ v_{max} = \max_{i,j} v_{ij}.$$

We map all values (u_{ij}, v_{ij}) to $(\tilde{u_{ij}}, \tilde{v_{ij}})$ such that $(\tilde{u_{ij}}, \tilde{v_{ij}}) \in [0, ratio * res] \times [0, res]$, according to the following transformation:

$$\tilde{u_{ij}} = \frac{u_{ij} - u_{min}}{u_{max} - u_{min}} * ratio * res, \ \tilde{v_{ij}} = \frac{v_{ij} - v_{min}}{v_{max} - v_{min}} * res,$$

where $ratio = \frac{u_{max} - u_{min}}{v_{max} - v_{min}}$ and res is a specified parameter that determines the height of the result image.

Each pixel on the equirectangular image (for example, pixel P in figure A.10) has known surrounding vertices on the discretization of $[\alpha_1, \alpha_2] \times [\beta_1, \beta_2]$ and known bilinear coefficients, say

$$P = a_{ij}\Lambda_{ij} + a_{i+1,j}\Lambda_{i+1,j} + a_{i,j+1}\Lambda_{i,j+1} + a_{i+1,j+1}\Lambda_{i+1,j+1},$$

$a_{ij} + a_{i+1,j} + a_{i,j+1} + a_{i+1,j+1} = 1$. We simply define that P is mapped to $(\tilde{u}(P), \tilde{v}(P))$ on the final image, where

$$\tilde{u}(P) = a_{ij}\tilde{u_{ij}} + a_{i+1,j}\tilde{u_{i+1,j}} + a_{i,j+1}\tilde{u_{i,j+1}} + a_{i+1,j+1}\tilde{u_{i+1,j+1}},$$

$$\tilde{v}(P) = a_{ij}\tilde{v_{ij}} + a_{i+1,j}\tilde{v_{i+1,j}} + a_{i,j+1}\tilde{v_{i,j+1}} + a_{i+1,j+1}\tilde{v_{i+1,j+1}}.$$

Thus, the final image is just a bilinear interpolation the positions of the vertices on the discretization of the viewing sphere.

A problem in this approach is that if the final image has a higher resolution than the input image, holes on the final image may appear. A more appropriate approach would be to use inverted bilinear interpolation (section 2.5.2). We leave this alternative as future work, and assume that the relation between input and output image is such that the output image has no holes.

• **Saving image:** If the result is stored in the matrix variable *result*, we use the command

```
imwrite(result, 'result.ppm', 'PPM')
```

to save it as *result.ppm*.

Appendix B

Feature Detection in Equirectangular Images

In this appendix, we explain the methods we have used to detect faces and lines in equirectangular images. For these both detections, we adapt standard Computer Vision techniques for the equirectangular image context. Such techniques will also be detailed.

In section B.1, we expose in details the method we used to detect faces, which is used to define the face detection weights we mentioned in section 2.7. We apply the standard face detector ([16]) by Viola et al. on the Mercator projection (section 1.3.3) of the equirectangular image. Implementation details of this process are also provided.

Section B.2 shows the method we propose to semiautomatically detect lines on equirectangular images. This method will try to replace the task of the user of marking lines, which is performed in window 1 of our application (section A.1). We apply the *Hough transform* on perspective projections (section 1.3.1) of the equirectangular image to detect lines. It turns out that the results obtained by doing only that are not satisfactory and preprocessing steps will be necessary. We also show implementation details for this method and a final panoramic image produced when one uses such detection of lines, instead of marking them on the equirectangular image.

B.1 Automatic Face Detection in Equirectangular Images

In this section we explain how we find the weight field w_{ij}^F exposed in section 2.7, that depends on the localization of faces on the equirectangular image. In a more general context, we show a method for face detection in equirectangular images.

Beyond our motivation of using such detection for correcting shape distortion in face regions on panoramic images, there are other motivations for the face detection problem. For more information, we recommend the presentation available in [23].

We start by explaining the main details of the standard face detector by Viola and

Jones ([16]), which is the key ingredient for our method. Then we show how we joined this detector to other steps to produce a method that automatically detects faces in equirectangular images. It is important to mention that this method was already proposed very briefly in [1] and this section intends to give more details about it.

Next, we show some results and finish explaining how we compute the weight field $w^F_{i,j}$ based on the faces detected by the method.

B.1.1 Robust Real-time Face Detection

In this section we explain [16], which is one of the main methods to detect faces in images known in the Computer Vision literature. It is applicable to detect frontal faces. We do not intend to expose technical details about implementation, time of detection and comparisons with previous methods. We focus only on explaining the main ideas of the method. For details, we recommend the user to read [16].

The method is based in three key ingredients, which are the three main contributions of [16]:

• **Integral image:** use an integral graph for fast feature evaluation.

• **Feature selection:** select important features, using a learning method;

• **Focus of attention:** focus on potential sub-windows of the image. These sub-windows are selected by a cascade of classifiers.

We assume that the detection is going to be performed in a gray scale image with equalized histogram.

The features that are going to be used to detect faces are the *rectangular features*, which are illustrated in figure B.1

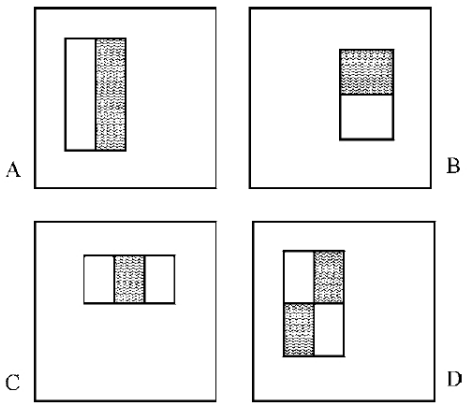

Figure B.1: The sum of pixels that lie within white rectangles are subtracted from the sum of pixels in the gray rectangles.

Observe that the set of rectangular features is over complete: for the base resolution[1]

[1]The detector is constructed assuming such base resolution. The detection is performed by scaling

of the detector that is 24×24 pixels there are 160,000 different rectangular features.

The main advantage of the rectangular features is that they are easy to evaluate using the *integral image* model. The integral image at pixel (x, y) is given by

$$ii(x, y) = \sum_{x' \leqslant x, y' \leqslant y} i(x', y'),$$

where i is the original image. The value of the integral image is illustrated in figure B.2.

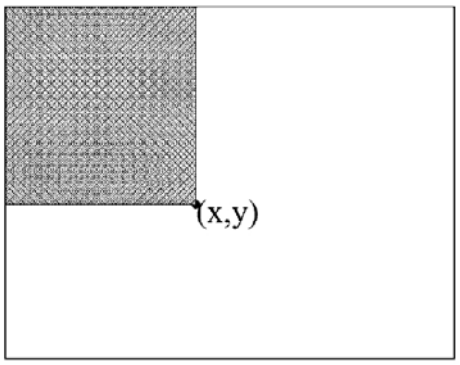

Figure B.2: Value of the integral image at (x, y).

The integral image can be calculated for the entire image in just one pass. In fact, using the cumulative sum in row x,

$$s(x, y) = s(x, y - 1) + i(x, y),$$

we have the relation

$$ii(x, y) = ii(x - 1, y) + s(x, y)$$

and this relation permits that the integral image is evaluated in just one pass. Here we assume $s(x, -1) = 0$ and $ii(-1, y) = 0$.

Now it is easy to evaluate a sum inside a rectangle. For example, in figure B.3, the sum within D is easy to obtain using the values of the integral image.

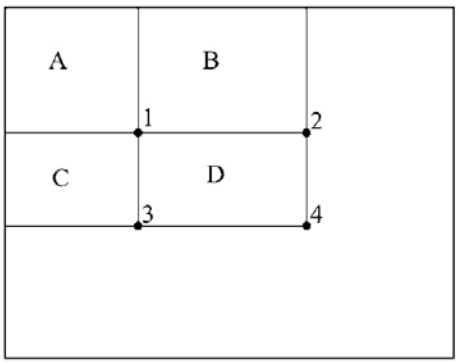

Figure B.3: The sum within D can be computed as $4 + 1 - 2 - 3$.

the obtained detector in different resolutions. More details in [16].

With the rectangular features, we can start defining the classifiers. A *weak classifier* is a function $h(x, f, p, \theta)$ which depends on a feature f, a threshold θ and a polarity p:

$$h(x, f, p, \theta) = \begin{cases} 1 & , \quad \text{if } pf(x) < p\theta \\ 0 & , \quad \text{otherwise,} \end{cases}$$

where x is a 24×24 sub-window of the image.

Now it is necessary to choose which classifiers characterize better face features. This selection is done using a training process based on face and non-face examples (some face examples used for training are shown in figure B.4) as described below. After such classifiers are chosen, a strong classifier is constructed. This process is explained below.

Figure B.4: Example of frontal upright face images used for training.

Adaboost - Inicialization

• Given examples $(x_1, y_1), \ldots, (x_n, y_n)$, where $y_i = 0; 1$ for negative and positive examples.

• Initialize weights $w_{1,i} = \frac{1}{2m}, \frac{1}{2l}$, for $y_i = 0, 1$ respectively where m and l are the number of negatives and positives.

Adaboost - Loop: for $t = 1, \ldots, T$:[2]

• Normalize weights: $w_{t,i} \leftarrow \frac{w_{t,i}}{\sum_{j=1}^{n} w_{t,j}}$;

• Select the weak classifier that minimizes

$$\epsilon_t = \min_{f,p,\theta} \sum_i w_{t,i} |h(x_i, f, p, \theta) - y_i|.$$

Obs. 1: $\epsilon_t \in [0, 1]$.

Obs. 2: There is a way of efficiently minimize ϵ_t, described in [16];

[2] T stands for the number of weak classifiers that will compose the strong classifier. It is a chosen parameter.

• Define

$$h_t(x) = h(x, f_t, p_t, \theta_t),$$

where f_t, p_t, θ_t are the minimizers of ϵ_t;

• Update the weights:

$$w_{t+1,i} = w_{t,i}\beta_t^{1-e_i},$$

where $e_i = 0$ if example x_i is classified correctly, $e_i = 1$ otherwise, and $\beta_t = \dfrac{\epsilon_t}{1-\epsilon_t}$.

Obs.: This update means that if the error ϵ_t is low, the examples that were classified correctly will be less considered for the next weak classifier selection.

Adaboost - Final strong classifier

• After the T weak classifiers are chosen, the final strong classifier is defined as:

$$C(x) = \begin{cases} 1 \quad , & \text{if } \displaystyle\sum_{t=1}^{T} \alpha_t h_t(x) \geqslant \frac{1}{2}\sum_{t=1}^{T} \alpha_t \\ 0 \quad , & \text{otherwise} \end{cases},$$

where $\alpha_t = \log \frac{1}{\beta_t}$.

Obs.: If the error ϵ_t is low, α_t is higher.

To illustrate the learning process, we show in figure B.5 the features associated to the first two weak classifiers selected by the method.

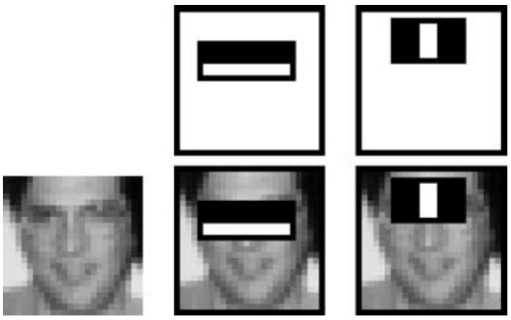

Figure B.5: The first two features: The first one measures the difference in intensity between the region of the eyes and a region across the upper cheeks. The feature capitalizes on the observation that the eye region is often darker than the cheeks. The second feature compares the intensities in the eye regions to the intensity across the bridge of the nose.

It turns out that a 200-feature strong classifier is fast, the results are good but not enough for many real tasks. Adding more features increases too much the computational time. The solution for this problem is to develop a *attentional cascade classifier*, that we explain briefly below:

• Simpler strong classifiers are used in the first stages of the cascade to reject non-face windows, leaving just a few windows to be evaluated by the more complicated strong classifiers in next stages.
• The illustration of this process is shown in figure B.6.

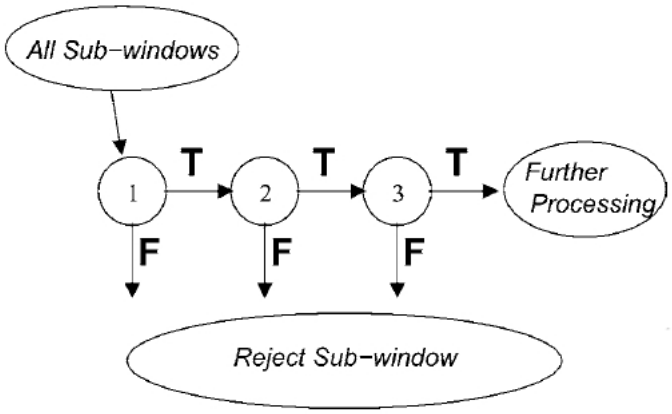

Figure B.6: The windows that are rejected by the simpler classifiers are no longer evaluated, leaving to the more complicated classifier a reduced number of windows to evaluate.

• The training process to obtain a good cascade classifier is based on detection and performance goals. We do not explain this process here, for more details see [16].

The most computationally expensive part of this method is the training process. But once training is completed, the detector is ready to be applied to any image and the detection time is very fast. The discussion about time of training and detection can be found in [16].

Another important point to emphasize is that this the training and detection processes are applicable for detection of other kinds of objects, not only faces.

B.1.2 Method and Implementation

In this section, we show and explain each step of our method for detecting faces in equirectangular images. The method starts by projecting the equirectangular image using the Mercator projection (section 1.3.3) and obtaining its corresponding Mercator image. Next, the face detection process explained in previous section is applied to the Mercator image and the coordinates of the detected faces are mapped back to the equirectangular domain.

We also show implementation details of some steps. We used the OpenCV library ([24]) and C++ language to implement this method.

Step 1: Obtain the Mercator Image

This step is necessary because the faces in the input equirectangular image may be too

distorted due to the longitude/latitude parametrization distortions. Beyond, the Mercator projection preserves the vertical orientation of the faces that are vertical in the equirectangular domain. Also, the Mercator projection is conformal, i.e., it will preserve well the shape of the faces. These two observations make the face detector explained in the previous section applicable for the Mercator image.

Step 2: Process the Mercator image

Obtain its corresponding gray scale image and equalize its histogram. We show below the code that performs this 2 steps:

```
cvCvtColor( mercator_image, gray, CV_BGR2GRAY );
cvResize( gray, img2, CV_INTER_LINEAR );
cvEqualizeHist( img2, img2 );
```

The processed image is saved as *img2*.

Step 3: Detect faces on the Mercator image

This step is performed using OpenCV's function *cvHaarDetectObjects*:

```
CvSeq* cvHaarDetectObjects(
const CvArr* image,
CvHaarClassifierCascade* cascade,
CvMemStorage* storage,
double scale_factor,
int min_neighbors,
int flags,
CvSize min_size
);
```

This function implements a variation of the method explained in section B.1.1. It includes diagonal features to the rectangular ones, but the rest of the process is identical to what we explained.

• *image* stands for the input image, the Mercator image in our case.

• *cascade* stands for a cascade classifier: OpenCV makes available classifiers for front face detection. The command

```
CvHaarClassifierCascade *cascade = (CvHaarClassifierCascade*)cvLoad( "C:/Program
Files/OpenCV/data/haarcascades/haarcascade_frontalface_alt.xml",NULL,NULL,NULL);
```

loads such a classifier, for example.

• *storage* is a memory space where the detected faces will be stored.

• *scale_factor* is the jump between resolutions where the detector will look for faces. For

example, we used $scale\_factor = 1.05$, which means that each scale is 5% larger than the previous scale.

• *min_neighbors* stands for the number of neighbor windows that has to be detected to a window be reported as a face. This parameter uses the observation that usually when a window is detected as a face, some other windows near it will be reported as a face too. Thus the parameter prevents that false face results happen. We used $min\_neighbors = 4$.

• *min_size* is the minimum size of window where the detector looks for faces. We used 1×1 pixel window as minimum.

Step 4: Loop on detected faces

For each detected face:

• Map the coordinates of its center and corners (in the Mercator image) back to the equirectangular domain;

• Draw a rectangle around the face on the equirectangular domain;

• Write in a text file (the file *face_matrix.txt* mentioned in section A.2) the (λ, ϕ) coordinates of the center of the face and $\sigma = \frac{radius}{3}$, where *radius* is the radius of the face on the Mercator domain. Example and details about this file we give in section B.1.4.

We made the source code of the method available in [23].

B.1.3 Results

We show in this section some result images (figures B.7, B.8 and B.9) of the method described in last section.

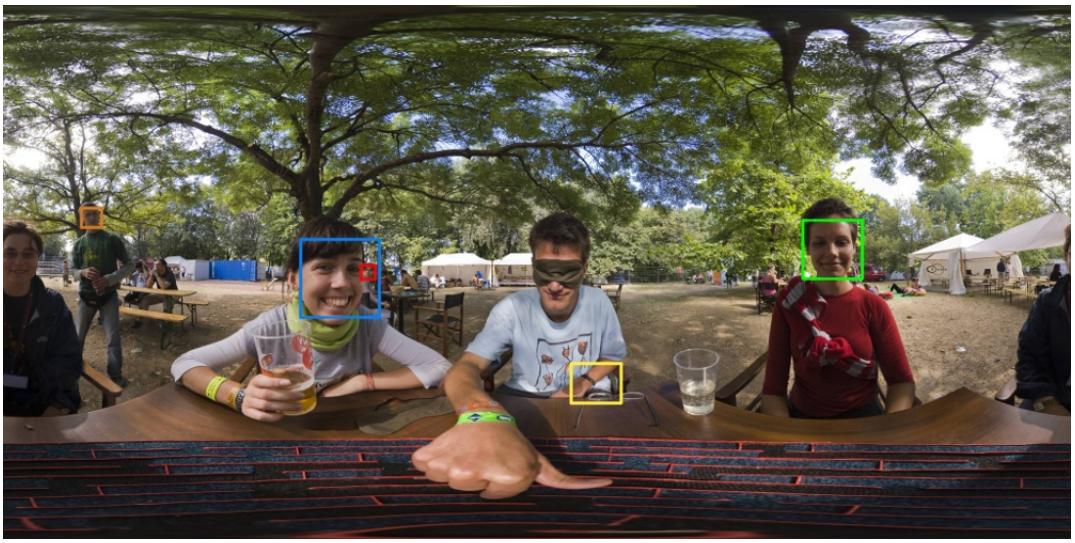

Figure B.7: 4 faces correctly detected, 1 missing and 1 false detection. Source image: "Sziget 2008: Solving a maze", by Flickr user Aldo.

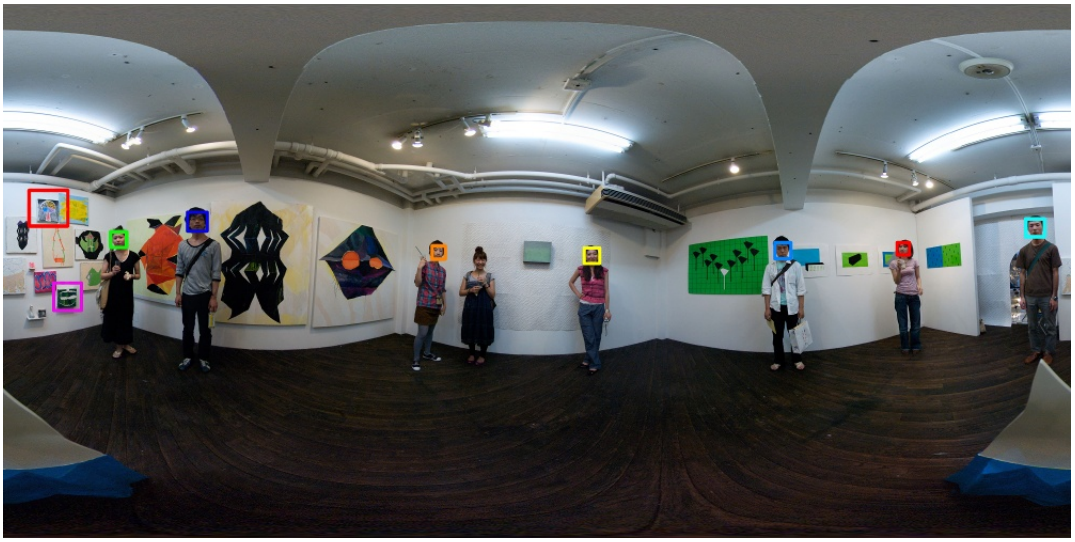

Figure B.8: 7 faces correctly detected, 1 missing and 2 false detections. Source image: "eppoi3", by Flickr user pop⋆.

The detection in figure B.9 was already used in a result shown in chapter 3. We discuss more this example in next section, where we illustrate how to obtain the weights w_{ij}^F (face weights introduced in section 2.7).

Figure B.9: 6 faces correctly detected and 1 false detection.

B.1.4 Weight Field

We show below the output file (*face_matrix.txt*) for the result shown in figure B.9:

```
1.8316 0.1564 0.0237
-0.8419 -0.0408 0.0259
0.8734 0.1502 0.0244
2.3374 0.0816 0.0259
-0.0346 0.1035 0.0326
```

```
-1.7247 -0.1502 0.0467
1.1058 -0.3801 0.0541
```

Each line corresponds to a detected face, say f_k. The first two numbers are the coordinates (λ_k, ϕ_k) of the center of the face in the equirectangular image and the last number, say σ_k, corresponds to one third of the radius of the face in the Mercator projection.

For each $(\lambda_{ij}, \phi_{ij})$ in the discretization of $[\alpha_1, \alpha_2] \times [\beta_1, \beta_2]$ we define

$$w_{ij}^{(k)} = e^{-\frac{\|M(\lambda_{ij},\phi_{ij}) - M(\lambda_k,\phi_k)\|^2}{2\sigma_k^2}},$$

where M is the Mercator projection. To define the face weights w_{ij}^F we just sum the weights over all faces:

$$w_{ij}^F = \sum_{f_k \text{ face}} w_{ij}^{(k)}.$$

B.2 Semiautomatic Line Detection in Equirectangular Images

As we saw in Appendix A, the task for marking lines in equirectangular images may be quite long, depending on the scene. Also, straight lines in the world are curved in the image, and identify which arcs correspond to lines in the world may be difficult in some cases. For these reasons, we propose in this section a method to semiautomatically detect lines in equirectangular images. This detection can substitute or abbreviate the task of marking lines performed by the user in window 1 (section A.2.1).

The detection is semiautomatic because it depends on parameters. This set of parameters may vary from case to case and we did not find a good fixed set. Such parameters are detailed in the end of this section.

We start this section by explaining the *Hough transform*, the *bilateral filter* and a process that we called *eigenvalue processing*. These three topics will not be explained in the equirectangular image context because such operations will be performed in perspective images.

Next, we detail our method that is based on obtaining six different perspective projections from the equirectangular image and searching for lines in each of them.

To finish, we show some results of our method and panoramic images that one would obtain if used the detected lines instead of marking them in window 1. We also make some concluding remarks.

B.2.1 The Hough Transform

In this section we show a standard technique for detecting lines in images, named *Hough transform*. The example image that we will use in this and in next two sections is shown in figure B.10.

Figure B.10: Example image: a perspective projection taken from an equirectangular image.

The Hough transform is applied to a binary image. We apply the *Canny filter* to the previous image and obtain the *edge* image shown in figure B.11.

Figure B.11: Binary image obtained with Canny edge detector.

The function *cvCanny* in OpenCV implements Canny edge detector. Its syntax is the following:

```
void cvCanny(const CvArr* img,CvArr* edges,double lowThresh,
double highThresh,int apertureSize = 3)
```

For theoretical details about the detector and information about the parameters of the above function, we recommend [24] (pages 151 to 153). We do not explain here which parameters we used to obtain the result in figure B.11.

To find straight lines in the image, we analyze each white point (x_0, y_0) in the binary image. Passing through (x_0, y_0) there are infinite lines of the form

$$y_0 = ax_0 + b.$$

Thus, there is an infinity of pairs (a, b) corresponding to lines passing through (x_0, y_0). Each pair (a, b) receives a vote and the most voted pairs correspond to the lines with more points in the image. It turns out that this representation is not convenient for implementation purposes since a and b are in the range $[-\infty, +\infty]$. For this reason, each line passing through (x_0, y_0) is written in polar coordinates

$$\rho = x_0 \cos\theta + y_0 \sin\theta$$

and represented by (ρ, θ). The set of all (ρ, θ) representing lines passing through (x_0, y_0) form a sinusoidal curve in the (ρ, θ) plane (called *Hough plane*) as illustrated in figure B.12. figure B.11.

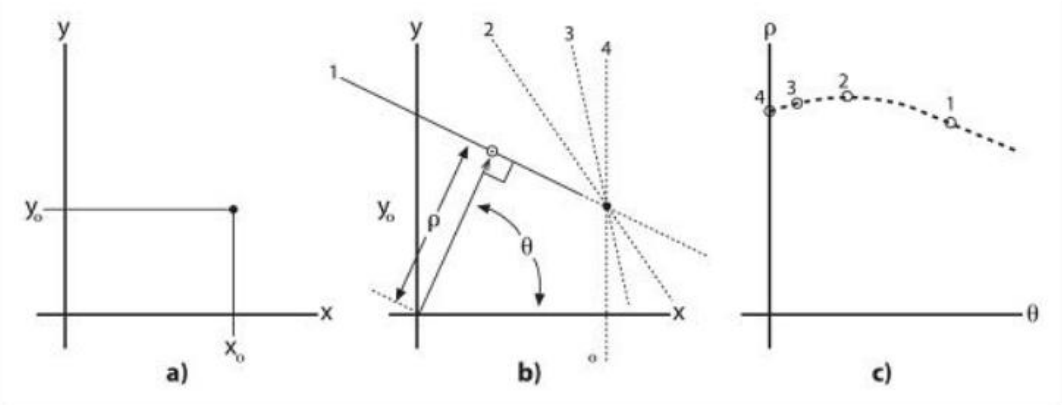

Figure B.12: 4 lines passing through (x_0, y_0) are shown in b). Each one of these lines are represented by a point (ρ, θ) in the Hough plane (c). All possible lines through (x_0, y_0) form a sinusoidal curve in the Hough plane. Figure taken from [24].

The most voted pairs (ρ, θ) represent lines with more points in the edge image and are elected as lines.

OpenCV implements this process through the function *cvHoughLines2*:

```
CvSeq* cvHoughLines2(CvArr* image, void* line storage, int method, double rho,
double theta, int threshold, double param1 = 0, double param2 = 0);
```

For details about the parameters, we refer to [24] (pages 156 to 158). We used for *method* the value *CV_HOUGH_PROBABILISTIC*, which returns lines with endpoints, a very

convenient feature for our application. We do not discuss what values we used for the other parameters here.

In figure B.13, we show the detected lines for our example.

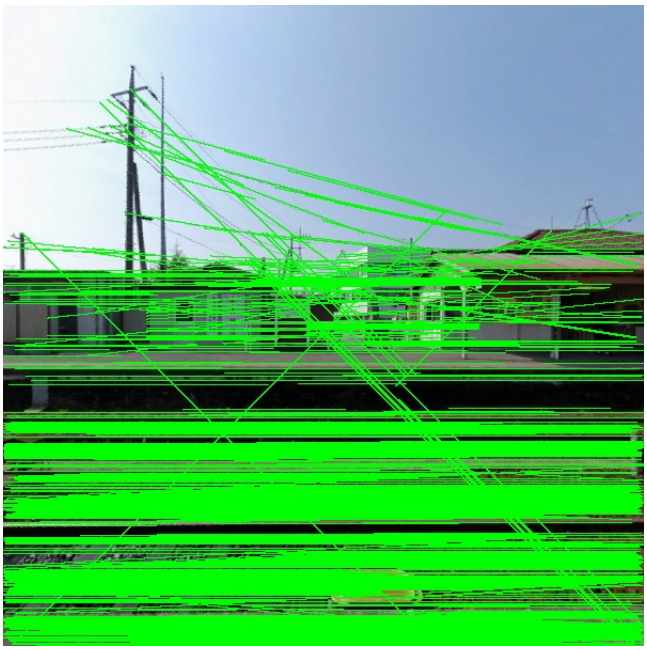

Figure B.13: The detected lines are shown in green.

As one can see, many nonexisting lines were detected. This happened because, in highly textured regions, as the ground between the rails, the edge detector detected many points that voted too much for nonexisting lines in such regions. A naive solution would be to change the parameters of the edge detector to detect less lines, but this would cause in missing many lines. In next sections, we present methods that try to alleviate such problem.

B.2.2 Bilateral Filter

Our first attempt to remove undesirable texture from an image was to use bilateral filtering. Simple blurring would handle this task but would also blur lines and the edge detector would not detect them.

The bilateral filter only blurs pixels on the image that have similar neighbors because it considers the difference of colors between pixels: this is appropriate to remove textures that do not have great disparity of colors and preserves the most important edges.

More formally, for some pixel p, the filtered result is:

$$[BF(I)]_p = \frac{1}{k_p} \sum_{q \in \Omega} I_q G_{\sigma_s}(\| p - q \|) G_{\sigma_r}(\| I_p - I_q \|),$$

where G_{σ_s} is a gaussian filter centered on p with deviation σ_s and G_{σ_r} is a gaussian filter centered on I_p with deviation σ_r, k_p is a normalizing factor, the sum of the $G_{\sigma_s} \cdot G_{\sigma_r}$ filter weights and Ω is the spatial support of G_{σ_s}.

OpenCV has the following function:

```
cvSmooth(const CvArr* src, CvArr* dst, int smoothtype=CV_GAUSSIAN,
int param1=3, int param2=0, double param3=0, double param4=0).
```

The parameters mean the following:

- *src, dst*: Source and destiny images;
- *smoothtype:* Set CV_BILATERAL;
- *param1=param2:* Size of spatial support Ω (it has to be square);
- *param3:* Color sigma (σ_r);
- *param4:* Space sigma (σ_s);

For our example the result of bilateral filtering is shown in figure B.14:

Figure B.14: Bilateral filtering using $\sigma_s = 15$ and $\sigma_r = 31$.

A good way of removing more texture of the image is to reapply the bilateral filter. We show in figure B.15 the result of applying bilateral filter six times on the example image, with the same parameters ($\sigma_s = 15$ and $\sigma_r = 31$).

For the method proposed in section B.2.4, the number of applications of the filter is always six. The parameters σ_s and σ_r are passed on the command line.

B.2.3 Eigenvalue Processing

After bilateral filtering, Canny edge detector is applied to the image. In some cases, undesirable textures still remain (see figure B.16).

We applied a method suggested in [25]. It consists in spliting the binary images in windows of the same size and perform a local analysis of the position of the points in each window.

Figure B.15: Result applying six times the bilateral filter. Notice how almost all the texture is gone and the important lines still remain.

Figure B.16: Result of the edge detector applied after bilateral filtering. Some textures still remain and blurring more the image would blur too much the important lines.

If the points lie in the same direction, they possibly must belong to a line. Otherwise, if the points are too spread in the cell, they must be discarded because they do not belong to a line.

For each window, a *covariance matrix* is constructed:

$$A = \begin{pmatrix} a & b \\ b & c \end{pmatrix},$$

where

$$a = \frac{\sum_{i=1}^{n}(u_i - \overline{u})^2}{n},$$

$$b = \frac{\sum_{i=1}^{n}(u_i - \overline{u})(v_i - \overline{v})}{n},$$

$$c = \frac{\sum_{i=1}^{n}(v_i - \overline{v})^2}{n},$$

$$(\overline{u}, \overline{v}) = \frac{\sum_{i=1}^{n}(u_i, v_i)}{n},$$

where n is the number of white points in the window and u_i and v_i are the cartesian coordinates of each white point.

The eigenvalues of A are:

$$\lambda_1 = \frac{a + c + \sqrt{(a-c)^2 + 4b^2}}{2}, \text{ and } \lambda_2 = \frac{a + c - \sqrt{(a-c)^2 + 4b^2}}{2}$$

It is clear that $\lambda_1 \geqslant \lambda_2$ and both are positive. If the ratio between λ_1 and λ_2 is too large, the white points lie close to the direction of v_{λ_1}, the eigenvector associated to λ_1. If λ_1 and λ_2 are too close then there is no predominant direction and the points are too spread in the window.

These ideas give us a way of discarding points:

- Given a binary image, a window size and a threshold value τ;
- For each window, if $\frac{\lambda_1}{\lambda_2} < \tau$, discard all the white points of this window.

For the example in figure B.16, we obtain the result in figure B.17.

To implement this step we programmed a function named *eig_preprocess*:

```
IplImage* eig_preprocess(IplImage* grayscale, float tau, int window_size)
```

B.2.4 The Method

In this section we explain how we integrate the techniques exposed up to here to detect straight lines in equirectangular images. We explain the steps of the method and illustrate them with an example. We used OpenCV library and C++ language to implement this method.

- **Input:** An equirectangular image that represents a scene (figure B.18).

- **Step 1:** Obtain six perspective projections from the equirectangular images centered on six different points (section 1.4.1). The choice for perspective projections is quite obvious:

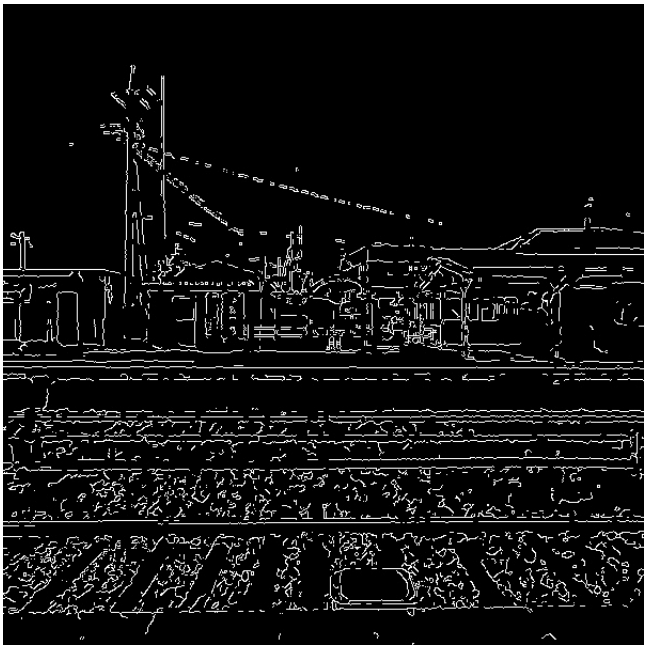

Figure B.17: Result obtained with *window size* = 5 and $\tau = 1.5$. The eigenvalue processing helps to eliminate some textures.

Figure B.18: Equirectangular input image: "Kasuza-Ushiku Station, Kominato Railway, Chiba, Japan", by Flickr user Soosuke.

since we want to detect straight lines in the real world, we have to look for straight lines on an image where the lines are preserved. As we already know, the perspective projection satisfies this requirement. The perspective images for our example are shown in figures B.19, B.20 and B.21.

• **Step 2:** Filter each perspective image with the bilateral filter applied six times. This step depends on two parameters of the bilateral filter and produces results as in figure B.22 (showing just two of the six results).


Figure B.19: Perspective projections centered on $(\lambda, \phi) = (0, 0)$ and $(\lambda, \phi) = (\frac{\pi}{2}, 0)$.


Figure B.20: Perspective projections centered on $(\lambda, \phi) = (\pi, 0)$ and $(\lambda, \phi) = (-\frac{\pi}{2}, 0)$.


Figure B.21: Perspective projections centered on $(\lambda, \phi) = (0, -\frac{\pi}{2})$ and $(\lambda, \phi) = (0, \frac{\pi}{2})$.

• **Step 3:** Obtain the edges of the filtered images using Canny edge detector. This step depends on a parameter to set the thresholds for the filter. The greater this parameter, the smaller the number of detected edges. The results for this step are shown in figure B.23.

Figure B.22: Results after applying bilateral filtering.

Figure B.23: Edge images obtained with Canny filter.

• **Step 4:** Process these edge images with eigenvalue processing. This step depends on two parameters to discard points. The results for this step are shown in figure B.24.

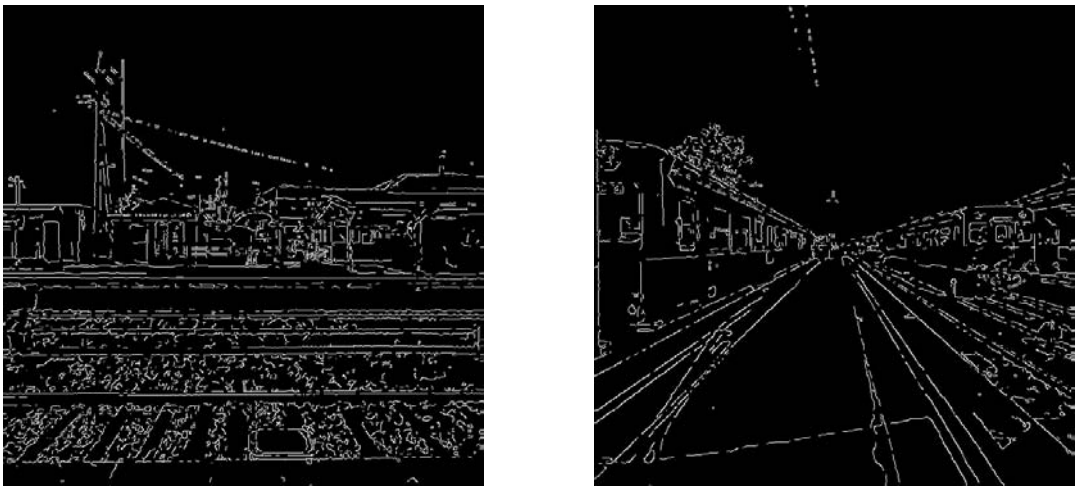

Figure B.24: Results after applying eigenvalue processing.

• **Step 5:** Detect lines from the binary images obtained in step 4 using OpenCV's *Hough*

Probabilistic Transform. Figure B.25 shows the results for this step.

Figure B.25: Detected lines are indicated in green.

• **Step 6:** For each line in each perspective image, obtain its endpoints, map them to the original equirectangular image and plot the geodesic curve connecting these endpoints on the equirectangular domain. The **output** is shown in figure B.26.

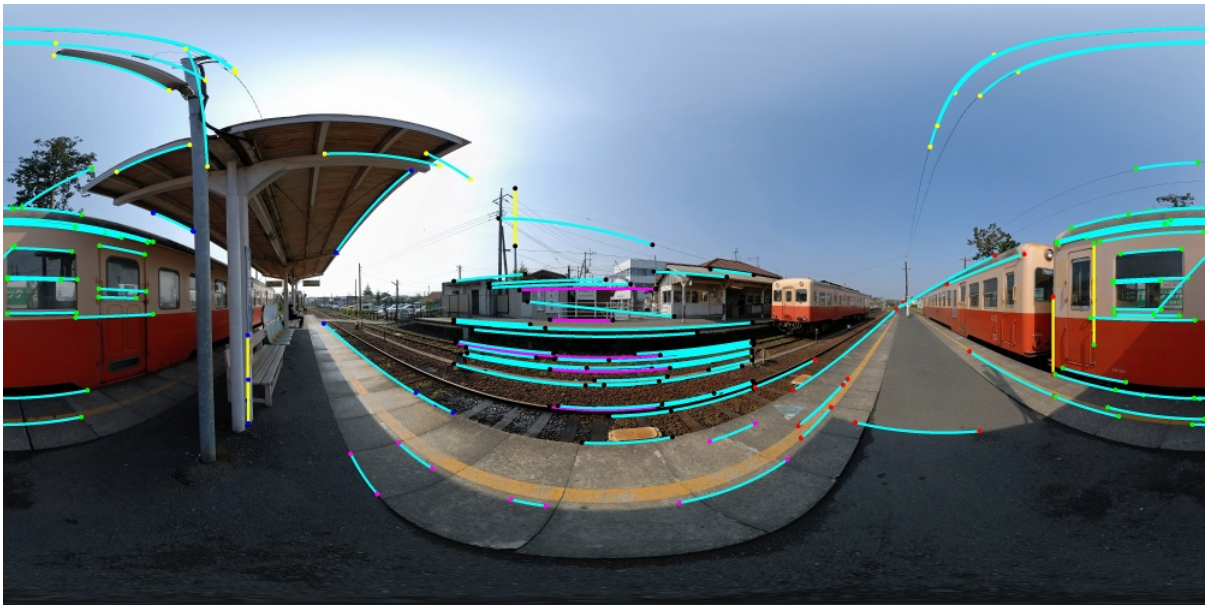

Figure B.26: Final result. 110 line segments detected.

Besides the final image, the method also produces two files *L_endpoints* and *L2_endpoints* (as in section A.2.1) with coordinates of the endpoints, orientation and index for each line.

As we mentioned before, our method depends on parameters, which are passed in command line. Below we explain what each parameter means:

• *argv[1]*: Input equirectangular image;

• *argv[2]*: Output image;

• *argv[3]*: Parameter used by the filter Canny (step 3 described in the 1st section of this report);

• *argv[4]*: σ_s (space sigma for bilateral filter). The greater this parameter, the smaller the number of detected lines because the image is more blurred;

• *argv[5]*: σ_r (range sigma for bilateral filter). The greater this parameter is the stronger the edge has to be to not be blurred, i.e., the greater this parameters the smaller the number of detected lines too;

• *argv[6]*: Window size for eigenvalue processing. It decides the locality of the eigenvalue analysis;

• *argv[7]*,*argv[8]*,*argv[9]*,*argv[10]*,*argv[11]*,*argv[12]*: τ value for eigenvalue processing for the six different perspectives. Since all the steps are performed separated in each perspective, the user may want to discard more points (and thus detect less lines in the final result) in a different way for the different perspective images.

B.2.5 Results

Figures B.27, B.28 and B.29 show some more results obtained with our method.

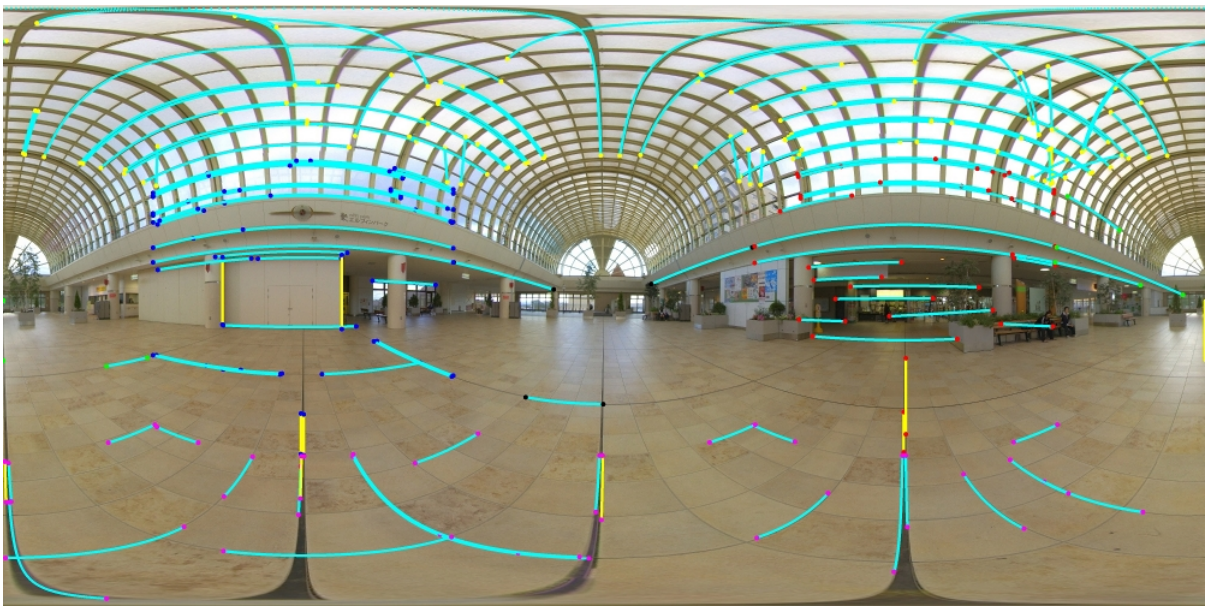

Figure B.27: 161 line segments detected. Input image: "Kitahiroshima Station", by Flickr user Vitorid.

Figure B.28: 93 line segments detected. Input image: "Microsoft Vodafone Viaduct", by Flickr user Craigsydnz.

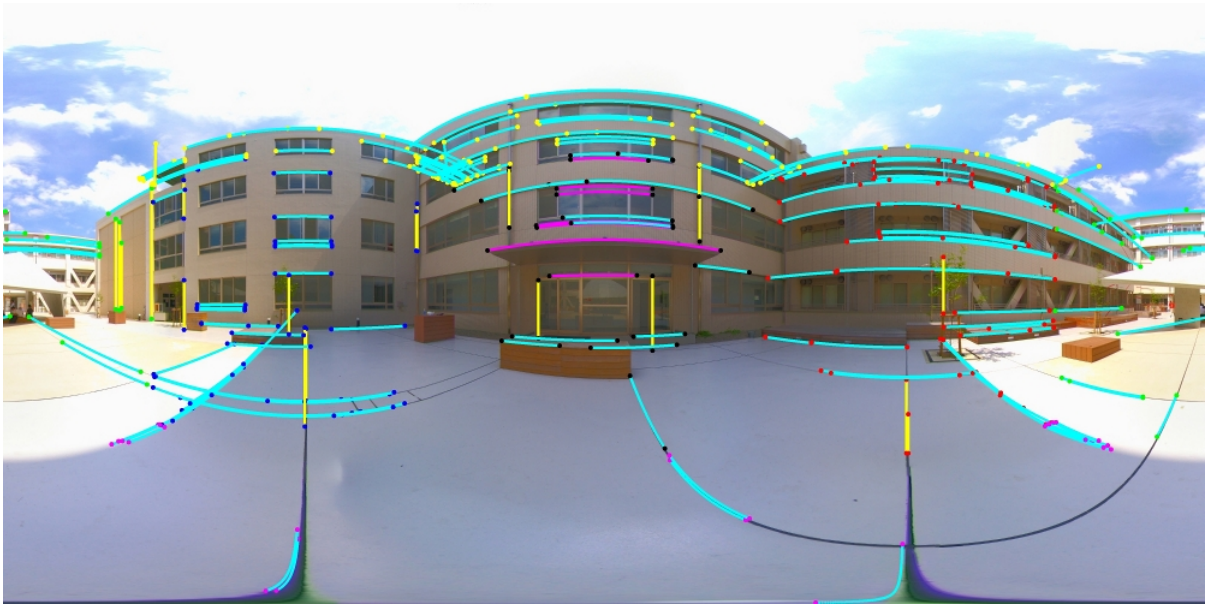

Figure B.29: 226 line segments detected. Input image: "Nagoya University", by Flickr user Vitorid.

In figure B.30 we show a final panoramic image produced using the lines returned by our method, shown in figure B.26.

B.2.6 Concluding remarks

As can be seen in figures B.26, B.27, B.28 and B.29 many important lines were detected by our method, but some other lines were missing. Another problem is that there are regions (as the rails in figure B.26) where too many lines were detected, which leads to too many constrains for our optimization. Other point to be mentioned is that, when the

Figure B.30: Panoramic image produced using lines shown in figure B.26. FOV: 140 degree longitude/160 degree latitude. Vertices: 31,000.

user marks lines, she has the possibility of marking lines that are not clearly represented in the image as a horizon that she wants to be horizontal in final image.

All the reasons mentioned above show us that our detection should be integrated to window 1, as a preprocessing step. The user could remove, include or extend the detected lines, which is easier than looking for all possible lines and marking them. Also, the user could control the parameters of our line detector in the interface, which is more intuitive.

We leave the integration of our line detector to the interface as future work.

Conclusion

Review

In this section, we review the main aspects of our work and reinforce which of them are original contributions.

• **Modeling of concepts related to the problem:** We modeled some concepts that are part of the physical world as mathematical entities. For example, field of view was modeled as a part of a sphere, panoramic images as functions and so on.

• **Bibliographic review:** We provided a bibliographic review of the panoramic image problem, giving details of the main references on this topic and discussing pros and cons of each approach. We also obtained conclusions on perceptual properties that are desired in panoramic images, such as conformality and preservation of straight lines. This review can be seen as a small contribution of our work.

• **Deep and conclusive analysis of [1]:** We discussed this reference in a formal and detailed way, making our work a good complement for it. For example, the perturbed optimization, which we called *linear system method*, was mentioned very briefly and no details were provided in [1]. In our work, we wrote explicitly the perturbed energy $\tilde{E}$ and proved some statements in order to obtain its minimizer. Other example is how to turn the quadratic energies into matrix form and what matrices are obtained in this process. The discussion of the results was richer in our work and we could conclude that the method is applicable for a good variety of scenes. All this analysis is one of the main contributions of our work.

• **Development of the application software:** We developed a software that implements all the theory discussed about [1]. New features such as specification of FOV, number of iterations and vertices were added to the interface in [1] which turns our software a small contribution of our work.

• **Methods to detect features in equirectangular images:** We applied Compu-

ter Vision techniques to develop methods for detecting faces and lines in equirectangular images, which are important for the main reference we discussed in the thesis. The line detection method is an original contribution of our work.

• **Panoramic videos:** We separated the problem in 3 cases, stated desirable properties in panoramic videos, defined the temporal viewing sphere and studied some of its properties, mathematically modeled the panoramic video problem, turned the desirable properties into mathematical equations, obtained energies that measure how temporally incoherent a panoramic video is and suggested an optimization solution for one of the cases. This is the main original contribution of this thesis, since almost no material on this topic is known on the literature.

Discussion

At the end of this thesis, we can make some qualitative concluding remarks that reflect the main ideas one can get from our work.

The first one is that the panoramic image problem is now very mature. The need for obtaining images of wide fields of view finds its roots centuries ago in paintings and the limitation of perspective projection was already in the Renaissance. But only with the development of technology and methods as, for example, stitching equipment and methods, it was possible to bring this theme to a different level. In recent years, many publications on the theme were published and now it is clear what properties we expect in panoramic image.

Among all these references, we decided to study and implement Carroll et al. ([1]). We think we proved the applicability of the method by showing a variety of situations where it produces good results. The explanation for the quality of the method is that it models precisely the undesirable distortions through the mathematical formalization of them. Equations and energy terms were used to model the distortions.

At this point, it is valuable to observe how a concrete theme such as producing panoramic images and videos can amalgamate very different areas of pure and applied mathematics. In this work, we used theories and techniques related to the following areas: Differential Geometry, Linear Algebra (both theoretical and numerical), Optimization, Numerical Analysis, Analytic Geometry, Multivariable Analysis, Statistics, Computer Vision, Image and Video Processing.

Interesting extensions arose from our study of panoramic images. In this work, we suggested methods to detect lines and faces in equirectangular images and opened a novel discussion about panoramic videos. This work left open many possibilities for future work and we point them in next section.

Future Work

We think the most important future work for the panoramic image problem are:

• **Migrate all the Matlab code to C/C++:** We implemented the optimization and the interface in different languages. It would be interesting for future applications to integrate both parts to the same language.

• **Integration of line detection to the interface:** This integration would allow the user to specify the parameters for line detection in a window where she also could include or remove lines.

• **Apply the method to gigapixel images:** After finding a discretized projection using the method described in chapters 2 and 3, the final panoramic image is produced using bilinear interpolation and this process can be done for any resolution of the input equirectangular image, even gigapixel ones. High quality results would be produced using these input images.

For the panoramic video problem, the next steps we intend to pursue are the following:

• **Finish case 1:** We intend to implement the other solutions discussed for this case and compare them to the one implemented in this thesis.

• **Case 2:** Implement the optimization solution and compare it to the solution presented in this thesis.

• **Integrate cases 1 and 2:** Use the solutions of these cases to solve the panoramic video problem with stationary viewpoint.

• **Case 3:** Generalize for this case what was developed for the first 2 cases.

• **Investigate numerical methods for the problem:** The solution we proposed in this thesis took too long to be computed. We intend to investigate numerical and computational methods for the problem in order to produce results faster.

The development of the panoramic video theme may cause impact for different areas of art and entertainment, since it leads to a different way of filming and visualizing scenes. We mention below some areas of application:

• **Cinema:** If a scene is filmed with a spherical camera that produces an equirectangular video, there is no need to choose in which direction to point the camera. The scene will be much better represented by the equirectangular video and specification of FOVs could be done as a post processing step. An interesting future work is to develop an interface where the input is an equirectangular video and the user can specify different FOVs for different times. Also, the possibility of filming and visualizing wide FOVs can add interesting new possibilities on narratives. Special display devices that cover a wider FOV can be developed to explore better this new way of filming and displaying.

• **Sport broadcasting:** There is a huge difference between watching a soccer game in the stadium or at home in the TV. One of the reasons for this fact is that in the stadium we

perceive much better the details of all the field, while at home we only see a limited FOV (usually a window around the position of the ball). Since the structure of the soccer game scene is very simple (some lines in the field and a set of known moving objects), one of the first applications of panoramic videos could be for sports filming. These considerations are extendable for other sports such as basketball, baseball, volleyball and so on.

• **Vigilance:** Spherical cameras can replace common cameras for vigilance since they "see" much more information. Analysis of spherical videos (as, for example, people detection) become necessary and informative ways of displaying the video (i.e., the choice of the appropriate projection) may be analyzed.

We intend to work with these (and possibly other) practical applications as soon as we develop more the theoretical ideas on the theme.

Bibliography

[1] R. Carroll, M. Agrawal, and A. Agarwala, "Optimizing content-preserving projections for wide-angle images," *ACM Trans. Graph.*, vol. 28, no. 3, pp. 1–9, 2009.

[2] R. Szeliski and H.-Y. Shum, "Creating full view panoramic image mosaics and environment maps," in *SIGGRAPH '97: Proceedings of the 24th annual conference on Computer graphics and interactive techniques*, (New York, NY, USA), pp. 251–258, ACM Press/Addison-Wesley Publishing Co., 1997.

[3] M. Brown and D. G. Lowe, "Recognising panoramas," in *ICCV '03: Proceedings of the Ninth IEEE International Conference on Computer Vision*, (Washington, DC, USA), p. 1218, IEEE Computer Society, 2003.

[4] J. Kopf, M. Uyttendaele, O. Deussen, and M. F. Cohen, "Capturing and viewing gigapixel images," *ACM Trans. Graph.*, vol. 26, no. 3, p. 93, 2007.

[5] D. Zorin and A. H. Barr, "Correction of geometric perceptual distortions in pictures," in *SIGGRAPH '95: Proceedings of the 22nd annual conference on Computer graphics and interactive techniques*, (New York, NY, USA), pp. 257–264, ACM, 1995.

[6] M. Agrawala, D. Zorin, and T. Munzner, "Artistic multiprojection rendering," in *Proceedings of the Eurographics Workshop on Rendering Techniques 2000*, (London, UK), pp. 125–136, Springer-Verlag, 2000.

[7] L. Zelnik-Manor, G. Peters, and P. Perona, "Squaring the circles in panoramas," in *ICCV '05: Proceedings of the Tenth IEEE International Conference on Computer Vision*, (Washington, DC, USA), pp. 1292–1299, IEEE Computer Society, 2005.

[8] J. Kopf, D. Lischinski, O. Deussen, D. Cohen-Or, and M. Cohen, "Locally adapted projections to reduce panorama distortions," *Computer Graphics Forum (Proceedings of EGSR 2009)*, vol. 28, no. 4, p. to appear, 2009.

[9] "Point grey ccd and cmos digital cameras for industrial, machine, and computer vision." URL: http://www.ptgrey.com.

[10] "Flickr: Equirectangular." URL: http://www.flickr.com/groups/equirectangular/.

[11] J. P. Snyder, *Map projections–a working manual*. Supt. of Docs., 1987.

[12] L. K. Sacht, "Multiperspective images from real world scenes." URL: http://w3.impa.br/~leo-ks/s3d.

[13] L. K. Sacht, "Multi-view multi-plane approach to project the viewing sphere." URL: http://w3.impa.br/~leo-ks/image_processing.

[14] A. Agarwala, M. Agrawala, M. Cohen, D. Salesin, and R. Szeliski, "Photographing long scenes with multi-viewpoint panoramas," *ACM Trans. Graph.*, vol. 25, no. 3, pp. 853–861, 2006.

[15] M. P. Do Carmo, *Differential Geometry of Curves and Surfaces*. New Jersey: Prentice-Hall, Inc., 1976.

[16] P. Viola and M. J. Jones, "Robust real-time face detection," *Int. J. Comput. Vision*, vol. 57, no. 2, pp. 137–154, 2004.

[17] U. Neumann, T. Pintaric, and A. Rizzo, "Immersive panoramic video," in *MULTIMEDIA '00: Proceedings of the eighth ACM international conference on Multimedia*, (New York, NY, USA), pp. 493–494, ACM, 2000.

[18] D. Kimber, J. Foote, and S. Lertsithichai, "Flyabout: spatially indexed panoramic video," in *MULTIMEDIA '01: Proceedings of the ninth ACM international conference on Multimedia*, (New York, NY, USA), pp. 339–347, ACM, 2001.

[19] M. Uyttendaele, A. Criminisi, S. B. Kang, S. Winder, R. Szeliski, and R. Hartley, "Image-based interactive exploration of real-world environments," *IEEE Comput. Graph. Appl.*, vol. 24, no. 3, pp. 52–63, 2004.

[20] A. M. d. Matos, "Visualizacao de panoramas virtuais," Master's thesis, PUC-Rio, 1998.

[21] A. Agarwala, K. C. Zheng, C. Pal, M. Agrawala, M. Cohen, B. Curless, D. Salesin, and R. Szeliski, "Panoramic video textures," in *SIGGRAPH '05: ACM SIGGRAPH 2005 Papers*, (New York, NY, USA), pp. 821–827, ACM, 2005.

[22] L. K. Sacht, "Content-based projections for panoramic images and videos." URL: http://w3.impa.br/~leo-ks/msc_thesis.

[23] L. K. Sacht, "Face detection." URL: http://w3.impa.br/ ~ leo-ks/cv2009/face_detection.

[24] D. G. R. Bradski and A. Kaehler, *Learning opencv, 1st edition*. O'Reilly Media, Inc., 2008.

[25] F. Szenberg, *Acompanhamento de Cenas com Calibracao Automatica de Cameras*. PhD thesis, PUC-Rio, 2001.